DEVELOPMENT OF AN OMNI-DIRECTIONAL WEATHER-MONITORING ANEMOMETER

A Dissertation

by

VIJAY RAMAKRISHNAN

Submitted to the Office of Graduate Studies of
Texas A&M University
in partial fulfillment of the requirements for the degree of

DOCTOR OF PHILOSOPHY

December 2006

Major Subject: Aerospace Engineering

DEVELOPMENT OF AN OMNI-DIRECTIONAL WEATHER-MONITORING ANEMOMETER

A Dissertation

by

VIJAY RAMAKRISHNAN

Submitted to the Office of Graduate Studies of
Texas A&M University
in partial fulfillment of the requirements for the degree of

DOCTOR OF PHILOSOPHY

Approved by:

Chair of Committee,	Othon K. Rediniotis
Committee Members,	Paul G. A. Cizmas
	Rodney D. W. Bowersox
	Luis San Andres
Head of Department,	Helen L. Reed

December 2006

Major Subject: Aerospace Engineering

ABSTRACT

Development of an Omni-Directional Weather-Monitoring

Anemometer. (December 2006)

Vijay Ramakrishnan, B.Tech., Indian Institute of Technology-Madras, India;

M.S., Texas A&M University

Chair of Advisory Committee: Dr. Othon K. Rediniotis

This work presents the design, fabrication, calibration and testing of a pressure-based three-component anemometer capable of measuring accurate wind speeds in extreme weather conditions. The groundwork, at the outset, covers the development of a 12-hole omni-directional flow-velocity measurement probe capable of measuring flows up to 155° from the probe axis. The new 12-hole design is optimal in the sense that the calculation of the four unknown flow quantities, i.e., two flow angles, flow speed and static pressure, is achieved with the minimum necessary number of holes/ports on the probe tip. The fact that this design has 33% lesser number of holes compared to an earlier design, has significant implications in the instrument's spatial resolution, frequency response as well as cost of interfacing and usage. A prototype 12-hole probe with a spherical tip diameter of 3/8 inches was fabricated and tested. Good flow prediction accuracy was obtained.

Further groundwork on multi-hole probe technology was carried out, developing new methods for correcting and refining the calibration and reduction procedures. When calibrating multi-hole velocity probes in a wind-tunnel, offset (or bias) errors often exist in the recorded flow angles due to errors in aligning the traverse system exactly with the flow direction and due to the angularity of the tunnel flow itself. These offset angles are hard to quantify from direct measurements with any degree of accuracy. Although usually small (less than 0.5° in most good calibrations), these errors still need to be

corrected to increase the flow measurement accuracy of the probe. In this work, a method is developed that computes offset errors in all types of multi-hole probes – from the traditional 5- and 7-hole probes to the omni-directional 18-hole probe and the next-generation 12-hole probe – using simply the pressure data obtained during their calibration. The algorithm doubled the measurement accuracy for most probes. Other issues related to post-processing of the pressure data from flow studies, when the multi-hole probe encountered unsteady and reversed flow conditions, were also examined.

The design of the anemometer (herein called a Weatherprobe) builds on that of the 12-hole probe and is capable of measuring wind velocities up to ±45° to the horizontal plane and 360° around the horizontal plane. Due to the non-conventional arrangement of its pressure ports, newly developed calibration and data-reduction algorithms were used. The probe was calibrated and its measurement accuracy assessed in a calibration facility. All associated instrumentation was assembled from the ground up and ruggedized for harsh-weather applications. Field tests performed over many days next to a 3-D sonic anemometer showed good agreement in measured flow properties, thus validating the entire Weatherprobe system. This probe has widespread applications in weather monitoring, wind energy potential estimations and structural wind load evaluations.

ACKNOWLEDGMENTS

I am extremely grateful to my advisor Dr. Othon Rediniotis for his insights, expert advice and patient supervision throughout my research. Under his guidance, my 5+ years of graduate studies has been a rewarding experience.

I acknowledge the guidance given by my advisory committee. Their pointers and insights helped in bringing focus and direction to my research.

I also thank Rick Allen and Josh Weimar for their expert help in the design and fabrication of many parts for the Weatherprobe.

I owe a special thanks to my good friend and colleague Manoranjan Majji, for his immense help during field tests.

My deepest gratitude to Dr. Gunnar Schade and his doctoral student Changhyoun Park of the Department of Atmospheric Sciences, Texas A&M University for accommodating my Weatherprobe system at their field site and for sharing their wind data for comparison studies.

Finally, I thank the Aeroprobe Corporation, especially Dr. Matthew Zeiger (CEO and senior scientist), for the internship opportunity and for the financial support to conduct my research and studies. I also thank Jason Gibbs (Aeroprobe Corp.) for his help during probe calibrations.

TABLE OF CONTENTS

Page

Page

LIST OF TABLES

LIST OF FIGURES

FIGURE Page

FIGURE Page

FIGURE Page

FIGURE Page

FIGURE Page

NOMENCLATURE

English Symbols

A = oscillation amplitude, surface area

A_θ, B_θ = polynomial coefficients for C_θ expression

A_ϕ, B_ϕ = polynomial coefficients for C_ϕ expression

C_p = non-dimensional pressure coefficient

C_s = static pressure coefficient

C_t = total pressure coefficient

C_β = yaw-angle coefficient

C_θ = cone-angle coefficient

C_ϕ = roll-angle coefficient

C_δ = offset coefficient

C_x = cut-off coefficient

D = diameter

dT = temperature difference

f = oscillation frequency

h = convective heat transfer coefficient

K = non-dimensionalized acceleration

k = conductive heat transfer coefficient

Nu = Nusselt number

P = pressure

Pr = Prandtl number

P_s = static pressure

P_t = total pressure

q = freestream dynamic pressure

q_{est} = estimated dynamic pressure

R = radius of sphere

R, S, T = polynomial coefficients for q_{est}

Re = Reynolds number

T_s = static temperature of the flow

U_{mag} = velocity magnitude at measurement point

V = Coulombic potential, volts

Greek Symbols

δ = horizontal offset angle

ε = error

Θ = cone angle in global coordinate system

Θ^* = central angle

θ = cone angle in local coordinate system

μ = viscosity of air

ξ = vertical offset angle

ρ = density of air

σ = standard deviation

Φ = roll angle in global coordinate system

ϕ = roll angle in local coordinate system

Subscripts

ave = averaged value

cal = from calibration database

est = estimated value

pred = predicted value

test = of a test point

1 INTRODUCTION

1.1 PRESSURE PROBE THEORY

Multi-hole pressure probe theory has been widely studied and is well-documented. Popular probes such as 5- and 7-hole probes[1-5] have established themselves as reliable and accurate steady-state flow-measuring devices. They have been used to resolve the three-dimensional flow velocity vector and static and total pressures at the point of measurement in many applications. Some early work includes Bryer and Pankhurst,[6] where a comprehensive overview of probe types, design, and construction is given. Fig 1.1 depicts typical 5- and 7-hole probe tips.

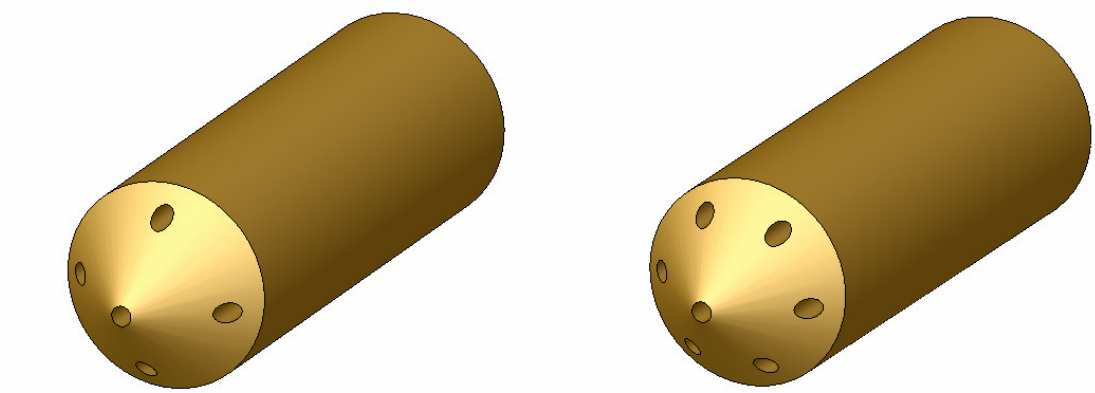

Fig. 1.1 Conical tip 5- and 7-hole probes.

Although multi-hole probes are very popular in subsonic flows, they have also been successfully calibrated and used in transonic[7-9] and supersonic[10-13] flows. Milanovic and Kalkhoran[14] used a numerical method to calibrate a probe instead of tedious experimental techniques and obtained moderate success with prediction accuracy.

This dissertation follows the style of AIAA Journal.

However, for the sake of higher prediction accuracies, most current-generation probes use non-nulling methods based on extensive calibration of the probe that allows for imperfections in the probe tip geometry. The probe is calibrated in a flow field with known properties where every possible flow incidence angle is simulated by rotating and/or pitching the probe through the entire angular range of the probe. The port pressures, corresponding to each angular orientation, are recorded and stored in a calibration database. Based on the calibration data or the type of probe, the angular domain of the probe is divided into sectors. The calibration data is then processed to obtain non-dimensional velocity-invariant coefficients that relate the port pressures (non-dimensionalized with an estimate of the freestream dynamic pressure) to the flow incidence angles. These relations are typically explicit polynomial expressions[15] obtained by surface/curve-fitting the coefficients to the angles. An alternative method to interpolation schemes was studied by Rediniotis and Vijayagopal,[16] where they used artificial neural networks applied to 7-hole probes and achieved good prediction accuracies.

For maximum accuracy at all flow speeds, probe calibrations are usually performed over the entire subsonic regime from Mach 0.1 all the way up to Mach 0.8 (typically in steps of 0.1). Once the calibration is done, the probe is ready for use in an unknown flow field. At any unknown velocity magnitude and flow angles, the non-dimensional pressure coefficients are calculated first from the port pressures. The unknown quantities (flow angles and velocity magnitude) are then calculated from the mathematical relations (established when processing the calibration data) between them and the non-dimensional coefficients. The data-reduction algorithms that convert the pressure data into flow data have also undergone much revisions and improvements over the years resulting in a dramatic increase in the measurement accuracy expected from multi-hole probes – often better than half a degree in the flow angles and half a percent in the velocity magnitude.

Ramakrishnan and Rediniotis[17] presented a systematic way of defining well-behaved pressure coefficients for any generic port arrangement (5-, 7-, 12-, 18-hole or any other) for spherical or hemispherical tipped probes. One of the challenges when working with a generic port arrangement was that the conventional definitions of the non-dimensional pressure coefficients either can no longer be applied, or if they can be applied, they may be far from optimal. Some of the important properties of a properly defined coefficient include independence from the other three variables (for example, the yaw angle coefficient should be independent of the pitch angle, the dynamic and static pressures) and smooth, and preferably linear, behavior. The definitions developed achieve exactly the purpose stated.[17] The sensitivity of the angle-coefficients C_θ and C_ϕ to their corresponding angles (i.e., local angle coordinates θ and ϕ, described in detail later in this work) is evident in Figs. 1.2 and 1.3. A data-reduction algorithm for any generic port arrangement was developed. The performance of the developed coefficients and data-reduction procedures was demonstrated for the 18-hole probe.[17]

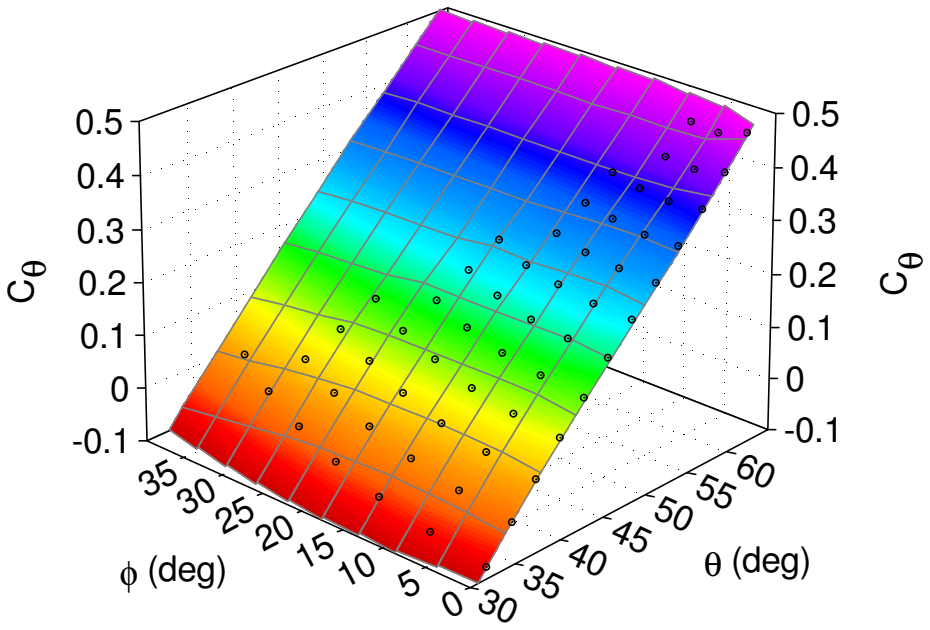

Fig. 1.2 Typical behavior of cone angle coefficient for a sector[17].

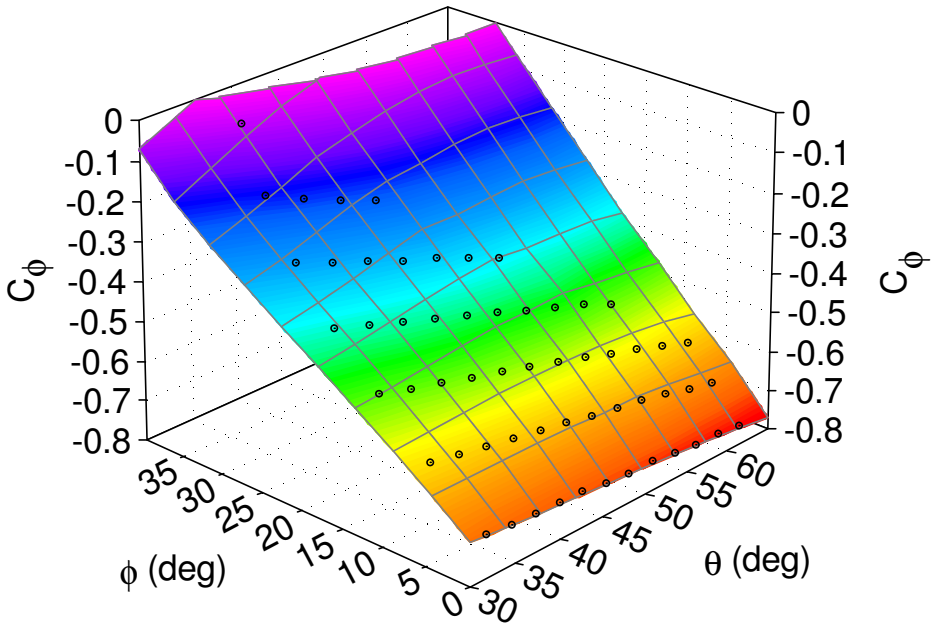

Fig. 1.3 Typical behavior of roll angle coefficient for a sector[17].

The range of measurable flow angles (with respect to the probe axis) for the 5- and 7-hole probes is limited – typically, 55° and 70°, respectively. Hence, they cannot be used in many complex flow fields (e.g., flow behind a backward facing step). For such flows, the omni-directional probe,[18] developed in recent years (Fig. 1.4), is preferred. Thus the range limitation was nearly eliminated by the introduction of this 18-hole, nearly-omni-directional probe, which has eighteen pressure ports distributed on a spherical probe tip.

1.2 OMNI-DIRECTIONAL FLOW FIELD MEASUREMENTS

The operation principle of the 18-hole probe (Fig. 1.4a) is based on the fact that the ports, when properly combined in six groups of five, form a network of 5-hole configurations (some ports/holes are shared by two groups). Each one of these configurations operates as a 5-hole probe. Each one of the 5-hole configurations can be calibrated to provide accurate measurement of any velocity vector within a cone angle of 60°, i.e., any velocity vector with $\theta_i \leq 60°$, where θ_i measures from the axis of the i^{th} 5-sensor configuration (i = 1…6). This axis is defined as the line that connects the central

port of the configuration to the center of the sphere. If all six configurations and their measurement ranges are now combined, any possible velocity vector can be accurately measured.[18] Fig. 1.4b presents a picture of the probe tip, showing some of the surface ports and illustrating how the sting protrudes from the spherical head. Having the sting intersect the sphere at the geometric center of three adjacent 5-sensor configurations minimizes the effect of sting interference. Each of the tip surface ports is routed through the base of the sting. Fig. 1.4c presents a picture of the base of the sting, illustrating the pattern of the sting base holes. Each one of the sting base ports is connected to a stainless steel tube which is subsequently connected, typically through plastic tubing, to a pressure sensor. Fig. 1.4d shows a picture of a fully assembled 18-hole probe.[18]

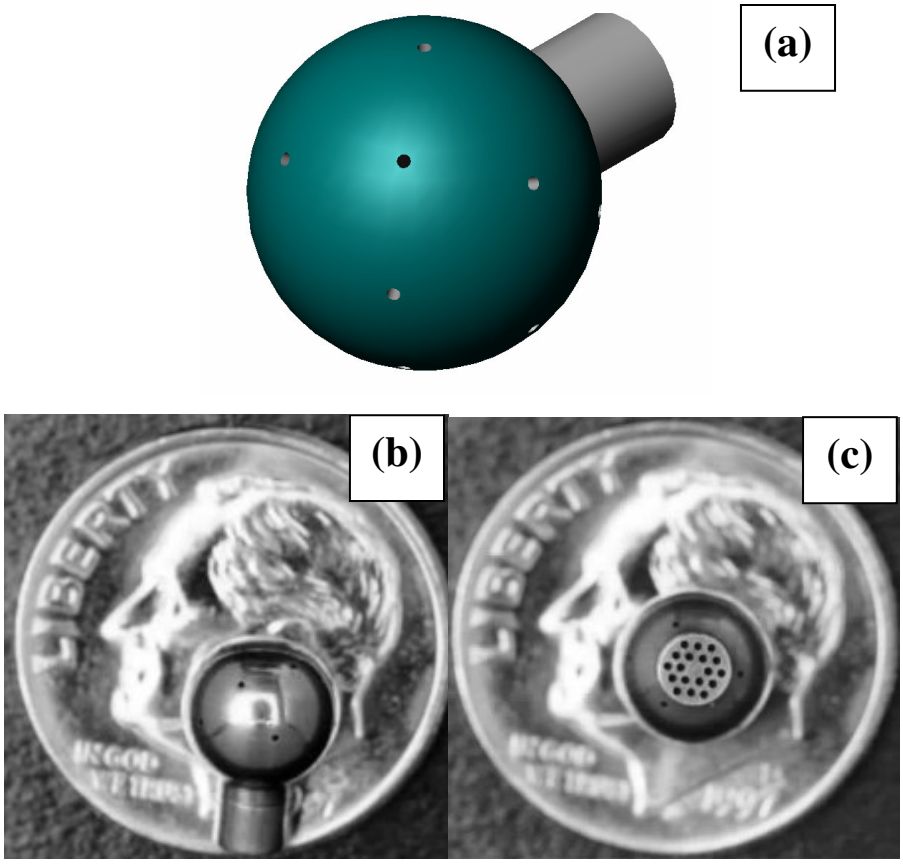

Fig. 1.4 The 18-hole probe: (a) port arrangement, (b) spherical tip, (c) cylindrical sting base and (d) a fully assembled 18-hole probe.

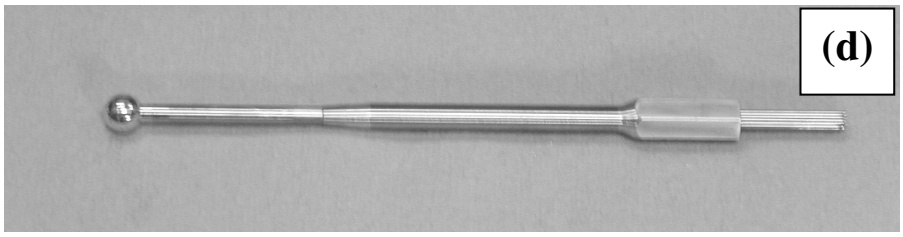

Fig. 1.4 (continued).

The 18-hole probe is essentially an extension of the 5-hole probe design. The design was driven by the necessity to use the reduction method of a conventional 5-hole configuration, the only method available at the time. As a result, over a large region of its measurable range, there are more than four ports available with valid (attached-flow) pressure data. Since there are typically only four unknown variables during flow measurement, there is a redundancy in the number of ports in the 18-hole probe. When new calibration and reduction algorithms[17] were developed that could tackle any generic arrangement of ports, it became possible to consider designing an optimized version of the omni-directional probe which was free of redundancy – i.e., a new 12-hole design. These algorithms do not depend on the axisymmetry of the port distribution pattern to define the non-dimensional pressure coefficients. Moreover, they eliminate the need to separate the measurement domain of a probe to "low-angle" and "high-angle" regimes, typical in conventional 5- and 7-hole probe algorithms that require two different sets of pressure coefficient definitions and procedures. The algorithms were first tested for their prediction capability with 18-hole probe data and were found to give flow prediction more accurate than earlier conventional methods.

The 12-hole probe design's preliminary feasibility study was done earlier in the author's Master's thesis. In this work it was fabricated and calibrated and its workability proven. The design is based on the classic question in physics known as Thomson's problem[19] which consists of distributing N unit charges on a sphere such that the Coulombic potential is a minimum.[20] The potential (V) is described by the familiar equation:

$$V = \sum_{j=1}^{N} \sum_{\substack{i=1 \\ i>j}}^{N} d_{ij} \qquad (1.1)$$

where N is the number of point charges and d is the distance between points i and j (in this case, on a sphere). Many standard solutions for a wide range of N values have been researched and are well-documented.[21, 22] For our purpose, it was required to find the smallest N such that at any point on the sphere there are always four ports within approximately 85° (the laminar flow separation angle for a sphere). This is achieved with N = 12. In fact, by inspecting 18-hole calibration data, it was observed that pressure values begin to deteriorate due to separated flow at ports in the range of 80° and above. For N = 12, the farthest any stagnation point will get, among its nearest four ports, is 81.2°, which is acceptable. This 12-point distribution corresponds to the vertices of an icosahedron (one of the only five regular polyhedra) shown in Fig. 1.5.

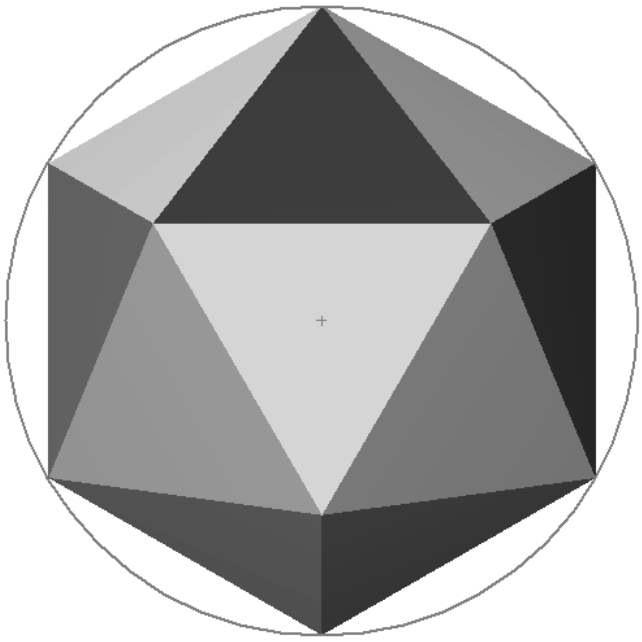

Fig. 1.5 Icosahedron inscribed inside a sphere. The ports of the 12-hole probe are located at the twelve vertices of the icosahedron.

The new 12-hole design for omni-directional measurement, presented in this work, offers several advantages over the 18-hole probe. It allows the calculation of the four unknown flow quantities, i.e. the two flow angles, the velocity magnitude (U_{mag}) and the static pressure (P_s), with the minimum necessary number of holes/ports on the probe tip. The flexible reduction algorithm, that worked very well for the 18-hole, could easily be adapted for this probe. The fewer number of holes helps in achieving significant benefits in terms of the instrument's spatial resolution, frequency response, cost of fabrication and pressure-sensor interfacing.

1.3 PROBE CALIBRATION ALIGNMENT ERRORS

When calibrating multi-hole velocity probes in a wind-tunnel, an offset (or bias) error often exists in the recorded flow angles due to errors in aligning the traverse system exactly with the flow direction and due to the angularity of the tunnel flow itself. These offset angles are hard to quantify from direct measurements with any degree of accuracy. Although they are usually small (less than 0.5° in most good calibrations), these errors still need to be corrected in order to increase the flow measurement accuracy of the probe. Some earlier studies include Clark et al.[23] who corrected for asymmetry of the ports in 5-hole probes due to manufacturing imperfections. It was applicable only if the probe could be pitched and yawed in the flow. Gonsalez and Arrington,[24] during their development of 5-hole probes, did similar studies of probe bias angles and found offsets (or biases) as high as ±0.6° in pitch and yaw. Their idea of the use of symmetry in two configurations of the probe – a second configuration in which the probe was rolled by 180° with respect to the first – was useful for the new method developed in this work. Their scheme was, however, ineffective for typical flow studies where the probe is used in non-nulling mode i.e., fixed with respect to the flow and data (flow speed and direction) obtained relative to the probe.

Zeiger and Schaeffler[25] fully addressed the issue of offsets in straight multi-hole probes whose calibration was typically done in cone-roll coordinates. They defined an offset

coefficient same as the yaw-angle coefficient (C_β) and used a symmetry condition, similar to that in Clark et al.,[24] to compute both vertical and horizontal offsets. Based on these offset values, the angles recorded in the raw calibration data were corrected. Their method, however, proved ineffective especially when applied to spherical-head probes like the 18- and 12-hole probes. In some cases, it had inconsistencies and high errors even when applied to 5- and 7-hole probes. One of the sources of error could be their offset coefficient definition itself which used all port pressures, while the offset depended only on the pressure of any one port. This could lead to higher uncertainties due to contributions from all the variables involved. Moreover, the method calculated offsets iteratively, but it corrected the calibration data for both offsets simultaneously (in each iteration) which is not desirable as was observed when developing the new method in this work. Furthermore, their method found the port locations (or angle coordinates) by simple averaging which can also be a source of error. Finally, only a linear fit was used in their offset plots. This could also be a source of error as is demonstrated later in this work. Since probe reduction techniques have come a long way since this earlier method, the higher prediction accuracy of current-generation probes requires a commensurate offset angle correction.

In this dissertation, an offset-correction algorithm is developed that computes bias (offset) angles in all types of multi-hole probes – from the traditional 5- and 7-hole probes to the omni-directional 18-hole probe and the next-generation 12-hole probe – using simply the pressure data obtained during their calibration. A mathematical expression, involving the original calibration angles and the predicted offset angles, was derived with which the calibration data can be corrected before the probe is put into use. The method faired well under tests for robustness and consistency with a multitude of experimental calibration data. The method, when compared to the earlier method, was found to perform much better in terms of accuracy.

1.4 PROBES IN UNSTEADY AND REVERSED FLOWS

As mentioned earlier, 5- and 7-hole probes typically measure flows that are within 75° with respect to the probe axis. If the flow happens to be beyond its working range, the probe fails to identify it. In other words, the probe could be facing the wrong direction and there is no way to know it. This can be a big disadvantage since this could cause the probe data being measured to be used as proper or valid data, when ideally the data should be marked as being beyond the probe's angular range and not used at all.

Thompson and Hackett,[26] while working on ways to increase the workable range of 7-hole probes using three-dimensional maps, ran into serious risks of the above problem happening. Several methods of discriminating between the valid and invalid data points were tried. While each of the methods held some promise, none were developed into a practical procedure.

Pisasale and Ahmed[27] directly addressed this problem for a 7-hole probe. They used a combination of non-dimensional coefficients and an error term based on these coefficients. The magnitude of these error terms, calculated based on experimental calibration data, would indicate if the flow was beyond the range. They carried out experiments in a flow behind a backward facing step and were able to validate their method to some extent. The new method developed in this dissertation is along similar lines as the work by Pisasale and Ahmed.[27] It should be noted, however, that the method in this work was developed independently since the author was unaware of their work which was published around the same period as the conceptual stages of this method.

A few comments on the differences between the two methods are in order. Our new method was developed for straight probes for which the calibration is typically done in cone-roll (Θ, Φ) coordinates. Their work on the other hand used pitch-yaw coordinates (α, β) which is known to be erroneous for data-reductions at high angles of attack.[15] The coefficient developed in this work could cover a range of reversed flows up to 150° all

by itself. They used 2 sets of coefficients – one for the range of $|\alpha| < 125$ and another for higher pitch angles. Their technique became unwieldy for $|\alpha| > 125$ because their coefficients required an estimate of the actual dynamic pressure of the flow, which is typically unknown when the probe is being used in flow studies. It required the probe to be rotated by 180°, if the experimenter was in doubt of the direction of the probe, and check the pressures again in order to judge the validity of either data set. This is highly impractical in terms of time and effort, especially for flow studies in which data is acquired over a period of time with the probe fixed in a particular direction. In such cases, only the validity of each data point is needed for analysis during post-processing of the data. Corrective measures or a re-run with a different orientation of the probe can be undertaken subsequently if and when required.

If a multi-hole probe is being used in steady flows or in a flow with low-amplitude low-frequency fluctuations, the measured port pressures can be directly used in the reduction algorithm and the flow properties calculated. But most probes have some amount of pneumatic tubing that communicates the pressure from the probe surface to the sensors. Pressure waves tend to attenuate from one end of a tube to another based on the flow oscillation frequency.[28, 29] To this end, an experimental set up in our research group[30] was upgraded to measure, up to 3 kHz, the response of different probe tubing assemblies. The setup uses two speakers to cover the range of frequencies of interest. This acoustic calibration facility could handle two or three pressure ports simultaneously thus greatly cutting down on the run-times. A 7-hole probe could be calibrated for acoustic response in three runs and a 5-hole probe in just two runs. With powerful mathematical (software) tools such as Matlab, the theoretical study of the frequency response, their corresponding transfer functions and other aspects can be studied easily. With this correction for frequency response, the probes can be used in turbomachinery flows[31, 32] where high unsteadiness is encountered.

A common problem experienced by all users of multi-hole probes is port blockage due to debris in the flow field. The severity of the problem depends on how clean the flow is. Wind speed measurement probes, such as the one developed here, due to their outdoor application, are susceptible to frequent maintenance checks for port blockage and cleaning depending on the nature of the test site. But before such corrective steps can be taken, the blockage has to be identified and the data, taken after the blockage, has to be corrected or flagged as bad points. Of course, it is not necessary that all the data points need to be corrected because the blockage might have occurred only at a few ports outside the range of influence of the velocity vector, i.e., on the leeward side and hence not used by the reduction algorithm. A preliminary study addressing all these issues and how to upgrade the reduction algorithm to account for port blockages was conducted and is presented in this work.

For spherical tip geometries, the main two sources of errors are inertial (potential flow) effects and spatial velocity gradient effects as found by Humm et al.[33] They found that errors due to viscosity and circulation were much less significant. Only a quasi-steady calibration of the probe performed in a wind-tunnel is available. Therefore, when the probe is in use, even if all tubing was eliminated and sensors installed right at the surface, unsteadiness in the flow can still change the port pressures due to what is commonly known, in fluid dynamics, as inertial effects. This error in pressures obviously leads to errors in calculated flow properties and hence a correction has to be done to the calculated properties during reduction. In other words, for the probe in unsteady flow, the steady probe calibration can generally not be used directly to accurately reduce the instantaneous measured pressures to the instantaneous flow properties. Johansen and Rediniotis[34-36] developed theoretical and experimental techniques to address this problem. Based on their theoretical model, a new simpler and faster strategy to correct for inertial effects is presented in this work and the technique applied to the Weatherprobe. One of the main features of this new technique is that it does not need time series data. The correction is performed on the calculated values at

each time step independently. Moreover, the increase in sampling rate (up to 40 times) that was needed in the earlier method is completely avoided.

1.5 ANEMOMETERS

The 12-hole probe proved to work well for omni-directional flow studies in wind-tunnels and can replace the 18-hole. This led us to consider developing a probe for wind speed measurements – a pressure-based anemometer – that would work on the same principles and take advantage of the newly-developed reduction algorithm.[17] There is a good market for high-accuracy three-dimensional anemometers especially in harsh weather environments. Our experience with pressure-based multi-hole probe technology can be summarized as follows:

1. a new robust algorithm for any generic port arrangement.
2. development of an optimized probe for omni-directional flow field measurements – 12-hole.
3. refinements in calibration procedures (such as correction of alignment errors) and data-processing to attain very high measurement accuracies.
4. sophisticated techniques (experimental and numerical) to correct measured flow properties in unsteady flow fields.
5. good handle on the measurement uncertainties and sensitivities originating from various sources of error in pressure-based flow-field studies.
6. expertise in probe fabrication and associated instrumentation.

But all this technology was applied thus far exclusively to flow field studies in wind-tunnels and internal flows within the confines of laboratory walls. There is a whole domain in meteorological research which needs data in the atmosphere of quantities identical to what are currently being measured. The need to measure wind speed and direction with high accuracies suggests new frontiers for multi-hole probe technology. To this end, a pressure-based probe in the same lines as the omni-directional 12-hole probe can be designed anew with the following factors in mind:

- environmental factors such as rain limit our freedom of choice of pressure-port locations, pressure tubing etc.
- the instrumentation associated with traditional wind-tunnel probes is not viable outdoors. It should be able to withstand the harsh environments in which meteorological research is typically carried out.
- the instrumentation should be stand-alone and make real-time data accessible remotely.
- the probe itself should be unaffected in precipitation and icing conditions.

Although many 3-D wind measurement instruments exist in the market, they are plagued with many limitations in terms of accuracy, robustness and reliability. A competent wind speed instrument at a compelling low price has immense marketability in not just meteorological research but also in many other fields such as

- wind-energy potential estimates necessary in surveys for development of wind farms
- ski-resorts where remote access to wind speed data at another location is very useful
- structural load evaluations on tall buildings to analyze viability of their design

It is prudent at this point to survey other existing wind speed measurement technologies and evaluate the state of the art which will help in finalizing the design parameters and goals for our new instrument. Rotational cup anemometers[37] are the traditional favorites. Thanks to their simple design and easy-to-use attribute, they have been widely used throughout the last century. The cup anemometer works on the simple principle of converting the "rpm" of the rotor to wind speed – a linear relation. Once the instrument is calibrated in a wind-tunnel to find this relation, it is ready for use.

Common cup anemometers have a serious limitation in icing conditions because they tend to get freezed up and the rotor stalls thus providing no data. Some new ones are equipped with a heater base plate that serves to alleviate the problem of icing to some extent. But the effectiveness of this has been found to be highly suspect by many

researchers.[38] If the use of the cup anemometer is limited to lowland (no icing) weather stations, there is still the crippling lack of wind speed data in the vertical direction. Even more importantly, if there were a vertical component in the wind velocity, errors are introduced in the instrument's horizontal component read out.[39] "Off-axis errors" is the common terminology for this occurrence. This can be quite problematic in hilly/uneven terrains. Finally, the instrument's applicability, if one needs to capture turbulence in the flow, is very limited mainly due to inertia of the rotor. There are some studies that address correction of this problem,[40] but these are analytic and not backed by wind-tunnel or field tests. Lockhart[41] calculated performance characteristics of a cup anemometer based on standard methods prescribed by the ASTM program for meteorological instruments.

To side-step problems of icing, some new probes were designed that used the drag on a sphere to calculate wind speeds.[42] These probes had no moving parts and hence had better mechanical reliability. This also made it easier to resolve the problem of keeping the probe ice-free by installing heating elements inside the sphere. Force balances or sensors embedded inside the probe measured the two components (in the azimuthal plane) of wind-force (or drag). The velocity magnitude in the resultant direction was calculated based on the drag coefficient of the sphere known from theory or experiment. The probe still had limitations as regards the vertical component. The quadratic dependence of the measured force on the wind speed and the lack of proper calibrations undertaken by the designers resulted in poor prediction capabilities. In spite of the rugged quality of its design, the probe did not find much favor among researchers due to its low accuracy.

The top spot for high-accuracy 3-D wind speed measurement is currently held by the sonic anemometer.[43] The basic principle of the instrument is to find the time taken for sound waves to travel over a known distance (in a known direction) and thus compute the speed of sound. The flow speed in that direction would depend on the speed of sound

calculated. An emitter and a receiver are used to transmit sound waves and the electronics within calculate the time lag. The air temperature is measured by a separate sensor in order to compute the still-air speed of sound. The above would constitute only a 1-D wind speed read out. If three emitter-receiver pairs are used, three-component wind speeds can be calculated (with appropriate coordinate transformations).

Although manufacturers of recent designs claim accuracy of 2-3% in measured wind velocity magnitudes, field tests[38] peg it higher at about 5%. Many recent models are equipped with optional internal heaters to prevent icing in low-temperature applications. Suspicions of poor performance in cloudy conditions were laid to rest by the work of Siebert and Teichmann,[44] but the instrument's performance at high wind speeds (above 50 m/s) and heavy precipitation is still highly suspect. Its applicability to turbulent flow fields, although much better than cup anemometers, is limited to data acquisition at 10 Hz.[45] This rate is small when considering the fact that some weather stations, such as the Mt. Washington observatory, have expressed the need to analyze wind data obtained at 100Hz or more. There are also issues of flow distortion due to structural design (i.e., supporting structures of the instrument) which are not accounted for with any wind-tunnel tests. Lastly, sonic anemometers designed for an all-encompassing application are steeply priced upwards of $8000. When essential accessories like a data-logger and a computer (for post-processing) are included, the total cost can be as high as $15000. Hence, there is a need for a competitively priced all-weather anemometer – a tower-mountable instrument that can provide good-accuracy wind velocity (all three components) and is capable of withstanding hostile environmental conditions.

The anemometer developed in this work (called 'Weatherprobe' from here on) strives to achieve all the desirable attributes described above. This probe was developed from scratch although it shares basic working principles with the 12-hole. This design also (coincidentally) has twelve ports, albeit in a different arrangement i.e., closer to the equator so as to avoid water getting into the ports and is a lot bigger (6 in. spherical

head). The prototype probe is internally heated and can measure accurate 3-D wind data at up to 100Hz.

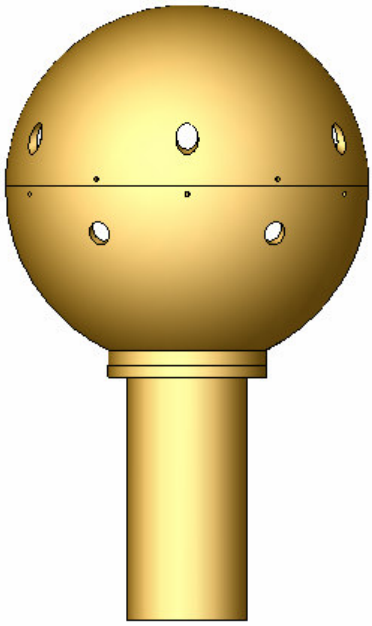

Fig. 1.6 The Weatherprobe.

The probe has a 12-port arrangement around the equator (Fig. 1.6) with a pressure sensor at each port. Coincidentally, the number of ports is the same as the "12"-hole omni-directional probe, but the port arrangement is different. All pressure sensors, heating elements and thermocouples reside inside the 6-in spherical aluminum head. The cylindrical support/shaft can be modified to conform to different mounts. Temperature controllers read in the temperatures and provide (PID) feedback control to the heating elements. The heating elements de-ice the pressure conduits and maintain the outer surface at ~5°C. The data-acquisition system is a stand-alone PC104-based IDAN module (16-bit resolution, 100 kHz throughput) which reads in the pressure data and generates high-accuracy wind data using a newly-developed reduction algorithm. The wind data thus obtained is stored in the Daq module's 20GB temporary storage for access through the Ethernet. All control inputs, data acquisition and post-processing are

handled by an easy-to-use windows-compatible GUI developed in Microsoft Visual C++.

The probe was extensively calibrated over a wide range of speeds in a low-speed wind-tunnel prior to usage. The probe was tested again with all the associated instrumentation (a "dry run") in a different wind-tunnel to get the final error estimates and to check full-configuration workability. Further, artificial rain was simulated in the lab to study the effects of rain and quantify corresponding errors, if any, in the measurement. Following this, the probe was set up for field tests next to a sonic anemometer for direct comparison of its capabilities.

In various parts of this work, "theoretical" data of flow over a sphere is used for analysis. This data is the pressure data obtained from an empirical equation for C_p (non-dimensional pressure coefficient) for laminar viscous flow over a sphere, as given in White[46]:

$$C_p = 1 - \left(\Theta \cdot (1.5 - \Theta^2 \cdot (0.4371 - \Theta^2 \cdot (0.1481 - \Theta^2 \cdot 0.0423)))\right)^2 \qquad (1.2)$$

Θ in the above equation is the angular location (on the sphere surface) of the point of interest with respect to the stagnation point.

In this work, the groundwork covers the fabrication and calibration of the 12-hole omni-directional probe (section 2). The application of reduction algorithms (recently developed in an earlier work) to this probe served as a validation of the algorithm's high accuracy prediction when applied to random arrangement of ports. The design and development of the Weatherprobe is carried out in two phases (sections 3 and 4). Errors in alignment are a big source of error in multi-hole probe calibrations and a new method to correct for it is extensively studied in section 5. Some miscellaneous issues related to error corrections in pressure probes such as point validation due to range limitation, Reynolds number effects and inertial effects are studied and solutions prescribed in the penultimate section.

2 OMNI-DIRECTIONAL FLOW FIELD MEASUREMENTS: 12-HOLE PROBE

2.1 DESIGN AND FABRICATION

The 12-hole probe design is based on the classic question in physics known as Thomson's problem which consists of distributing N unit charges on a sphere such that the Coulombic potential is a minimum.[20-22] For our purpose, it was required to find the smallest N such that for any stagnation point on the sphere, there are always four ports within ~85° (the laminar flow separation angle for a sphere) from it. This is achieved with N = 12. The farthest any stagnation point will get from its nearest four ports is 81.2°. In other words, a distribution of N = 11 ports around a sphere would have regions where the stagnation point does not have four ports in the attached-flow region. The 12-point distribution corresponds to the vertices of an icosahedron (canonical shape with twenty sides - each one of which is an equilateral triangle - and twelve vertices) shown in Fig. 1.5. Thus the geometric definition of the icosahedron helps in easily defining the port locations.

Solid models of two possible designs based on sting location are shown in Figs. 2.1 and 2.2. In Fig. 2.1, the center of the sting is located at the geometric center of any two adjacent ports; while in Fig. 2.2, the center of the sting is located at the geometric center of any three adjacent ports. These two configurations will be referred to as the two-port and the three-port sting configuration, respectively. In both configurations, the locations of the tip ports are described in a spherical coordinate system, as defined in Fig. 2.3. For the two-port and three-port sting configurations, the locations of the tip ports are given in Table 2.1 and Table 2.2, respectively, in terms of their Θ and Φ coordinates.

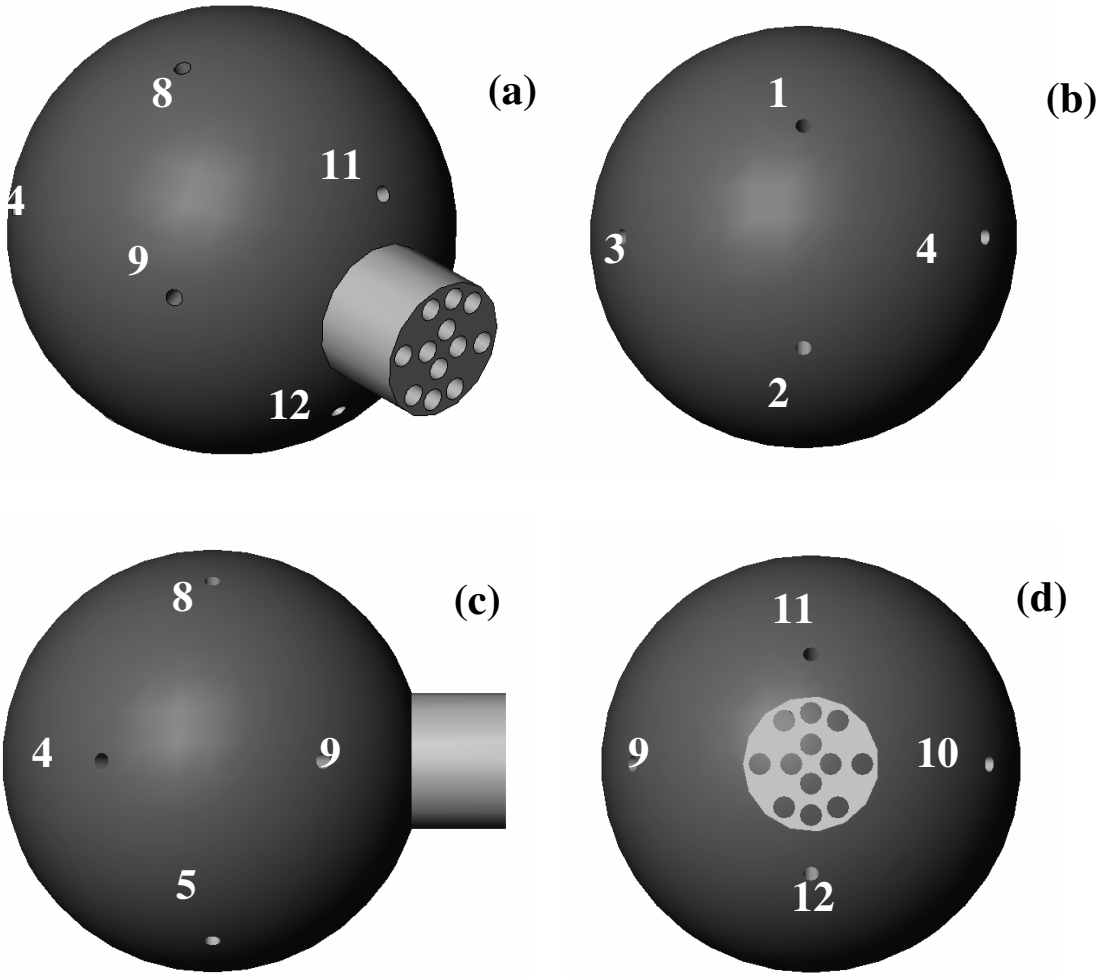

Fig. 2.1 Model of the 12-hole probe for two-port sting configuration: (a) perspective view, (b) front view, (c) side view, (d) back view.

For the two-port sting configuration, Fig. 2.1 presents a perspective view of the tip (Fig. 2.1a), and front, side and back views of the tip (Fig. 2.1b, Fig. 2.1c, Fig. 2.1d respectively), illustrating the location and numbering of the ports. Although ports 6 and 7 are not shown, they are located diametrically opposite ports 8 and 5 respectively. Fig. 2.1d also illustrates the arrangement of the holes on the base of the sting.

Table 2.1. Tip port coordinates for two-port sting configuration.

Port#	Θ (deg)	Φ (deg)
1	31.7	0.0
2	31.7	180.0
3	58.3	270.0
4	58.3	90.0
5	90.0	148.3
6	90.0	211.7
7	90.0	328.3
8	90.0	31.7
9	121.7	90.0
10	121.7	270.0
11	148.3	0.0
12	148.3	180.0

As it was previously mentioned, each one of the sting holes communicates with one of the tip holes/ports. The arrangement of the sting holes is very important because it ultimately dictates the minimum possible sting diameter, which, in turn, affects the maximum possible measurable flow angularity of the probe. The design here was based on a 3/8 in. tip diameter, a 0.014 in. tip hole diameter and a 0.020 in. sting hole diameter. The selection of the tip hole diameter was based on our experience with the 18-hole probe in terms of the minimum possible tip hole diameter that will not suffer from port clogging problems and will yield a reasonable measurement frequency response. Once 0.014 in. was selected as the tip hole diameter, this automatically dictated a minimum of 0.020 in. sting hole diameter, based on the availability of stainless steel tubing in the market. As discussed earlier, each hole in the sting base mates with a metal tube which ultimately connects each of the tip ports to a corresponding pressure sensor. The minimum-wall-thickness, 0.014 in.-I.D. stainless steel tube available in the market has an O.D. of 0.020 in., hence the selection of the sting hole diameter. The geometric values

chosen above and the fact that, for fabrication reasons, there has to be a distance of at least 0.005 in. between the edges of adjacent sting holes, dictate the optimal sting hole configuration (optimal in terms of minimizing sting diameter) shown in Fig. 2.1d. For the two-port sting configuration, the minimum possible ratio of sting diameter to tip diameter is 0.324. If this is compared to the corresponding ratio for the 18-hole probe (0.347), it can be seen that the sting is smaller for the 12-hole probe case, resulting in reduced sting interference and increased measurable flow angularity.

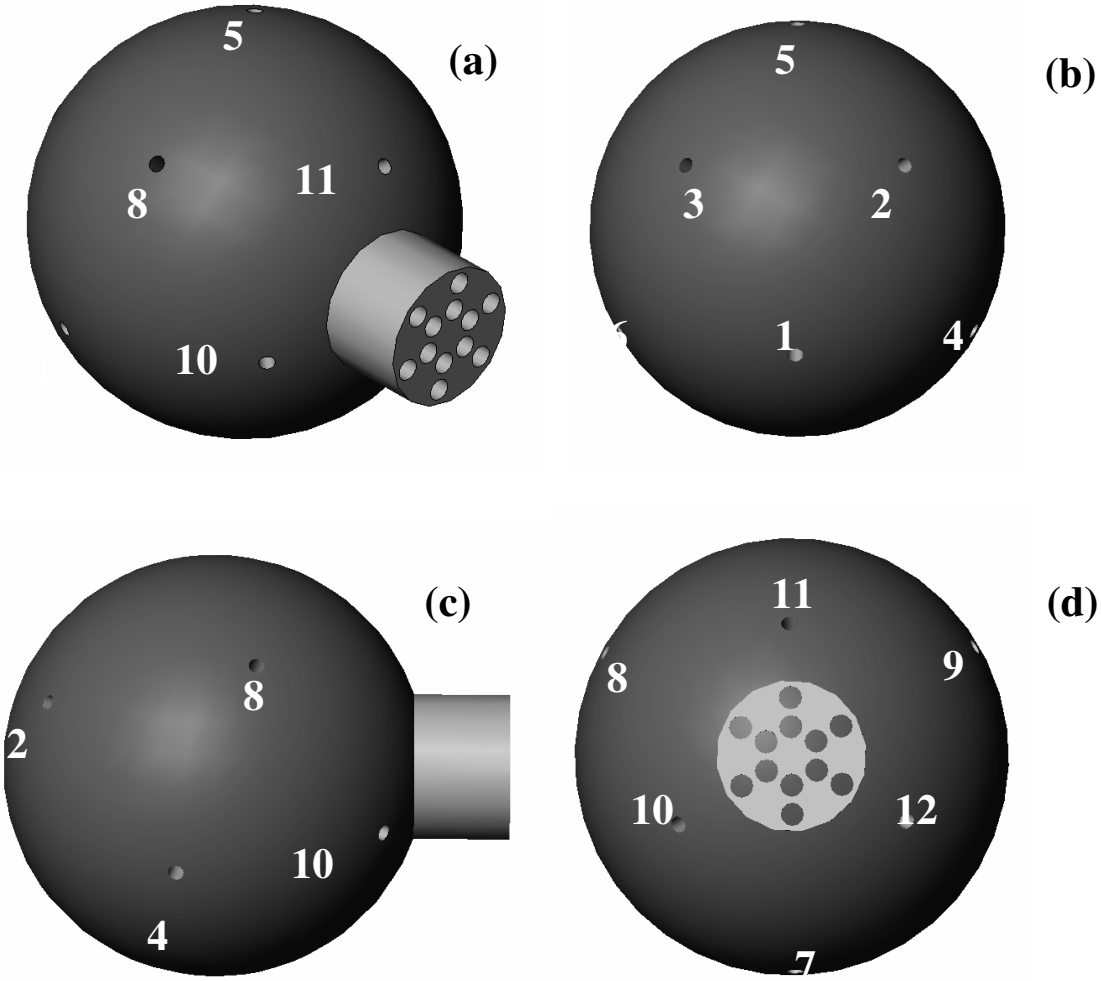

Fig. 2.2 Model of the 12-hole probe for three-port sting configuration: (a) perspective view, (b) front view, (c) side view, (d) back view.

Table 2.2. Tip port coordinates for three-port sting configuration.

Port#	Θ (deg)	Φ (deg)
1	37.4	0.0
2	37.4	120.0
3	37.4	240.0
4	79.2	60.0
5	79.2	180.0
6	79.2	300.0
7	100.8	0.0
8	100.8	120.0
9	100.8	240.0
10	142.6	60.0
11	142.6	180.0
12	142.6	300.0

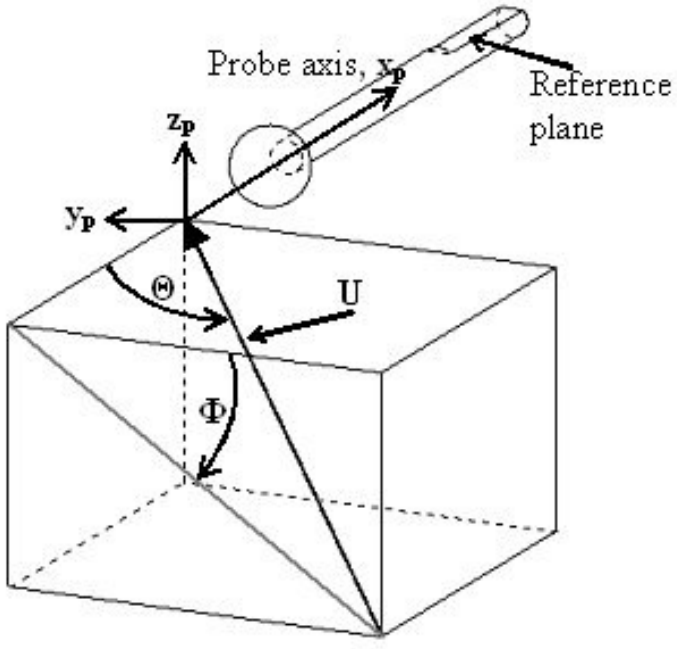

Fig. 2.3 Global coordinate system for the probe.

For the three-port sting configuration, Fig. 2.2 presents a perspective view of the tip (Fig. 2.2a), and front, side and back views of the tip (Fig. 2.2b, Fig. 2.2c, Fig. 2.2d respectively), illustrating the location and numbering of the ports. In this case all ports are shown. Fig. 2.2d also illustrates the arrangement of the holes on the base of the sting. For the three-port sting configuration, this sting hole arrangement is optimal (for the same tip, tip hole and sting hole diameters, i.e. 3/8 in., 0.014 in. and 0.020 in., respectively), although, as expected, it is different from the optimal sting hole arrangement of the two-port sting configuration. The resulting ratio of sting diameter over tip diameter is 0.347. As seen here, the minimum sting diameter for the three-port sting configuration, is a little bigger than the minimum sting diameter for the two-port sting configuration and the same as the 18-hole probe. However, the nearest port to the sting is further away (than that in the 18-hole) thus enabling increased measurable flow angularity.

After weighing the two options, it was decided to go with the two-port sting configuration. A prototype with a 3/8 in. tip diameter and 0.122 in. sting diameter was designed and built for calibration and testing. The probe head was a brass sphere with 0.014 in. holes precision-drilled at the specified locations. The probe sting interferes somewhat with the global symmetry of the spherical probe. However, calibration of the probe includes many points near the sting to alleviate this problem. A picture of the fabricated probe tip is shown in Fig. 2.4.

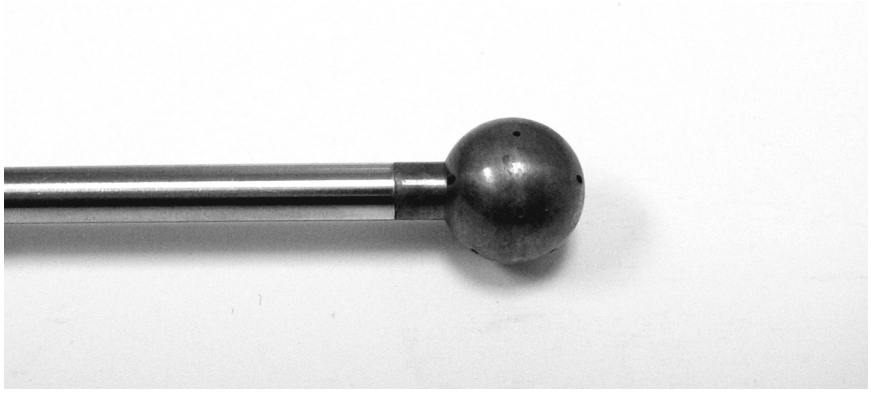

Fig. 2.4 Picture of the 12-hole probe.

2.2 CALIBRATION

If the probe tip were a perfect sphere, the port locations were accurately known, and the spherical symmetry of the tip was not compromised by the presence of the sting, then there would be no need for experimental calibration of the probe. However, the probe tip is not a perfect sphere and probe machining imperfections (especially for small probe tip diameters) make it practically impossible to know exactly the port locations. The above necessitate probe calibration.

The probe was calibrated at the subsonic jet calibration facility of Aeroprobe Corporation at Mach numbers of 0.05, 0.1, 0.3, 0.5, 0.6 and 0.7. The process involves placing the probe in a uniform, perfectly-known flow field (known in terms of velocity magnitude and direction, density, temperature, static pressure) at many different orientations with respect to the known velocity vector, and recording, for each such orientation, the twelve probe tip pressures and the freestream dynamic pressure. The main components of the probe calibration hardware are: the facility that generates the known flow field, the probe indexing system, which automatically places the probe at a series of user-defined orientations and the pressure data acquisition system.

In a typical flow measurement survey, the probe is held at a fixed orientation and the velocity vector changes in magnitude and direction. For practical reasons, during probe calibration, a reverse process is followed: The velocity vector is fixed in magnitude and direction and the probe is placed in different orientations with respect to the velocity vector. This probe placement is automatically achieved by the probe indexing system, or the indexer, for short. During this procedure, the probe tip is always maintained at the same physical location in space. Two stepper motors of the indexer, the cone and roll motors, set the cone (Θ) and roll (Φ) angles, respectively, of the probe orientation (refer to Fig. 2.3 for the cone and roll angle definitions).

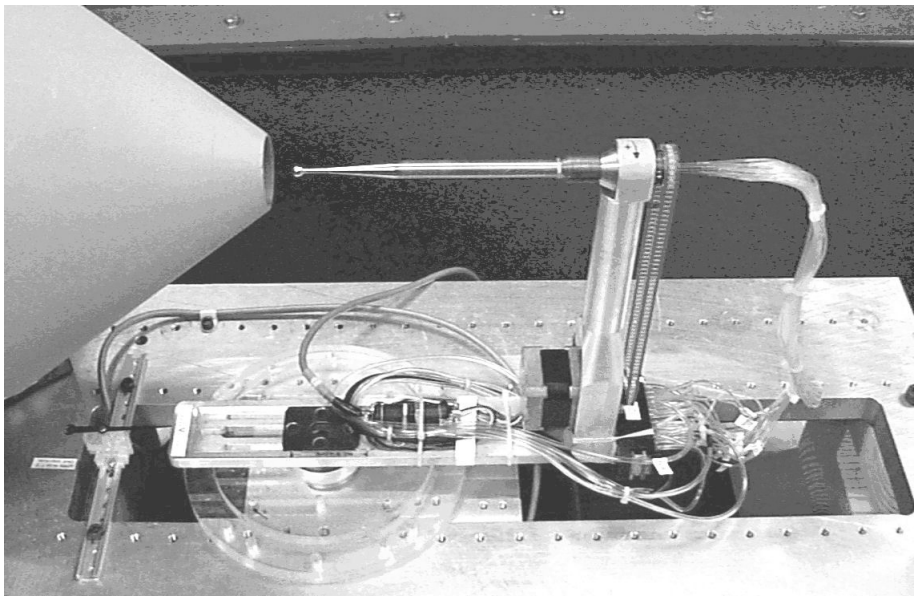

Fig. 2.5 The indexer at the jet facility.

A picture of one of our indexers installed at the jet calibration facility is shown in Fig. 2.5. The cone and roll ranges of the indexer are 0 to 155° and 0 to 360°, respectively. The cone and roll positioning have resolutions of 0.036° and 0.9°, respectively, and are both equipped with position encoders, resulting in position accuracies on the order of 0.001°. It should be noted that the design of the indexer is such that, regardless of the probe orientation, the probe tip always stays at the same point. A typical probe calibration records data for every 3.6° in roll angle and every 2.7° in cone angle. This translates into a total of about 5600 calibration points per velocity magnitude (the cone angle is varied from 0 to 152° and the roll angle from 0 to 360°). The pressure data was acquired using an Electronic Pressure Scanner (ESP) from PSI Inc. The pressure range of the sensor (at each Mach number) was chosen appropriately depending on the calibration dynamic pressure. The probe indexer and the ESP unit are interfaced to a computer that fully automates the entire calibration process.

To assess the accuracy of a calibration, a procedure called “calibration validation” is performed. For this procedure, test data are also collected after each calibration. This

involves positioning the probe at several known orientations, (Θ_{test}, Φ_{test}), none of them coincident with any of the orientations used for calibration, (Θ_{cal}, Φ_{cal}), and collecting the pressure data. These pressures are subsequently fed into the calibration routines and a predicted orientation (Θ_{pred}, Φ_{pred}) is calculated. The difference between the two pairs (Θ_{test}, Φ_{test}) and (Θ_{pred}, Φ_{pred}) is a measure of the calibration accuracy. The accuracy of U_{mag} and P_s are also evaluated for the same. About 1800 such test points were taken.

2.3 REDUCTION ALGORITHM

The preprocessing and reduction technique developed by the authors for a generic arrangement of ports[17] can easily be adapted to the 12-hole probe. The technique was employed earlier for the 18-hole probe with excellent results. In this technique the entire probe domain is divided into sectors of four ports each and non-dimensional coefficients found that relate the flow unknowns to the recorded port pressures.

A generic sector is shown in Fig. 2.6. It is a 2-D representation of the curved surface of the probe showing four ports and the stagnation point (SP). The angles θ and ϕ (smaller case) are the local (sector-specific) coordinates of the stagnation point ('*' in the figure) and constitute two of the four flow unknowns. The highest pressure is denoted by p1, the second-highest by p2 and so on. The local coordinate system is a standard spherical coordinate system with the line joining the center of the sphere to port#2 as the reference axis and the plane containing port#1, port#2 and the center of the sphere as the reference plane. It is elementary to convert θ-ϕ (local) to Θ-Φ (global) since the location of port#2 (the reference port for the local coordinate system) is known (i.e., calculated from calibration data).

The other two unknowns P_s (static pressure) and P_t (total pressure) are non-dimensionalized with an estimate of the dynamic pressure (q_{est}, defined later), as

$$C_s = \frac{p1 - P_s}{q_{est}}, \text{ and} \qquad (2.1)$$

$$C_t = \frac{p1 - P_t}{q_{est}}, \tag{2.2}$$

where p1 is the highest pressure of all four ports in the sector.

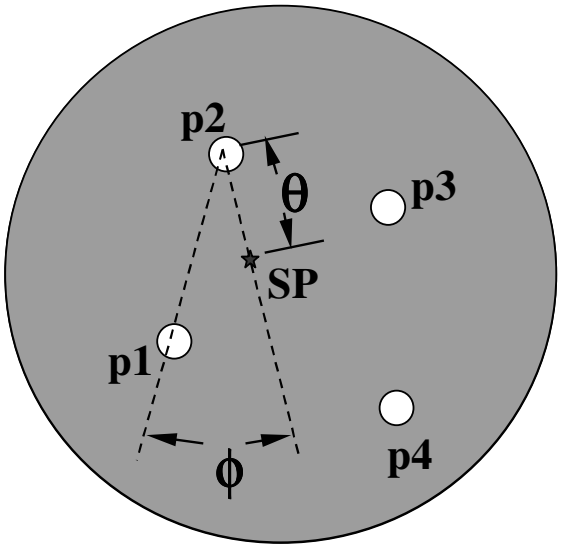

Fig. 2.6 Local (sector) coordinate system for the reduction algorithm.

The four unknowns are then related to the port pressures through two non-dimensional calibration angle-coefficients C_θ and C_ϕ defined as

$$C_\theta = \frac{A_\theta \cdot (p1 - p3) + B_\theta \cdot (p2 - p3)}{R \cdot (p1 - p3) + S \cdot (p2 - p3) + T \cdot (p3 - p4)} \tag{2.3}$$

$$C_\phi = \frac{A_\phi \cdot (p1 - p3) + B_\phi \cdot (p2 - p3)}{R \cdot (p1 - p3) + S \cdot (p2 - p3) + T \cdot (p3 - p4)} \tag{2.4}$$

where, the denominator is an estimate of the freestream dynamic pressure (q_{est})

$$q_{est} = R \cdot (p1 - p3) + S \cdot (p2 - p3) + T \cdot (p3 - p4) \tag{2.5}$$

The coefficients R, S and T are non-dimensional and are defined such that the estimated dynamic pressure (q_{est}) from all the calibration data points in the sector is fairly constant and close to the actual calibration dynamic pressure. The coefficients A_θ, A_ϕ, B_θ, B_ϕ are

also non-dimensional and are defined specific to each sector such that C_θ and C_ϕ are sensitive only to the corresponding angles they represent (θ and ϕ, respectively).

The calibration process (described in the previous section) provides pressure data at many points in each sector. This data undergoes preprocessing before the probe can be used for flow measurements. Preprocessing involves finding the sector-coefficients A_θ, A_ϕ, B_θ, B_ϕ, R, S and T for each sector and the angle-coefficients $C_{\theta\text{-cal}}$, $C_{\phi\text{-cal}}$ for each calibration data point. The procedure to calculate the sector-coefficients starts with plotting the pressure differences p1-p3, p2-p3 and p3-p4 against the local angles θ and ϕ for each sector. These surface plots are sufficiently planar if the sector is defined appropriately and the pressure differences chosen suitably.[17] Hence, from the three linear (surface-fit) equations, with some elementary algebra, the sector-coefficients can be calculated for each sector and stored in a database. The angle-coefficients can then be calculated for all the calibration points using equations (2.3) and (2.4). C_s and C_t are also calculated (using equations (2.1) and (2.2)) and stored in the same database. This preprocessed calibration data can now be used during reduction to solve for the flow properties.

The non-dimensional coefficients for a typical sector of the 12-hole probe were plotted using calibration data at Mach 0.05 for inspection. Figs. 2.7 and 2.8 are plots of the non-dimensional angle-coefficients, C_θ and C_ϕ, respectively. The surfaces are flat and sensitive only to their respective flow angle coordinates. The non-dimensional pressure coefficients – static (C_s) and total (C_t) – are shown in Figs. 2.9 and 2.10. These are well-behaved surfaces with no sharp gradients. Finally the estimated dynamic pressure, q_{est}, is also checked in Fig. 2.11. The surface is nearly constant and close to the calibration data dynamic pressure of 1.24 torr as desired. Note that the x- and y- coordinates in all these plots are the local coordinates (lower case θ and ϕ) of the calibration data points in the corresponding sector. The behavior of the coefficients, as is evident from the plots,

suggests good prediction capability of the reduction algorithm when applied to the 12-hole probe.

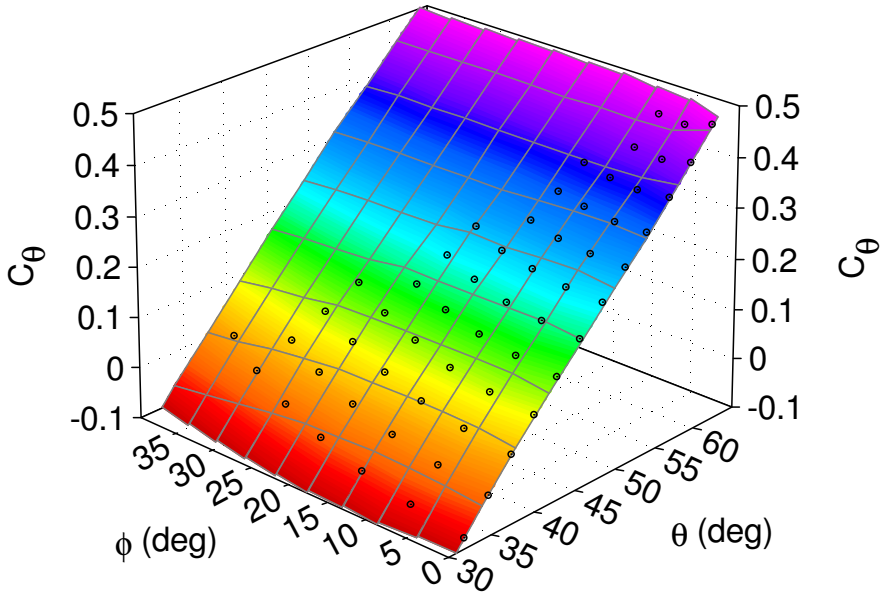

Fig. 2.7 Typical behavior of cone angle coefficient for a sector.

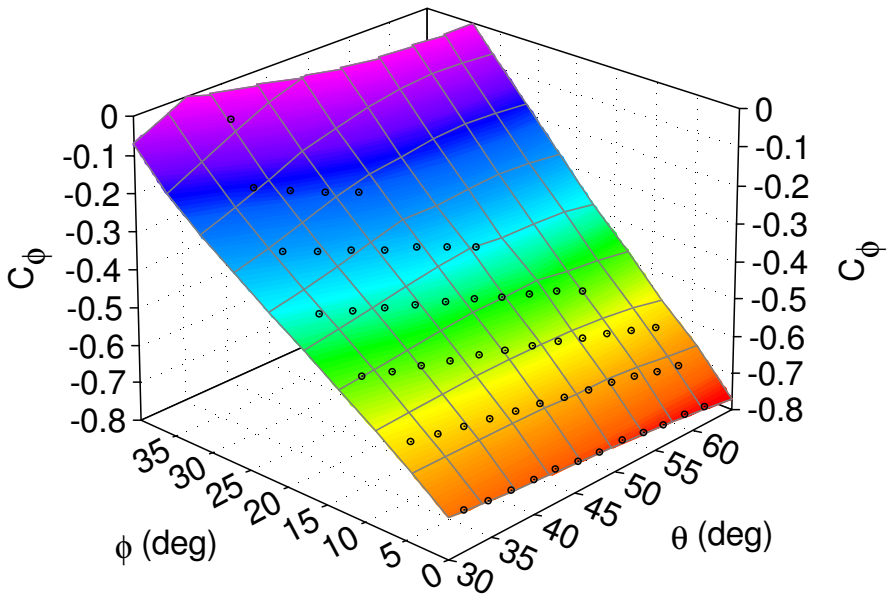

Fig. 2.8 Typical behavior of roll angle coefficient for a sector.

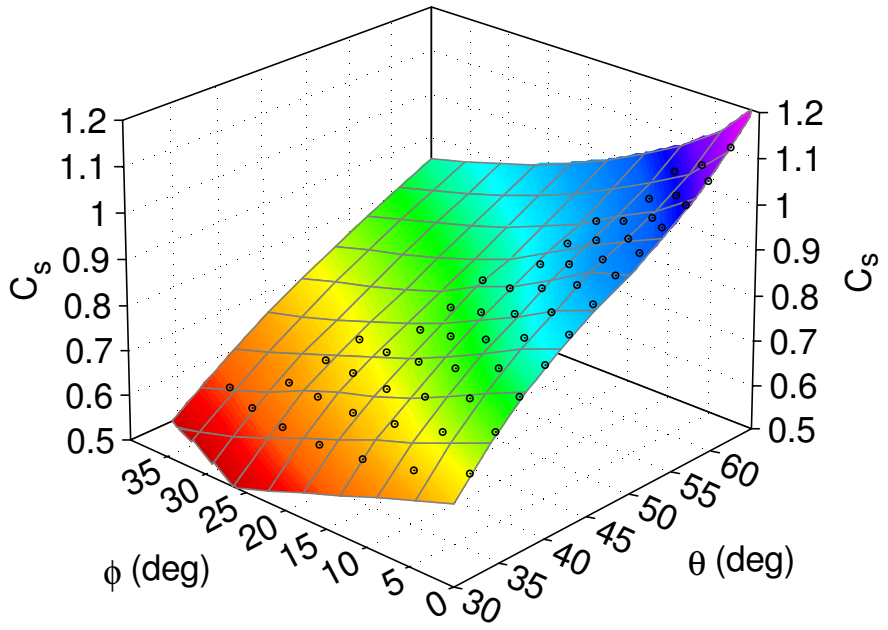

Fig. 2.9 Typical behavior of static pressure coefficient for a sector.

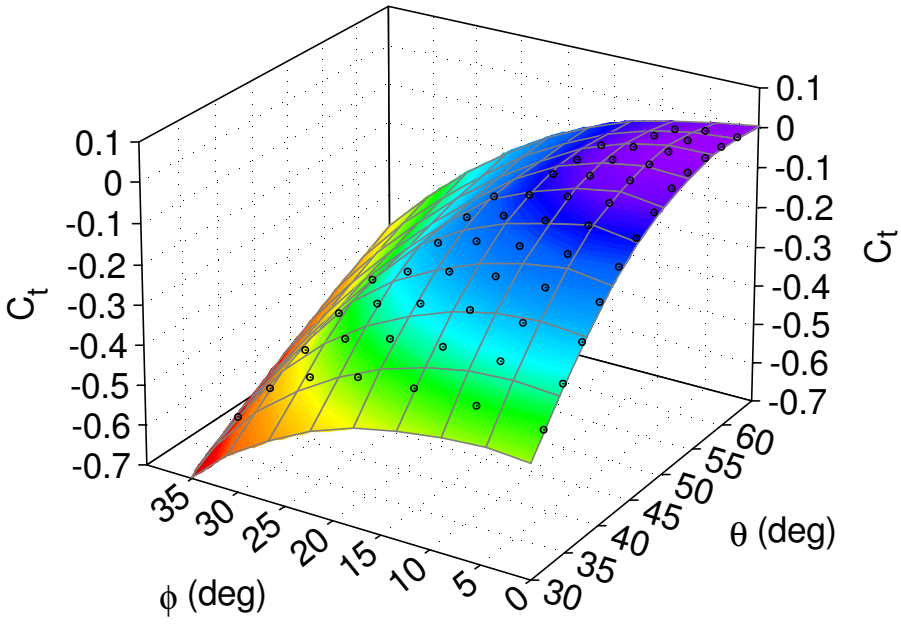

Fig. 2.10 Typical behavior of total pressure coefficient for a sector.

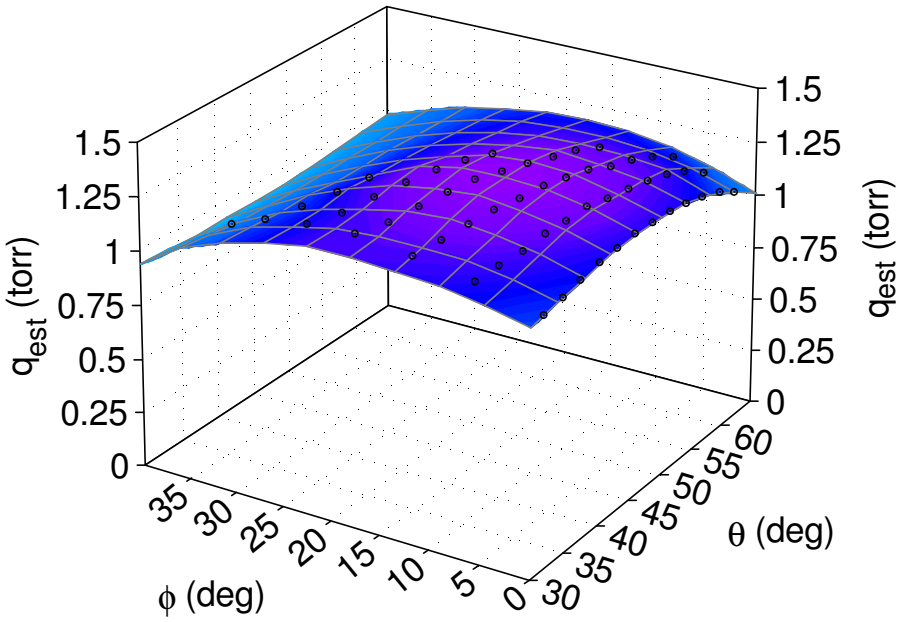

Fig. 2.11 Typical behavior of estimated dynamic pressure coefficient for a sector.

When the probe is inserted in an unknown flow field, for a given flow speed and direction (let's call it a test point), the relevant sector is first identified based on the highest four pressures for that point. The corresponding sector-coefficients (A_θ, A_ϕ etc.) are then obtained from the pre-processed data. Now the angle-coefficients ($C_{\theta\text{-test}}$, $C_{\phi\text{-test}}$) for the test point can be readily calculated using equations (2.3) and (2.4). The preprocessed calibration data is then searched to select calibration points nearest to the test point based on Euclidean distance in the C_θ-C_ϕ plane. Each of the four unknowns is separately related to $C_{\theta\text{-cal}}$ and $C_{\phi\text{-cal}}$ of the selected calibration points by local least-squares surface fits (polynomial expressions).

$$(\theta, \phi, C_s, C_t) = k_0 + k_1 \cdot C_{\theta-cal} + k_2 \cdot C_{\phi-cal} + k_3 \cdot C_{\theta-cal}^2 + k_4 \cdot C_{\phi-cal}^2 + \ldots. \quad (2.6)$$

A second-order fit was found to be sufficient for good predictions. $C_{\theta\text{-test}}$ and $C_{\phi\text{-test}}$ are then substituted in the polynomial expressions to calculate θ, ϕ, C_s and C_t. From these it is elementary to get the actual flow unknowns Θ, Φ (by coordinate transformation), P_s

and P_t (equations (2.1) and (2.2)). Further, using P_s and P_t, the flow velocity magnitude (Bernoulli equation, if the flow is incompressible) and/or the Mach number (isentropic relations, if the flow is compressible and T_s is known) can be readily computed.

2.4 SENSITIVITY AND UNCERTAINTY ANALYSIS

When a probe is used to measure an unknown flow field, the measured values for the velocity magnitude and angles can be different from the "true" values that would be measured by an infallible or perfectly accurate means of measurement. The magnitude of this discrepancy is a measure of the measurement accuracy of the probe. There are a number of factors/errors that can contribute to this discrepancy – errors in probe alignment, in the measurement of the probe tip pressures, in the calibration of the probe and in the data-reduction algorithm. There are two ways to determine the measurement accuracy of a multi-hole probe: (a) a theoretical approach known as uncertainty analysis or (b) an experimental approach called "calibration validation". The experimental way of estimating the probe measurement accuracy was discussed previously in the probe calibration section and will be followed here (instead of the traditional uncertainty analysis) since it provides a more realistic estimate of the errors. About 1800 test points throughout the angular range of the probe were collected at each Mach number for this purpose.

The errors in the prediction of the two flow angles (cone and roll angles) and the velocity magnitude, for these test points, at M = 0.05 are plotted in Figs. 2.12, 2.13 and 2.14 in the form of error histograms. In each plot the horizontal axis represents the error magnitude and the vertical axis represents the histogram frequency. The corresponding error data is presented in Table 2.3. 47 test points that turned out as outliers using Chauvenet's criterion[47] were removed before finding the error data. The fact that all mean errors are very close to zero indicates that there are no bias errors within the calibration or the reduction routine. The standard deviations, which are a measure of the measurement accuracy the customer should expect, are also small. The prediction errors

obtained with test data at other Mach numbers were similar (i.e., with near-zero means and comparable standard deviations). The error standard deviations obtained for all the calibration Mach numbers (for U_{mag}, Θ and Φ) is shown in Table 2.4. Hence, the accuracy of the probe can be summarized as 0.5° for Θ, 0.7° for Φ and 0.6% for the velocity magnitude, all with 95% confidence (two standard deviations).

Table 2.3. Error data for predicted variables at M = 0.05.

Flow variable	Mean (μ)	Standard deviation (σ)
Θ (deg)	-0.005	0.102
Φ (deg)	0.001	0.226
U_{mag} (%)	0.065	0.183
P_s (w.r.t q) (%)	-0.028	0.173

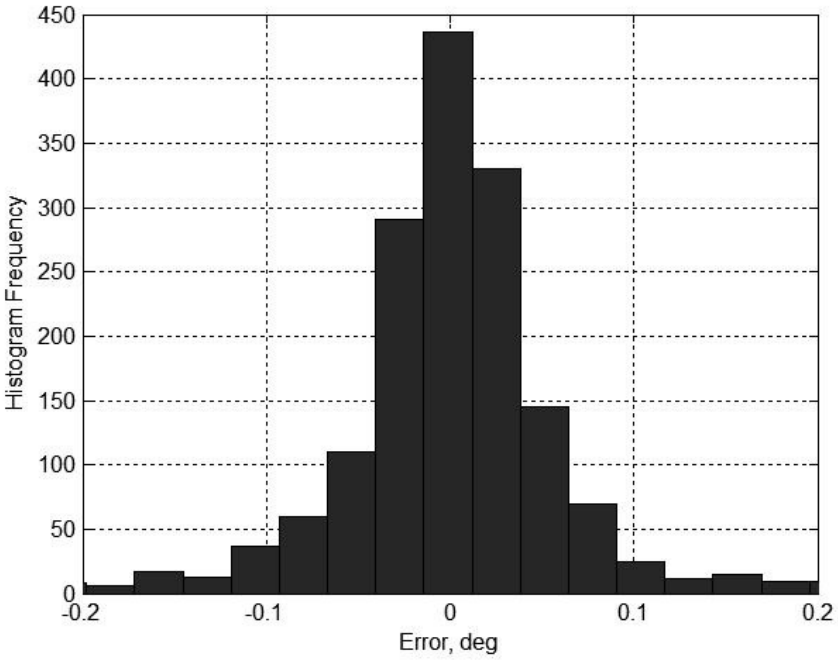

Fig. 2.12 Histogram of the error in the predicted cone angle (Θ).

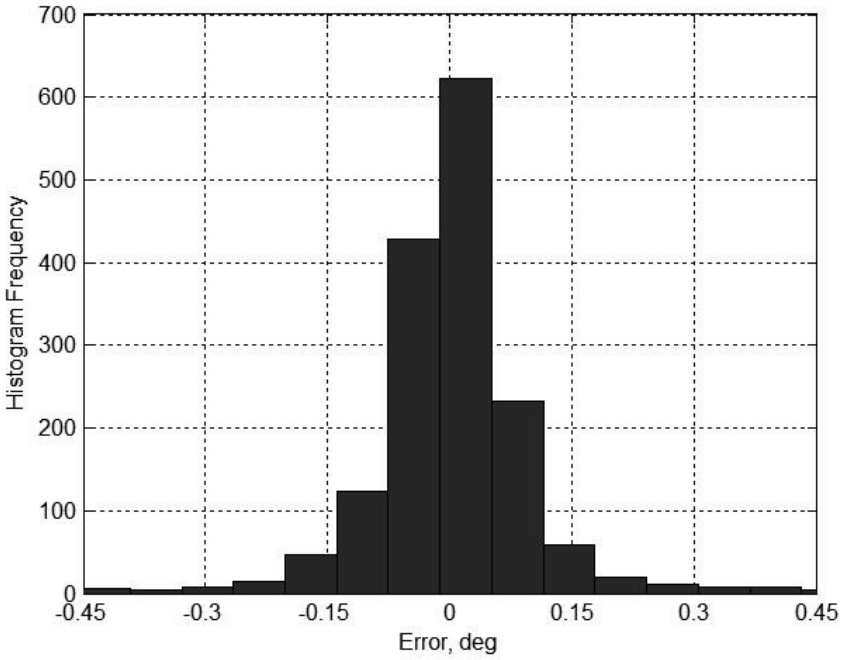

Fig. 2.13 Histogram of the error in the predicted roll angle (Φ).

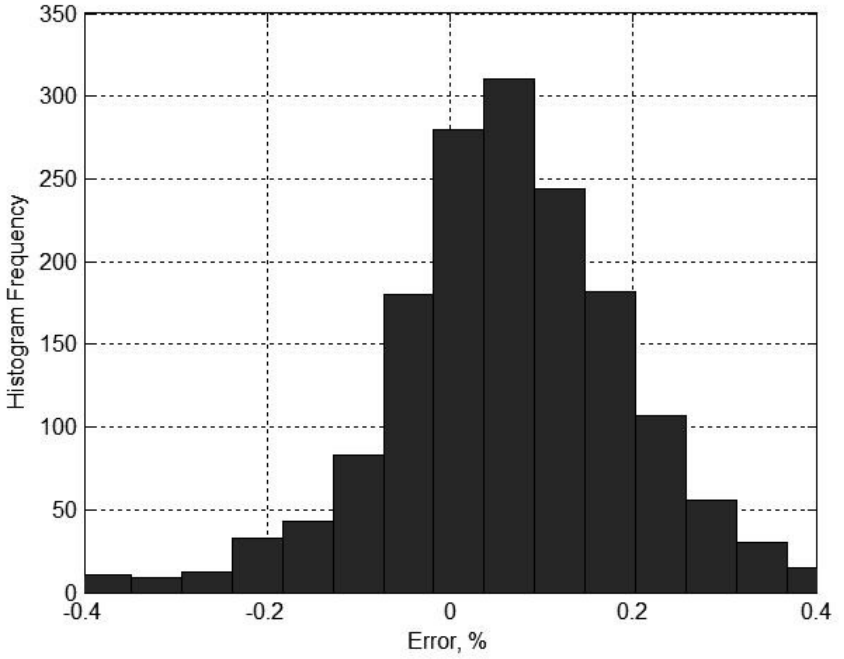

Fig. 2.14 Histogram of the percentage error in the predicted velocity magnitude (U_{mag}).

Table 2.4. Error data for predicted variables at a range of Mach numbers.

Flow variable	M = 0.05	M = 0.1	M = 0.3	M = 0.5	M = 0.6	M = 0.7
Θ (deg)	0.18	0.32	0.15	0.22	0.28	0.29
Φ (deg)	0.34	0.57	0.29	0.47	0.53	0.59
U_{mag} (%)	0.30	0.42	0.25	0.35	0.36	0.54

It is known from literature and from the authors' experience that a main source of error in flow prediction using multi-hole probes is the pressures. A sensitivity analysis was performed to see how much the variation in the calculated flow properties (outputs) of our calibration and reduction model can be attributed to the port pressures (inputs). The analysis involved the following steps (as outlined in Saltelli et al.[48]):

- identify the outputs – Θ, Φ and U_{mag} (P_s was not considered for this analysis)
- identify the inputs – p1, p2, p3, p4 (the four sector pressures of any test point)
- choose a distribution function for the selected inputs – Gaussian distribution with a chosen standard deviation
- develop an input spread with the above distribution
- calculate the unknowns using the reduction algorithm and compute their distribution
- evaluate and compare the dependence of the standard deviation of the output distribution on each input

The analysis was done with the calibration data at Mach 0.05 which corresponded to a freestream dynamic pressure of 1.24 torr. An error of 1% of the freestream dynamic pressure was introduced as the standard deviation (σ) for the pressure reading error distribution. The percentage error chosen is arbitrary and serves only to illustrate its effect on the prediction – due to p1, p2, p3, p4 separately and combined. The results are shown in Table 2.5. The output dependency on the highest three pressures (p1, p2 and

p3) overall, as seen from the root-mean-square (r.m.s) values in the last row of the table, is comparable. It should be noted that the r.m.s of the errors has no physical significance and is used here only as a means to indicate the overall error. There is a slightly higher sensitivity to p4 mainly in the predicted U_{mag}. In some flow field studies, the freestream static pressure is known, e.g., from an upstream static wall tap. In such cases the required number of pressure ports for the reduction algorithm goes down by one i.e., to three. Consequently, there is a redundancy in the availability of ports and the above analysis indicates that the flow unknowns must be calculated using p1, p2 and p3 since that combination has the least contribution to the output error.

Table 2.5. Sensitivity of predicted variables to port pressures at M = 0.05 with σ = 1% of q_{dyn}.

Flow variable	Default Error	Sensitivity to p1	Sensitivity to p2	Sensitivity to p3	Sensitivity to p4	All Combined
Θ (deg)	0.10	0.19	0.30	0.25	0.22	0.46
Φ (deg)	0.23	0.34	0.44	0.43	0.45	0.74
U_{mag} (%)	0.18	0.37	0.30	0.29	0.48	0.67
r.m.s	0.31	0.54	0.61	0.58	0.70	1.09

The error distributions in all the input pressures were combined and the prediction accuracy calculated (shown in the last column of Table 2.5). The default error (first column of Table 2.5) from the test data in the calibration facility is with an ESP sensor which commands high accuracy (typically 0.1% of its full scale span). The actual prediction accuracy when the probe is used by the end-user could be much worse depending on what sensors (not necessarily an ESP) are being used. The standard deviations in the last column of the table give us an estimate of the extent of such errors if pressure sensors with 1% (in σ) accuracy were being used – the error in each flow

variable is about three to four times the original error. Although the sensitivity analysis here has been done only for the 12-hole probe, such a dependency on pressure sensor accuracy can be expected in all multi-hole probes.

3 DESIGN, FABRICATION AND INSTRUMENTATION

3.1 PLANNING AND DESIGN

The design requirements for the Weatherprobe are based on the primary requirement that it be usable at the Mt. Washington weather observatory. This meant a design that will enable wind speed measurements in harsh environment conditions such as:

- high wind speeds up to 200mph.
- considerable vertical component of velocity (up to ±45° to the horizontal) due to the nature of the terrain
- heavy precipitation – rain and snow storms
- icing conditions with temperatures as low as -40°C in winter

The 12-hole probe design provided itself as the foundation for the Weatherprobe's design. The 12-hole probe had a 3/8 in. spherical head and pressure tubing running from the ports at the sphere-surface all the way through the sting and the probe body to external pressure sensors. For the Weatherprobe, there were design limitations on the length of tubing (for frequency response reasons) and it was decided to mount the sensors at or near the pressure-port. In other words, it was decided to minimize the pressure transmission paths from the probe tip to the transducer diaphragm and hence minimize the associated attenuation and phase lag in the measured pressure. Moreover, some space inside the sphere was needed to install heating elements and all the associated wiring. All this dictated a much larger spherical head and hence a 6 in. hollow sphere was chosen for the prototype. It was large enough to accommodate all the components but small enough to keep the heating requirements low. (Note that bigger the probe, the higher the heating requirement).

The 12-hole design has all the ports uniformly distributed throughout the sphere. For the Weatherprobe, such an arrangement would cause some ports to be exposed to direct influx of rain/snow in the event of precipitation. Hence all the ports had to be arranged

close to the "equator", where the equatorial plane is parallel to the azimuthal plane (Fig. 3.1a). The probe coordinate system for the Weatherprobe is the same as that of the 12-hole probe (reproduced here in Fig. 3.1b).

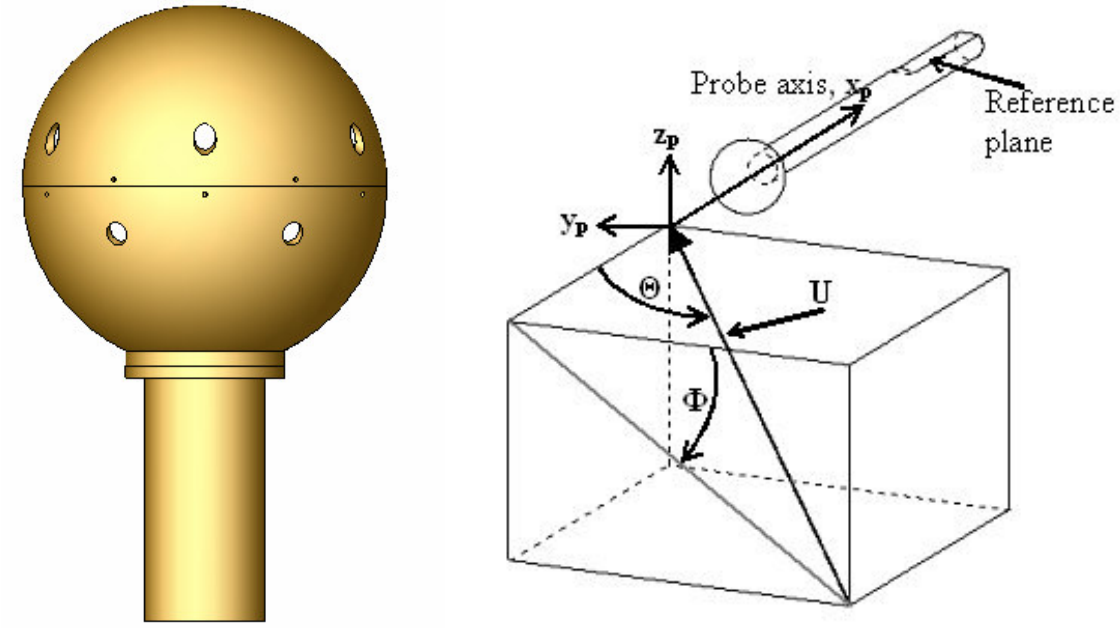

Fig. 3.1 Weatherprobe: a) Solid model, b) Coordinate system.

At the outset, three aspects of the design were decided – a) the number of ports, b) the type of distribution of the ports and c) the azimuthal angle at which the ports should be arranged. The main requirement for the port arrangement is that the ports should be arranged close to the equator in order to avoid clogging due to precipitation. Ports arranged at +/-30° or below are expected to satisfy this condition. Two patterns of arrangement were considered – staggered and aligned. The staggered arrangement refers to that in Fig. 3.1a. In the aligned arrangement, ports above and below the equator will be in the same vertical plane. The number of ports was decided to be either 10 or 12, an even number due to symmetry considerations. Different permutations and combinations of the three parameters were tested and the maximum possible range of resolvable angle (from the equator) calculated for each design. It is a design requirement that this angle,

which is the maximum angle of the wind velocity vector from the equator, be at least 45°.

The probe's angular range is the maximum angle at which the following two conditions are always satisfied: 1) there are at least four ports within 81° (well within the laminar sphere separation angle of 84°) and 2) at least one of these four is on the opposite side of the equator with respect to the stagnation point. The second condition requires that if the stagnation point is on the top hemisphere, at least one port on the bottom hemisphere be within 81° from the stagnation point. This condition, although not essential, was found to be good for the reduction algorithm in order to get better prediction accuracies.

To study different possible configurations, pressure data over a sphere was generated (using equation (1.2)) for some preliminary tests. The central angle (Θ^*) between any two points (Θ_1, Φ_1) and (Θ_2, Φ_2) on the surface of the probe can be derived from basic geometry as the equation:

$$\Theta^* = 2 \sin^{-1}\left(\left|\sqrt{\frac{\left(1-\cos(\Theta_1)\cos(\Theta_2)-\sin(\Theta_1)\sin(\Theta_2)\cos(\Phi_1-\Phi_2)\right)}{2}}\right|\right) \quad (3.1)$$

Ten ports with five on each side of the equator, or twelve ports with six on each side were considered. As mentioned earlier, the ports on each side could either be arranged vertically above/below each other or in a staggered formation (as in the final formation shown in Fig. 3.1a). For the prototype, it was decided to choose a staggered 12-port configuration because it consistently gave better angular ranges (when tested with theoretical data), thus narrowing down the list of possible configurations.

The next check was to look at the accuracy of prediction (throughout the entire angular range of the probe) for each configuration (using theoretical data). To this end, calibration and reduction algorithms that were developed for all multi-hole probes (Ramakrishnan and Rediniotis[17]) were tailored to meet the needs of the various port-arrangements being tested. Based on the best prediction accuracies, it was decided to

build a prototype with a staggered arrangement of six ports on each side of the equator at an angle of ±15° from the equatorial plane, as shown in Fig. 3.1a. The coordinate locations of the ports in this final design configuration are given in Table 3.1. The prediction accuracy for this configuration using theoretical data was good as is seen from the error histograms shown in Figs. 3.2, 3.3 and 3.4. This error data also served as a general uncertainty analysis during the planning stage by assuming clean (theoretical) calibration data. Errors of 0.3° in the angles and 0.35 % in the velocity magnitude, all with 95% confidence, were obtained. This is the bare minimum errors expected from the probe. Bias (or mean error) was nearly zero for the flow angles and very small (0.1%) for the U_{mag}, as seen in the histograms.

Table 3.1. Port coordinate locations in the Weatherprobe design.

Port#	Θ (deg)	Φ (deg)
1	75.0	0.0
2	75.0	60.0
3	75.0	120.0
4	75.0	180.0
5	75.0	240.0
6	75.0	300.0
7	105.0	30.0
8	105.0	90.0
9	105.0	150.0
10	105.0	210.0
11	105.0	270.0
12	105.0	330.0

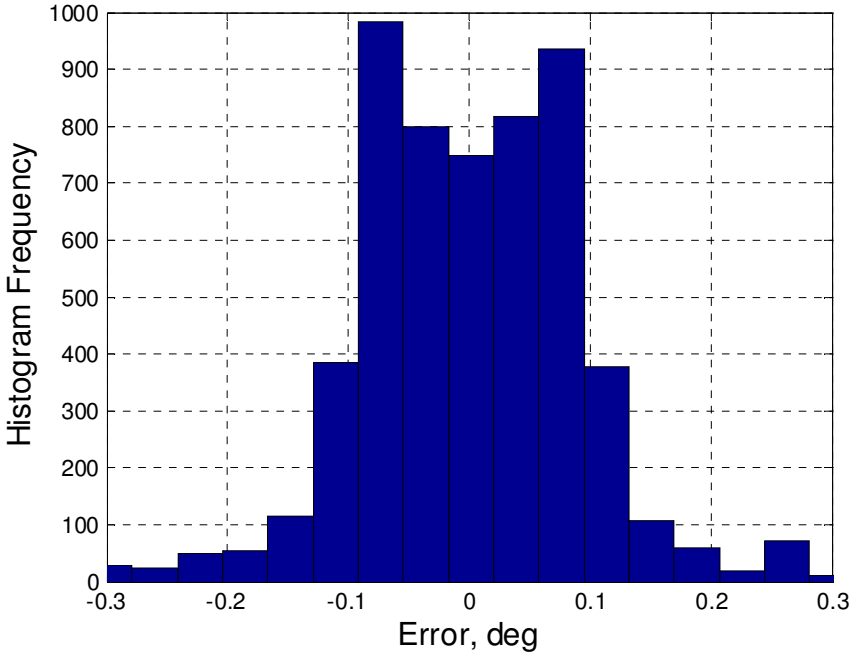

Fig. 3.2 Histogram of the error in the predicted cone angle (Θ) with theoretical data.

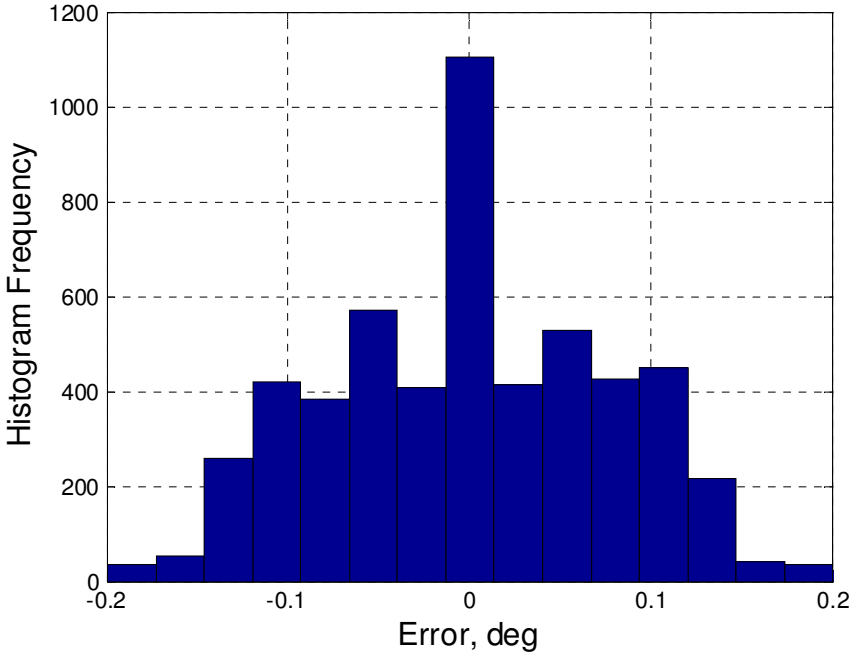

Fig. 3.3 Histogram of the error in the predicted roll angle (Φ) with theoretical data.

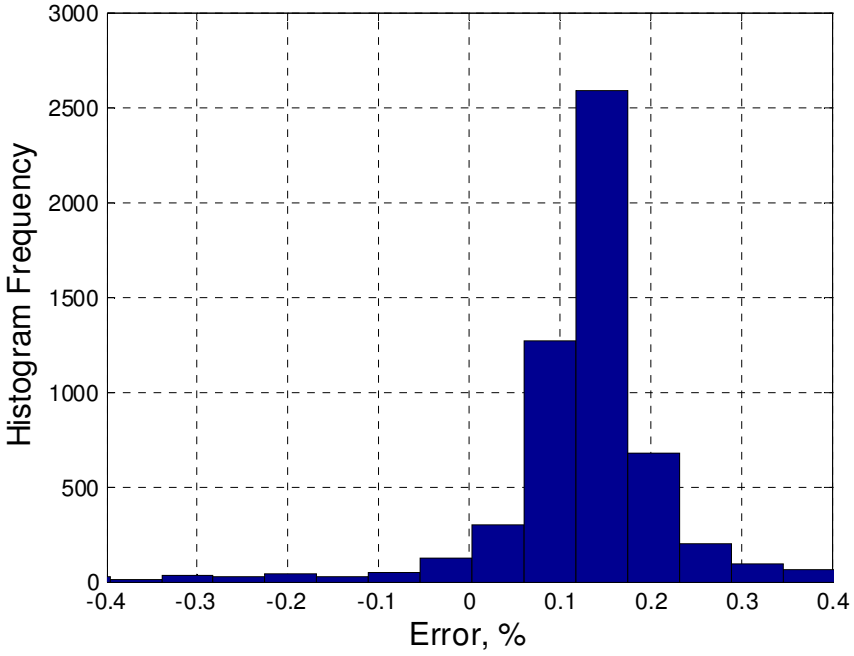

Fig. 3.4 Histogram of the percentage error in the predicted velocity magnitude (U_{mag}) with theoretical data.

3.2 MODIFYING THE REDUCTION ALGORITHM

The reduction algorithm had to be modified to suit the new port arrangement of the Weatherprobe. Based on the port locations (Table 3.1), the Weatherprobe was divided into sectors of four ports each, based on the highest pressures. Let us assume, without loss of any generality that, for some stagnation point (Θ_0, Φ_0), port A had the highest pressure in Fig. 3.5. Let us also consider only stagnation points that lay to the right of port A (dotted line). With port A being the highest, three sectors were defined for any stagnation point in this region, namely, A-B-Z, A-Z-B and A-Z-Y, where the ports' sequence in each sector have been specified in the decreasing order of the magnitude of the pressures they measure. The fourth port in the above three sectors was automatically chosen as Y, Y and B, respectively. On the symmetric side to the left of the dotted line, are three more similar sectors for stagnation points with port A having the highest

pressure. Hence, the region near port A, has been divided into six sectors, adding up to a sum total of 72 (12 x 6) sectors for the entire probe. The above sectorization scheme was found to work best after exhaustive trials with different schemes and by looking at the nature of the calibration data.

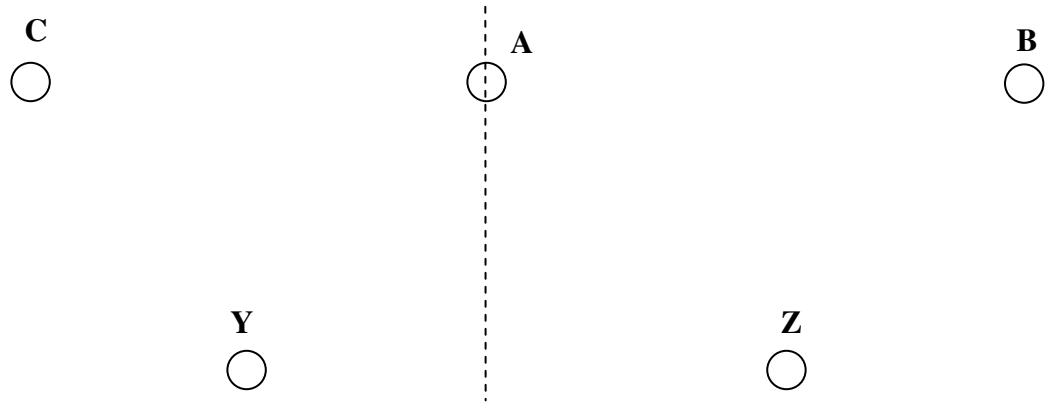

Fig. 3.5 Schematic of a generic port arrangement.

Non-dimensional sector-coefficients were then found based on raw pressure (calibration) data for each of the 72 sectors. Then, the non-dimensional angle-coefficients were calculated for each calibration point. This completed the preprocessing. The reduction algorithm followed the same technique as described for the 12-hole probe in section 2 or Ramakrishnan and Rediniotis[17].

3.3 FABRICATION

The probe head consisted of two hemispherical halves (commercially available) made of aluminum joined at the equator (Fig. 3.6). An aluminum ring of 0.25 in. thickness served to join the two halves with the aid of twelve 2-56 flat-head screws (3/8 in. length) around the equator. At the bottom of the lower hemisphere a 2in. hole was drilled to make way for the wiring through the cylindrical sting. The sting, also made of aluminum, was of 2 in. outer diameter, 1.6 in. inner diameter and 4 in. length. A small ring was welded to the lower hemisphere and the sting was then attached to this ring with four screws. A small

"flat" of 1 in. x 0.25 in. was machined on the outer surface of the lower end of the sting. This flat served as a reference plane for defining the probe's coordinate system. Holes of 3/8 in. diameter were precision drilled at the design port locations. Stainless steel tubes of 3/8 in. outer diameter and 1 in. lengths were attached at the drilled port locations using epoxy. The side of the tube that was near the surface was shaped with a belt sander to make it conform to the spherical surface and thus avoid any bumps. The inner diameter of these tubes was 0.3 in. which consequently was the port diameter of the probe. These tubes were attached (extending into the interior) at an angle of 30° to the horizontal (as shown in the probe's cross-sectional view in Fig. 3.7) to aid the draining of any water that might enter the ports.

An exploded view in SolidWorks showing all the parts is shown in Fig. 3.6a. A picture of the fabricated prototype probe is shown in Figure 3.6b.

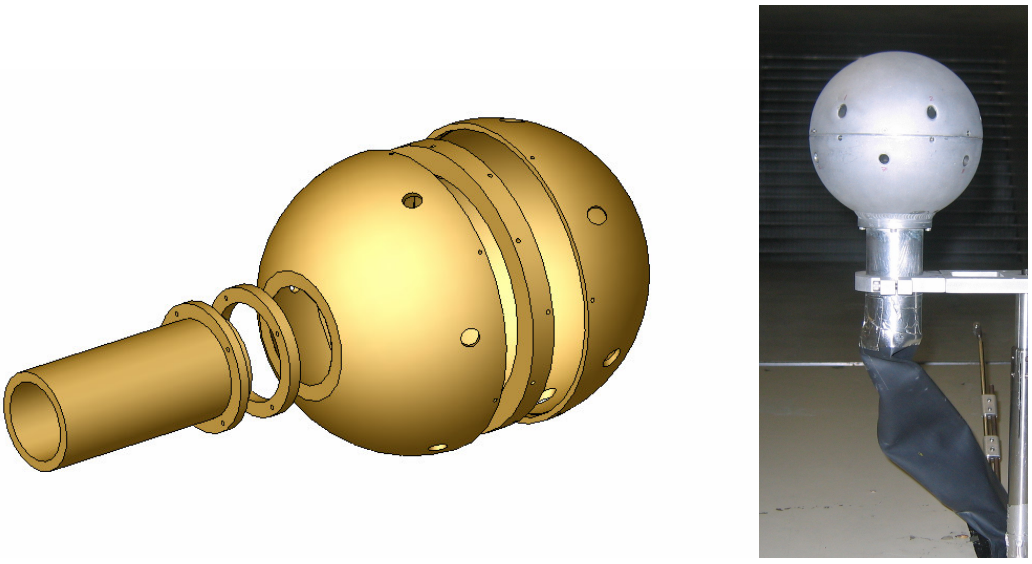

Fig. 3.6 Weatherprobe: a) exploded solid-model view, b) fully-assembled probe.

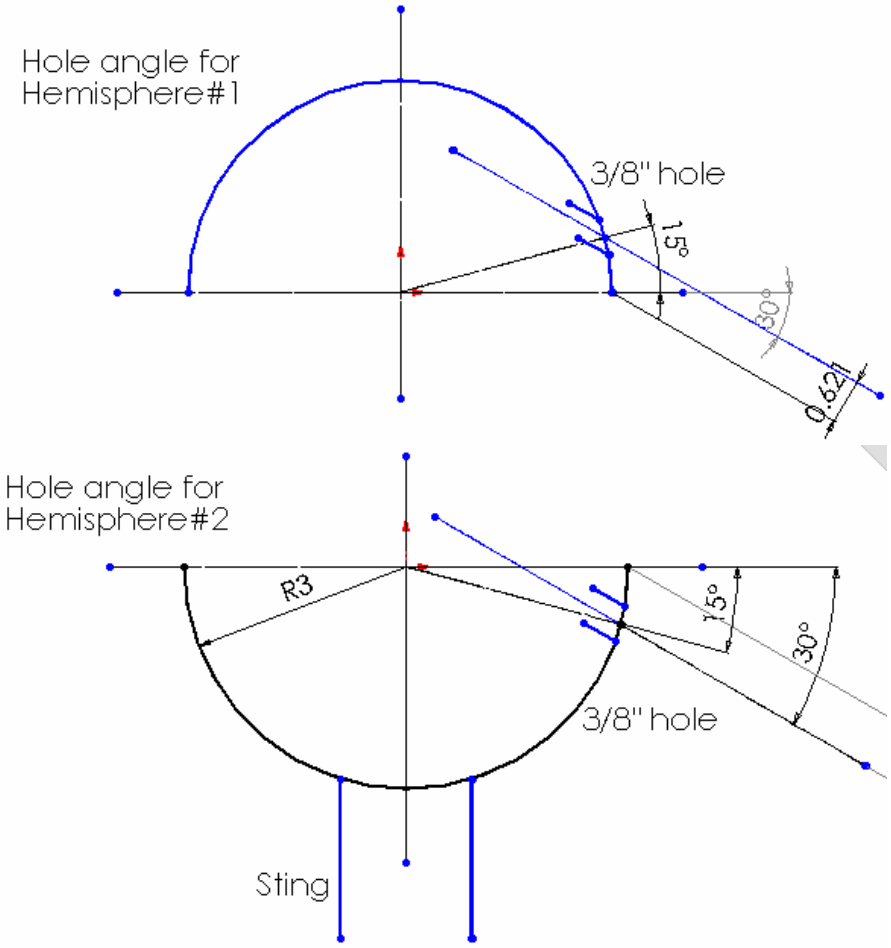

Fig. 3.7 Cross-section of the Weatherprobe depicting the inclined ports.

Complete machine drawings showing the dimensioning for all the parts are given in Appendix A.

3.4 INSTRUMENTATION: PRESSURE SENSORS AND DATA ACQUISITION

There is a wide variety of commercially available pressure sensors with varying levels of accuracy, size, pressure range and price range. The task of finding the one that exactly fits our needs is not trivial. With the conditions at Mt. Washington observatory in mind,

the following strict requirements were imposed for choosing the pressure sensors for the Weatherprobe.

- range 1 psi (or 50 mm Hg) (gage) (based on maximum wind speed)
- small size – so as to fit within the 6 in. diameter probe head
- amplified output – so that long signal lines do not attenuate the signal and there is minimal noise pick up
- low price – less than $50
- workable in humid conditions
- at least a 200Hz frequency response – to capture velocity fluctuations
- operating temperature -20°F to 120°F (-30°C to 50°C) – to maintain functionality in winter
- temperature compensation – at least between 0°C to 50°C
- board mountable – for internal circuitry if desired
- robust

It turned out that amplified output and small size were in most cases mutually exclusive unless price was not a factor. Only a handful of sensors in the market were anywhere close to all our requirements, of which many were tried and tested. Honeywell's 40PC series silicon piezo-resistive sensor with ±50 mm Hg range (Fig. 3.8a) was found to fit most of the requirements and was chosen for the prototype. It had a manufacture-specified overall accuracy (including hysteresis and repeatability) of 1% F.S.S (full-scale span).

For prototype development of the probe, it was intended to perform initial field tests at a low-land weather station in Texas and hence a lower range pressure sensor was needed to effectively measure wind speeds up to typically only 10-20m/s. Hence, a ±5 in. H_2O ASDXL series sensor (also from Honeywell) (Fig. 3.8b) was also tested and integrated (later) into the Weatherprobe system.

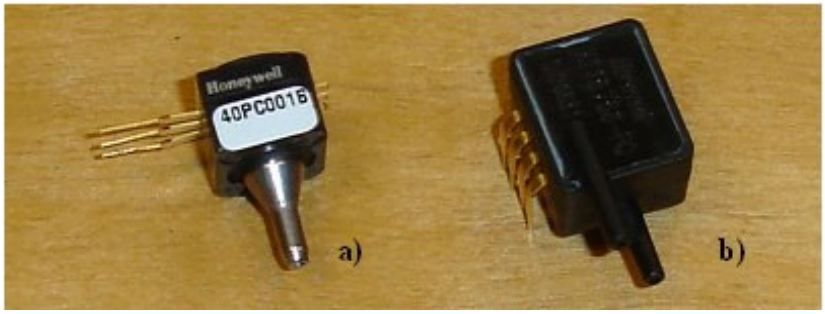

Fig. 3.8 Pressure sensors used in the Weatherprobe: a) 40PC series (±50 mmHg), b) ASDXL series (±5 in. H_2O) (from Honeywell Intl., Inc.).

Each sensor was calibrated over its full range. TSI's Air Velocity Calibrator (model 1125) was used to set the sensor pressure at different values. The calibration pressure was teed off and measured with an Edwards Barocel (model 590DF) – a high accuracy instrument that has a manufacture-specified accuracy of 0.05% F.S.S and a range of 100 torr. The sensors were warmed for at least twelve hours before calibration. The voltage output from the sensor (which ranges from 2.5V to 4.5V for positive pressures) was measured by the probe's data acquisition (Daq) system (described later). Rectangular pneumatic connectors with 14 pins (12 pins for each of the sensors, 1 pin for input calibration pressure and 1 pin for reference pressure) from Scanivalve Corp. enabled simultaneous calibration of all twelve sensors. Good linear calibration curves were obtained – a sample (for one sensor of the ASDXL series) of which is shown in Fig. 3.9.

As seen in Fig. 3.9, the sensor calibration is very linear with a slope of 2.358 torr/volt. Similar slopes were obtained for all the twelve sensors. The calibration was repeated many times for all the sensors and good repeatability was observed. The voltage reading at zero pressure, known as zero offset, was about 2.5 volts in each case and fairly stable as long as the ambient temperature was constant. The above calibration was performed at 22°C inside the lab. In order to test the effects of ambient temperature on the slope and the zero voltage, they were also calibrated outdoors at 30°C. A comparison plot showing both calibrations for a sample sensor is shown in Fig. 3.10.

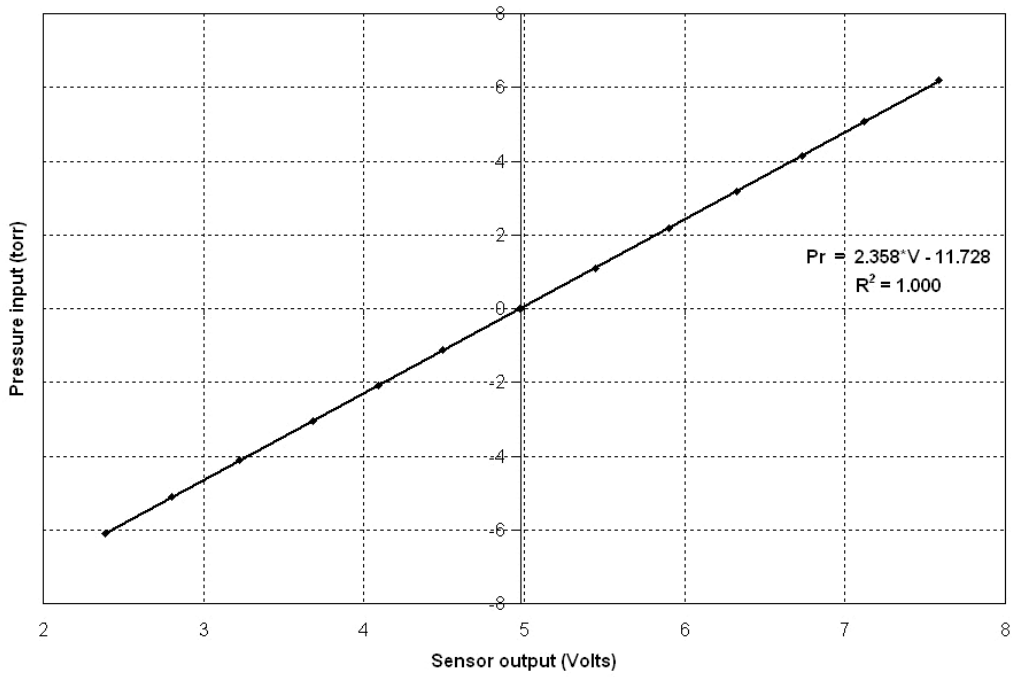

Fig. 3.9 Typical ASDXL sensor calibration slope – very linear.

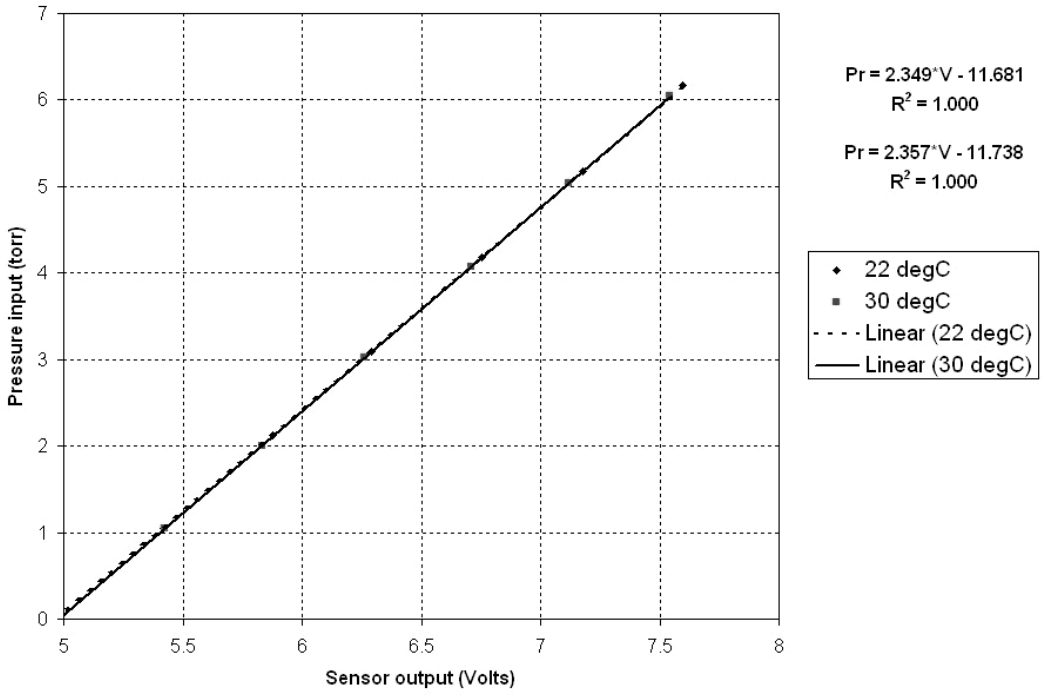

Fig. 3.10 Temperature dependence of the ASDXL sensor calibration – very small change in slope.

The calibration slope of the sensor outdoors was 1.004 times the indoor slope, which bears to be noted although it is a small change. This ratio was consistently observed in all the sensors. The zero offset voltage also drifted (as expected) due to the temperature change by about 5-10mV for all sensors. Hence, it was decided to use the outdoor calibration for field tests (in September) due to higher day temperatures. In future versions of the Weatherprobe system it will be beneficial to calibrate the sensors over a range of temperatures and use, for every measurement point, the appropriate calibration based on an ambient temperature reading.

There is a multitude of data acquisition (or Daq) boards in the market. Except for the ruggedness requirement (large temperature range) any of the commercially available brands would have fit the bill. The Daq board for the Weatherprobe needed the following attributes:

- high throughput – at least 100kHz for high frequency acquisition
- 16-bit A/D conversion – for high accuracy
- 8-K FIFO buffer – for temporary storage of the converted pressure data
- ±10 volt analog input range – for the sensors' output voltage up to 4.5V
- programmable binary gains – so that the measured sensor voltage can be amplified (thus reducing A/D error) if needed.

Apart from the above requirements for the board, the system itself needed to be self-sustaining so that it can be installed in remote locations. In other words, the Daq system required a sizeable storage for acquired data and a processor for real time measurements. Further, the entire system had to be rugged enough to handle Mt. Washington's conditions. RTD Embedded Technology's IDAN system (Fig. 3.11) proved to fit the bill. It was a PC-104 based system with a 1GHz processor, 512MB RAM and a 20GB hard-drive. It also had an Ethernet port through which data transfer could be easily handled. The system was ruggedized to work well over a temperature range of -20°C to 85°C and was splash proof. It also had fairly small physical dimensions of

approximately 6 in. x 6 in. x 6 in. thus conserving space. The system can thus be installed in harsh remote locations and provide real-time wind data that can be accessed remotely over the Ethernet.

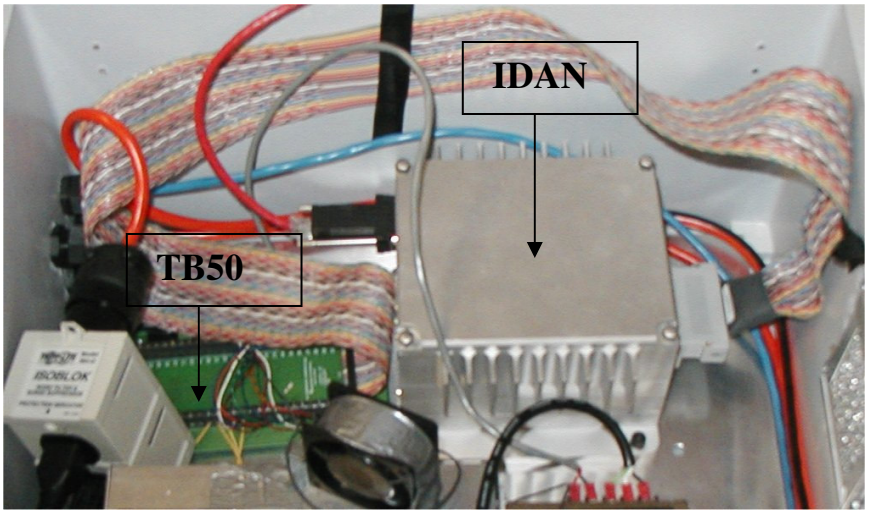

Fig. 3.11 IDAN data-acquisition system from RTD Embedded Technologies, Inc.

All the pressure sensors were interfaced with the IDAN system's Daq board through a TB50 (Fig. 3.11) screw terminal board from the same company.

A code in *Visual C++* was written to handle the Daq board settings and read the data off of the A/D converter at specified sampling rates. The code was set up to process the acquired voltage data (using the sensor calibration slopes) and obtain averaged pressure data at 1Hz (i.e., multiple samples averaged over 1 second). Although 100Hz data was the ultimate goal for the system, 1Hz was deemed sufficient for the prototype. A DLL written separately in *Delphi* performed the data-reduction. The DLL accepted the twelve pressures (from the VC++ code) as the input and generated flow data (three velocity components and static pressure). The DLL was fast enough to plot wind data in real time on the VC++ code's GUI (graphical user interface). The data was saved in the IDAN system's 20GB storage for future access. A picture of the GUI showing the input parameters and the output wind speed plot is shown in Fig. 3.12.

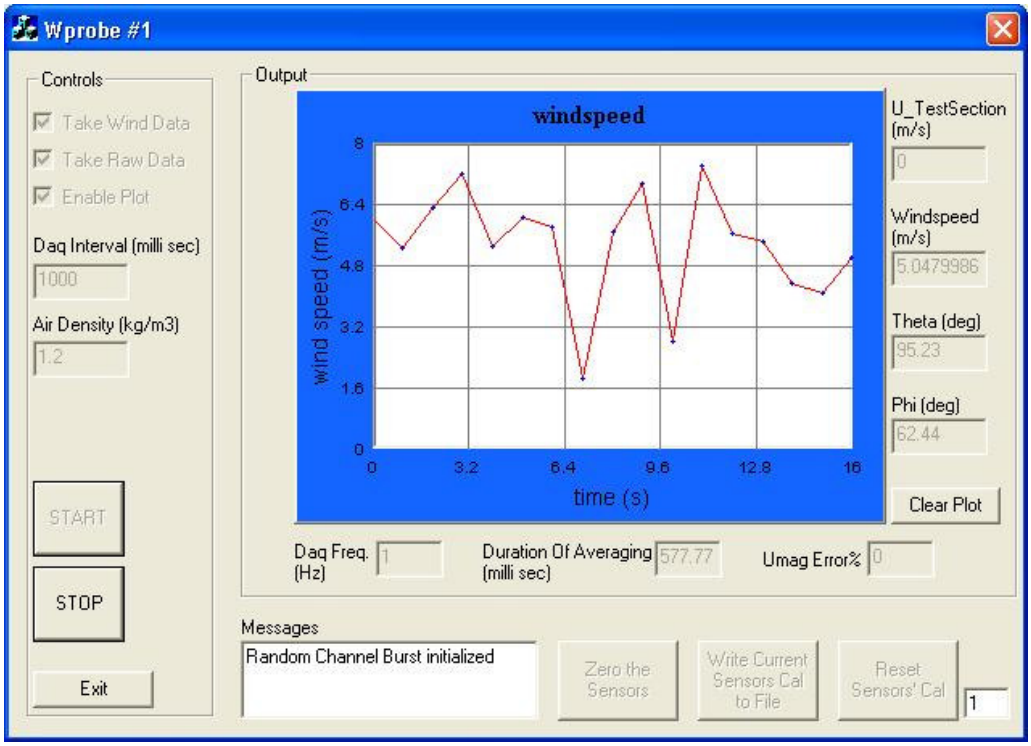

Fig. 3.12 Data acquisition GUI.

3.5 INSTRUMENTATION: HEATING AND TEMPERATURE CONTROL

Power requirement calculations

It was decided that the spherical head and the cylindrical sting would be heated internally for application of the Weatherprobe in icing conditions. Preliminary estimates to calculate the amount of heating power required, based on forced convection, were done by a combination of theoretical and experimental analysis. The following parameters were available for analysis:

- diameter of the probe = 6 inches
- maximum wind speed = 200 mph = 105m/s
- maximum difference between the desired probe surface temperature and the ambient temperature = 40°C
- density and viscosity of air

For a temperature difference of dT for a surface area A, the forced convection heat loss is calculated as

$$\dot{Q} = h \cdot A \cdot dT \tag{3.2}$$

where, h is the convective heat transfer coefficient calculated from

$$h = \frac{Nu \cdot k}{D} \tag{3.3}$$

where, k is the conductive heat transfer coefficient, (k = 0.0258 for Aluminum) and D is the reference dimension (the diameter for spheres and cylinders).

The Nusselt number (Nu) is calculated from empirical relations. For forced convection over a sphere, Nu is given as

$$Nu = 2 + \left(0.4\,Re^{1/2} + 0.06\,Re^{2/3}\right) Pr^{2/5} \left(\frac{\mu}{\mu_s}\right)^{1/4} \tag{3.4}$$

and for the cylinder,

$$Nu = \left(0.4\,Re^{1/2} + 0.06\,Re^{2/3}\right) Pr^{2/5} \left(\frac{\mu}{\mu_s}\right)^{1/4} \tag{3.5}$$

The net heat required is the sum total of that required for the spherical head and the cylindrical sting. The ambient temperature (hence dT), air density and air viscosity vary depending on location, season and altitude. Many different scenarios were tested. For the extreme conditions of Mt. Washington in winter, with the probe surface maintained at 5°C, the heating requirement was found to be approximately 600 watts.

In order to verify these calculations, a smaller model of the Weatherprobe was tested with the heating elements mounted internally. At ambient temperatures of about 20°C in the lab, the model probe was heated and maintained at 40°C. Air at a fairly constant speed was impinged on the probe from an air blower. The heat used up was compared to

that obtained from theoretical calculations. Assumptions were made for heat loss into the internal volume of the probe and radiative heat losses. 80% of the heat was accounted for. In other words, the experimental test required about 20% more power than was theoretically calculated for the said conditions. For preliminary tests, this result was acceptable and a more rigorous testing with more accurate flow speed and temperature measurements in a clean wind tunnel was abandoned.

Heating elements

Due to limited space within the probe and due to the curved nature of the probe surface, a flexible thin heating element was ideal. Many different heaters were tried and tested. Finally, silicone rubber heating elements (from Omega Engineering) with power density of 10 watts per square inch were chosen. The SRFG-series heating elements were fiberglass-insulated and were only about 0.1 in. thick. The heating elements work on 115Vac off-the-wall power supply. Each hemisphere had six elements (each 3in. long, 1 in. wide) symmetrically arranged on the inner wall. Each element provided a heating power of 30 watts. The sting had three heating elements (each 4in. long, 1 in. wide) along its length. They were affixed using thermally conductive paste (also from Omega Engineering). The total power available was 480 watts. Although this fell short of the target, it was deemed sufficient for the prototype. 480 watts is more than sufficient to keep the probe ice-free in hurricane winds (50m/s) in as low as -20°C ambient conditions. A picture of the heating elements mounted on the inner surface of the hemispheres is shown in Fig. 3.13.

Temperature control

A T-type thermocouple was installed within the sphere to measure the inside air temperature. This temperature is maintained at a desired setting using Omega's CNi8 series (model DH54-EI) temperature controller. The controller accepts a single thermocouple input and controls a solid-state relay (SSR) that works as an on-off switch depending on whether the thermocouple is reading above or below the set temperature.

The controller also provides a digital readout of the temperature. The heating elements are connected in series with the SSR. The circuit is depicted in the block diagram in Fig. 3.14. A picture of the controller and the SSR are shown in Figs. 3.15 and 3.16, respectively.

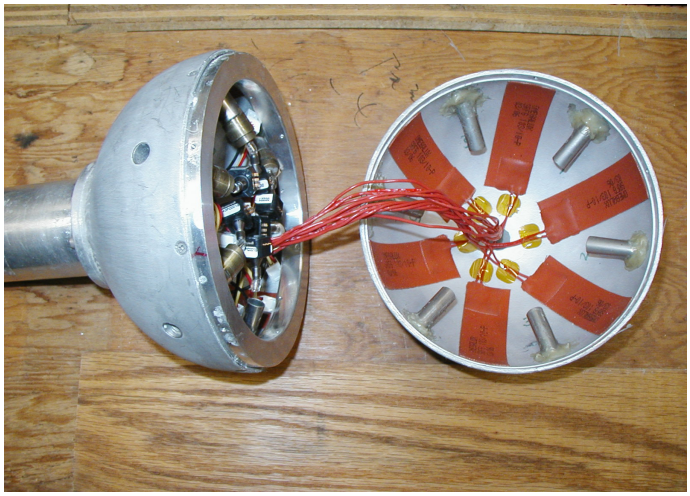

Fig. 3.13 Flexible silicone rubber heating elements mounted on the inside surface of the probe – 6 on each hemisphere.

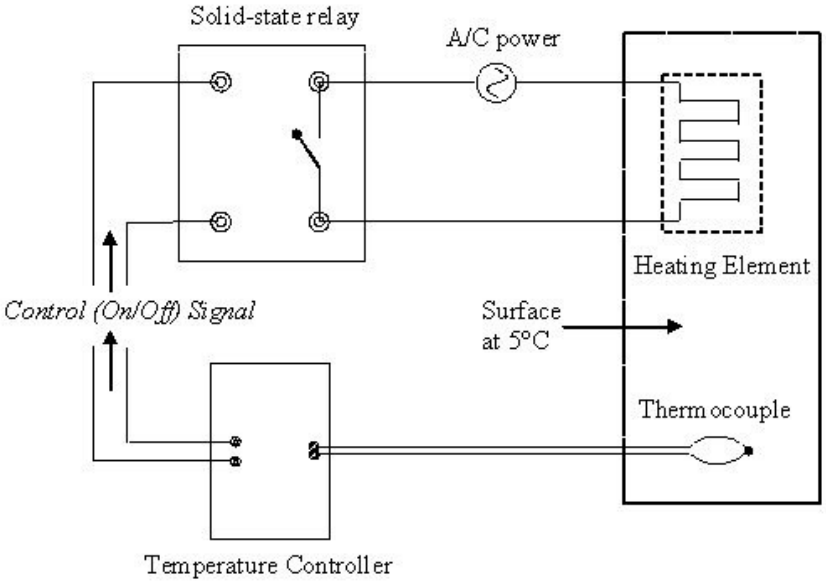

Fig. 3.14 Schematic of the temperature-control feedback circuit.

Fig. 3.15 Picture of temperature controller unit (CNi8 series, from Omega Engineering, Inc.).

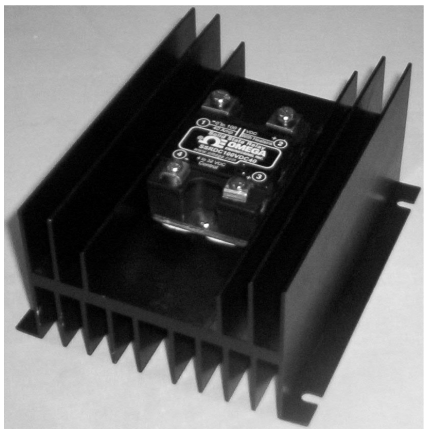

Fig. 3.16 Picture of solid-state relay with heat-sink (SSRL series, from Omega Engineering, Inc.).

3.6 INSTRUMENTATION: MISCELLANEOUS

Power supply

The power required by the Daq system was 50 watts at 8-32 VDC. Due to high temperatures likely to be reached during field testing, a robust power supply was chosen with a (distributor-supplied) power derating (as a function of temperature) as shown in Fig. 3.17. At ambient temperatures as high as 60°C, the graph shows the power supply being able to output at least 70% of its rated output. A 75W power-supply (Model RS75-24) with a 24V DC output from Astrodyne Corporation (Fig. 3.18) fitted our requirements. The power supply had an operating temperature of -25 to 70°C which was

ideal. The supply was also used to power a small cooling fan inside the enclosure which drew very little current.

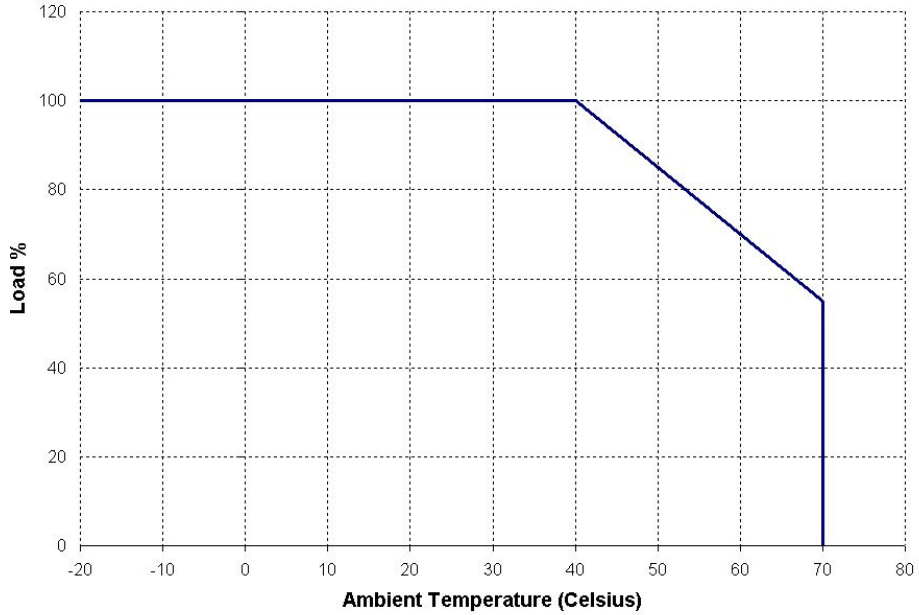

Fig. 3.17 Power derating (with ambient temperature) curve of the RS75-24 power supply (Courtesy: Astrodyne Corporation).

Fig. 3.18 Picture of the RS75-24 power supply – 75W max rating, 120VAC input, 24V output.

Hydrophobic coating

If any water (due to precipitation) on the surface of the probe sticks and/or beads up, it could affect the measurement accuracy of the probe. Hence, a coating from Luna Innovations, which was expected to stave off water from beading up on the surface, was tried on the aluminum outer surfaces. This hydrophobic coating was found to be effective to some extent. But the thickness and unevenness of the coating was not small enough to ignore its effects on the probe's performance and the coating was removed. Although, the prototype Weatherprobe is being tested without any coating, the above is mentioned here in order to stress the need for a good hydrophobic coating on the final product after prototype testing is completed. A coating by Advanced Materials Components Express (AMCX-18) was tested on smaller samples and seemed to work well and is proposed for the final version of the probe.

Enclosure

All the associated hardware was contained within a weather-proof fiberglass enclosure (from AD Products Co.) of dimensions 18in x 16in x 8in. The enclosure housed the IDAN Daq system, terminal board, power supply, solid-state relay, temperature controller and all associated wiring. A picture of the enclosure with all its components is seen in Fig. 3.19. All the instruments within are hooked up to the probe through signal cables running through the side. The enclosure, when closed, was completely sealed for rugged outdoor operation.

Since the enclosure would be set up outdoors, the heat dissipated by the instruments and solar heat gain, both of which could heat up the instruments beyond their operating temperatures, were also studied. The former was calculated by running the instruments in full swing and measuring the air temperature within the box (thermocouples near the top wall). The thermocouple readings, placed at three different locations, were averaged out. This temperature was found to be about 8°C above the ambient temperature outside the box after steady state was achieved (which took about 8 hours). Then, using basic

heat transfer equations the heat dissipation was found to be about 50 watts. The solar heat input into the box was also estimated by an approximate method which uses the surface area and type (color) of the enclosure. A more rigorous approach would be to measure temperatures at a lot more locations and solve the system using computational techniques, but was not adopted here since only an approximate estimate was needed to ensure that the (enclosure) internal temperature was well within the operating temperatures of all the instruments. Further, during field tests, the enclosure was provided with basic protection from direct solar radiation by deploying white-painted wooden panels above it.

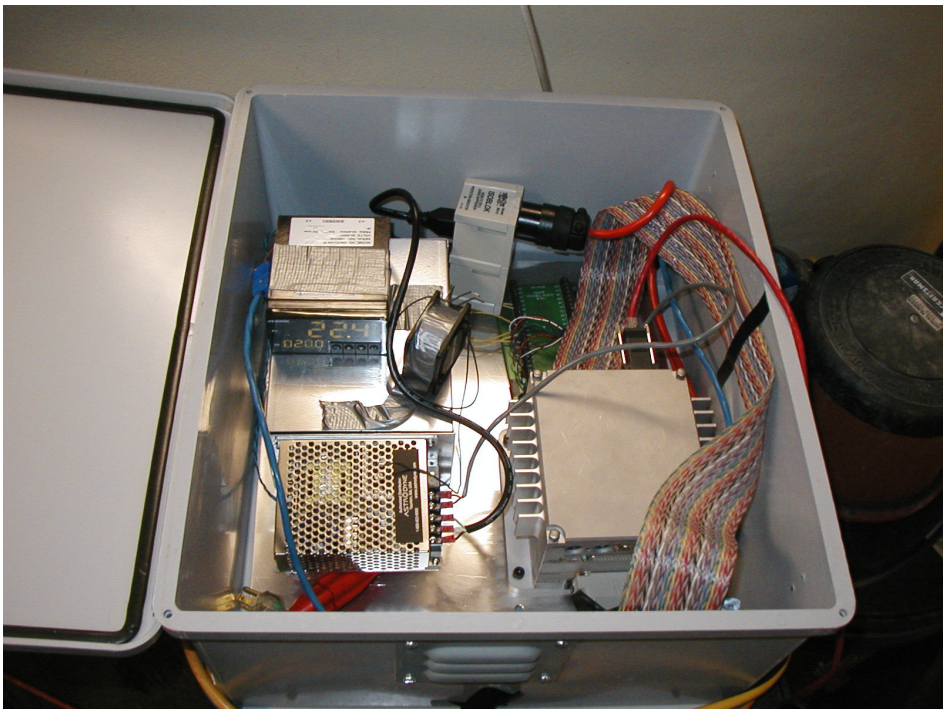

Fig. 3.19 Fiberglass enclosure with all components assembled.

4 CALIBRATION, WIND-TUNNEL TESTS AND FIELD TESTS

4.1 CALIBRATION AND PREPROCESSING

Any multi-hole probe that is being used in the non-nulling mode requires calibration before it can be used for taking measurements. A calibration provides a map between the port pressures and the flow field unknowns. This map is defined in terms of sector-specific non-dimensional coefficients that relate the four unknowns – Θ, Φ, P_s, P_t – to the port pressures. The process involves placing the probe in a uniform, perfectly known flow field (known in terms of velocity magnitude and direction, density, temperature, static pressure), at many different orientations with respect to the known velocity vector, and recording, for each such orientation, the twelve port pressures and the freestream dynamic pressure. The complete procedure is described in detail for the 12-hole omni-directional probe in section 2.

The calibration was performed at the Virginia Tech University Aerospace Engineering Department's 36-inch-diameter circular cross-section wind-tunnel. It is an open-throat return type tunnel, with the test section shown in Fig. 4.1. During calibration, none of the instrumentation earmarked for the Weatherprobe (previous section) were used. Instead, the calibration facility used its own set of pressure sensors and data acquisition (both hardware and software). Instead of the Honeywell piezo-resistive sensors chosen earlier for the prototype, an Electronic Pressure Scanner (ESP) from PSI Inc., which commands an accuracy of 0.1% of its full scale span (FSS), was used. This was to minimize calibration errors. The twelve pressure ports were connected via Tygon® tubing to a ±10 in. H_2O ESP. The calibration system had its own data acquisition board which obtained the pressure data from the ESP. The entire calibration process (motors and data acquisition) was automated using software written for the purpose.

Fig. 4.1 Virginia Tech low-speed wind-tunnel – Circular (36-in.) test section.

The probe was fixed to an L-shaped support frame with the aid of a shaft (see Fig. 4.2). The shaft length was adjusted such that the probe head was aligned vertically above the cone (Θ) motor. This ensured that the probe head stays at the same point in space throughout the calibration thus minimizing calibration errors that could be introduced if there are high spatial velocity gradients (or non-uniform velocity distribution) in the test section. The entire frame was then positioned such that the probe head was approximately centered with respect to the circular flow cross-section. The roll (Φ) motor is installed below the axis (shaft) of the probe. The cone-motor was a NEMA 34 frame stepper motor with a step-size of 1.8°/step. A tabletop traverse with 72:1 gear ratio was used to equip the cone-motor to have a minimum step-size of 0.025° and increased torque (although the probe was not calibrated at this resolution). The roll-motor was a NEMA 23 frame stepper motor with a step-size of 1.8° on a 4.8:1 ratio belt drive for the roll motion thus giving a minimum step-size of 0.375°. The L-frame (or arm) was made from a composite fence post and some metal pieces from the hardware store. Smooth rolling of the probe shaft was achieved by roller-bearings inside a machined sheath.

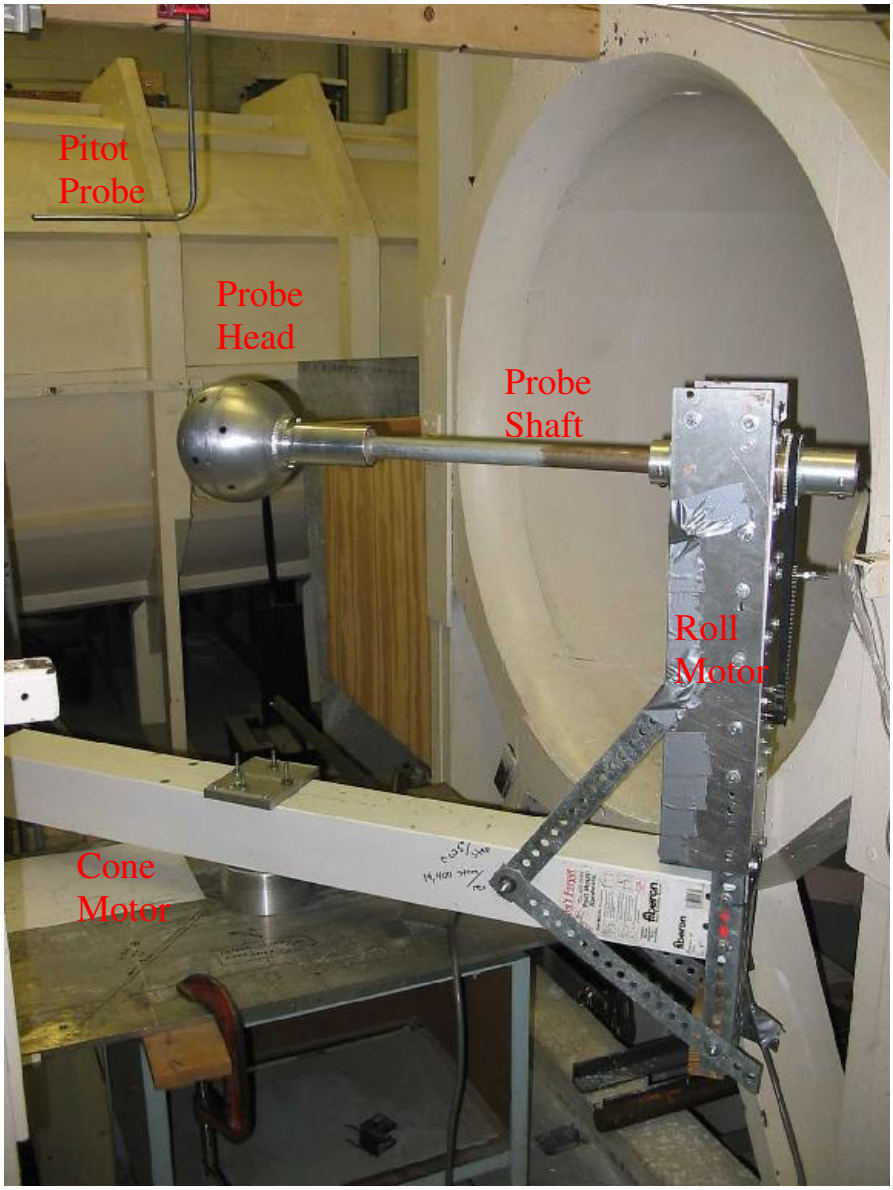

Fig. 4.2 Probe calibration rig – L-frame, cone motor and roll motor.

A pitot-static tube was used to record the dynamic pressure of the tunnel flow. The pitot was mounted slightly ahead (about three probe-head diameters) of the probe to avoid interference from the flow over the probe and at a height of approximately half the radius of the cross-section. Although a complete flow survey of the test section was not done, a check was done to ensure that the dynamic pressure measurement between the

two locations (the sphere location and the pitot location) was within at least 5%. During post-processing this error was corrected by a simple technique described later. Leads from the static and dynamic tubes of the pitot were connected to the ESP and the data was acquired simultaneously along with probe pressure data.

The ESP sensor was calibrated (after sufficient warm up) right before the start of the calibration to minimize errors. Further, during calibration, the zero-pressure reading of the ESP sensor was reset every 30 minutes automatically by the calibration software. At zero setting ($\Theta = 0$, $\Phi = 0$) at the start of the calibration, the plane of the L-frame was arranged perpendicular to the flow direction and the reference plane of the probe (a "flat" machined on the sting) was made level with the horizontal using a bubble level. This level was checked at a few Θ locations spanning the entire range (-45° to +45°) before calibration to ensure that the Θ rotation was not off-axis.

Calibration was performed at two speeds of 10m/s and 25m/s. At each Θ-Φ location the twelve port pressures and the flow dynamic pressure were recorded. The pressure data was sampled at 100Hz and averaged over a period of 1 second. At each new Θ-Φ location the flow was allowed to settle for 2 seconds before taking the readings. The averaging is done in order to reduce aerodynamic noise (flow fluctuations) and also to work as a digital filter for high frequency electronic (instrumentation) noise. The temperature of the flow was simultaneously monitored using a thermocouple installed in the tunnel. This value was used later when computing the density of air in the tunnel. The Θ angle (Fig. 2.3 in section 2) was varied from 45° to 135° (which corresponds to ±45° from the equator) in steps of 2.5° and the Φ angle was varied a full 0° to 360° in steps of 3.75° – resulting in a total of about 3500 calibration points. The choice of the calibration grid density was based on our experience with omni-directional multi-hole probe calibrations such as the 12-hole (section 2) and was judged sufficient to yield good probe measurement accuracies. The calibration time for a complete run at a given tunnel speed was about 3.5 hours.

A validation of the calibration data sets was performed, similar to what was done earlier for the 12-hole probe (refer section 2). For this purpose, an additional 800 test points were also taken interspersed between the calibration points. Good prediction was indicated from the corresponding error estimates.

The pressure coefficient C_p, defined in equation (4.1), was checked for all the ports to see how they matched with the viscous laminar experimental C_p (equation (4.2) from White[46]) and shown in Fig. 4.3 for some of the ports. The difference in the C_p curves indicates that the flow over the sphere was turbulent. This observation was later confirmed (in section 6).

$$C_p = \frac{p - p_\infty}{q_{freestream}} \tag{4.1}$$

$$C_p = 1 - \left(\Theta \cdot (1.5 - \Theta^2 \cdot (0.4371 - \Theta^2 \cdot (0.1481 - \Theta^2 \cdot 0.0423)))\right)^2 \tag{4.2}$$

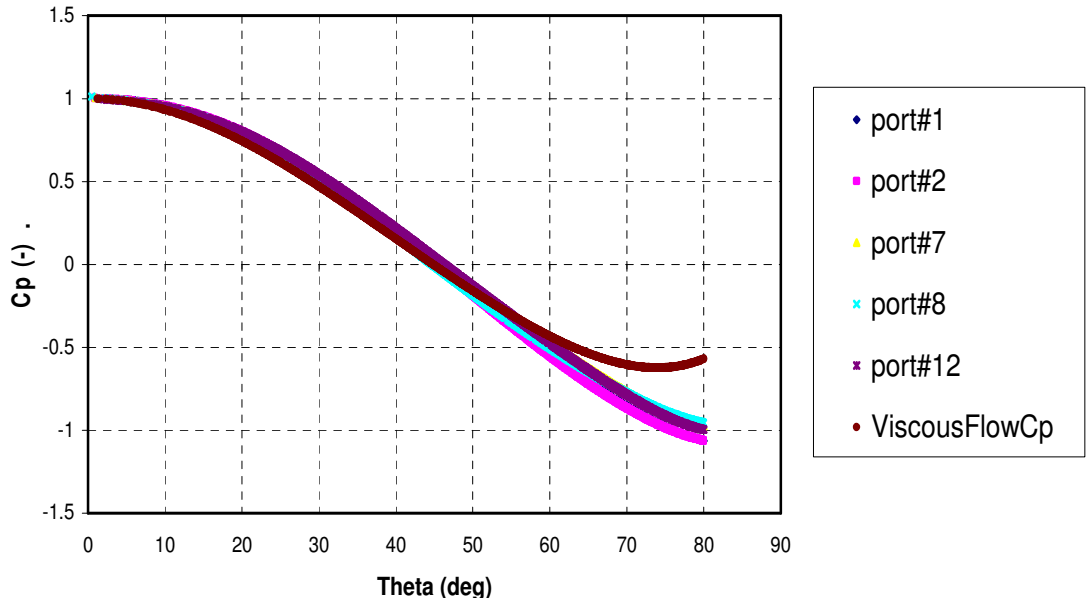

Fig. 4.3 Coefficient of pressure, C_p, obtained from calibration data (curve-fitted).

The calibration data was preprocessed as described for the 12-hole probe in section 2. The sector definitions for the Weatherprobe were described in the previous section. The test data was reduced and the error estimates (for each data set) were obtained. Table 4.1 shows the error data for the calibration data set at 25m/s. This is the minimum error that can be expected from the probe (ignoring sources of errors other than calibration data and reduction scheme).

Table 4.1. Error data from calibration validation – 25m/s.

	Maximum	Mean (μ)	Standard Deviation (σ)
Error in Θ (deg)	3.29	0.005	0.503
Error in Φ (deg)	2.92	-0.001	0.421
Error% in U	3.03	0.004	0.556

Similar errors were seen for the 10m/s calibration data set (shown in Table 4.2). During field testing other sources of error like the sensor accuracy, inertial effects, tubing frequency response etc combine to increase the actual prediction error of the probe.

Table 4.2. Error data from calibration validation – 10m/s.

	Maximum	Mean (μ)	Standard Deviation (σ)
Error in Θ (deg)	3.29	0.005	0.503
Error in Φ (deg)	2.92	-0.001	0.421
Error% in U	3.03	0.004	0.556

4.2 FULL-CONFIGURATION WIND-TUNNEL TESTS

After the probe was calibrated, all the associated instrumentation for the Weatherprobe could be assembled. The goal of the calibration was to find a relation between the pressures and the flow variables of just the probe and not of the associated

instrumentation. This gives us a lot of flexibility in our choice of instrumentation. For example, if there is a need to try a different pressure sensor, that can be achieved without having to recalibrate the probe. The prediction uncertainty of the final Weatherprobe system will be a combination of all the individual instrument uncertainties with the high-accuracy calibration uncertainty itself as the base.

It was decided to test the fully assembled Weatherprobe prototype system in the Aerospace Engineering 3ft x 4ft wind tunnel. The tests were intended to reveal two aspects of the system – 1) an estimate of the prediction accuracy with the Weatherprobe's own Honeywell pressure sensors and IDAN Daq and 2) any unforeseen problems in the coordinated working of the entire system, especially the heating and temperature control circuitry. Since this was just a check and not a full calibration, only a few select Θ-Φ orientations and only a few different tunnel speeds were part of the test matrix.

The 40PC-series Honeywell sensors, as mentioned earlier, have a manufacture-specified accuracy of only 1% FSS. Hence, the prediction accuracy is expected to get a lot worse when compared to the probe's base calibration accuracy (Tables 4.1 and 4.2). After the tests in the wind-tunnel were completed with these sensors, the entire process was repeated for the same test matrix, but after replacing the sensors with a ±5 in. H_2O ESP. The second test was expected to give much lower prediction errors.

A comparison at one stagnation point location (Θ = 100°, Φ = 0°) at three different speeds is shown in Table 4.3. This stagnation point corresponded to a sector, with ports 1, 2, 7, 8 and 12 as the highest five pressures. Hence, these five pressures normalized with the freestream dynamic pressure (q) are shown in the table. The pressure data for this stagnation point from the original calibration data ('Cal Data') is in Row #1. Rows #2 and #3 show the data obtained using the ESP for the same stagnation point. The last

two rows are with the default (Honeywell) sensors. Data at 10 m/s tunnel speed has been ignored for now. The errors in the predicted Θ, Φ and U_{mag} are shown for each case.

Table 4.3. Comparison with ESP pressure data.

	p1/q	p2/q	p7/q	p8/q	p12/q	Θ Error	Φ Error	U_{mag} Error%
Cal Data	0.067	0.331	0.988	-0.348	-0.622	-0.107	-1.314	-1.431
ESP_25m/s	-0.140	0.336	0.936	-0.354	-0.875	-0.507	2.834	2.379
ESP_40m/s	-0.109	0.314	0.936	-0.319	-0.894	1.130	1.867	-0.094
WT_25m/s	-0.138	0.266	0.929	-0.422	-0.833	0.613	1.172	2.317
WT_40m/s	-0.110	0.273	0.922	-0.344	-0.816	1.724	1.237	-0.518

The ESP pressure values are fairly close to the Honeywell pressures ("WT_25ms" and "WT_40ms"). But from the few stagnation points that were checked (those shown in Table 4.3 and many others) with the ESP, no case can be made to show that the ESP can give better results, as can be seen from the error prediction values in the last 3 columns. The ESP pressure data does not match the original calibration pressure ("Cal Data") either although it is (again) fairly close. This was surprising, since better prediction accuracies were expected with the ESP.

The data at any given Θ-Φ orientation was obtained in the following sequence of three steps in terms of the tunnel flow speeds – a few data points at 25m/s, then a step up to 40m/s and then a cut down to 10m/s. A surprising occurrence during the wind tunnel tests was a shift in the predicted Θ and Φ values when nothing except the tunnel speed was changed. This can be seen in Fig. 4.4 for data taken with Honeywell sensors at a fixed probe orientation. The first set of data (up to about 16 in the x-axis) is the Θ error at 25m/s flow speed. The next "step" is at 40m/s and the final one at 10m/s. This fluctuation in the predicted angles were seen even when the pressure data from the ESP was used to predict the flow Θ and Φ. A fluctuation in the flow angularity in the wind

tunnel itself (at different speeds) is a probable cause for this. Note that the errors, though they fluctuate, are still fairly close to zero especially at the higher speeds of 25 and 40 m/s. A similar trend was observed in all the other stagnation points in the test matrix. The errors in prediction were seen to improve considerably by averaging the sampled data over a longer period (1 second). The data in Fig. 4.4 would look as shown in Fig. 4.5 at 10Hz sampling rate.

In order to further improve accuracy, the Weatherprobe's calibration data was "normalized" by making sure that the highest pressure read by the ports match (on an average) the dynamic pressure measured by the pitot probe. The final error prediction for the Weatherprobe with 40PC series sensors can be stated as in Table 4.4.

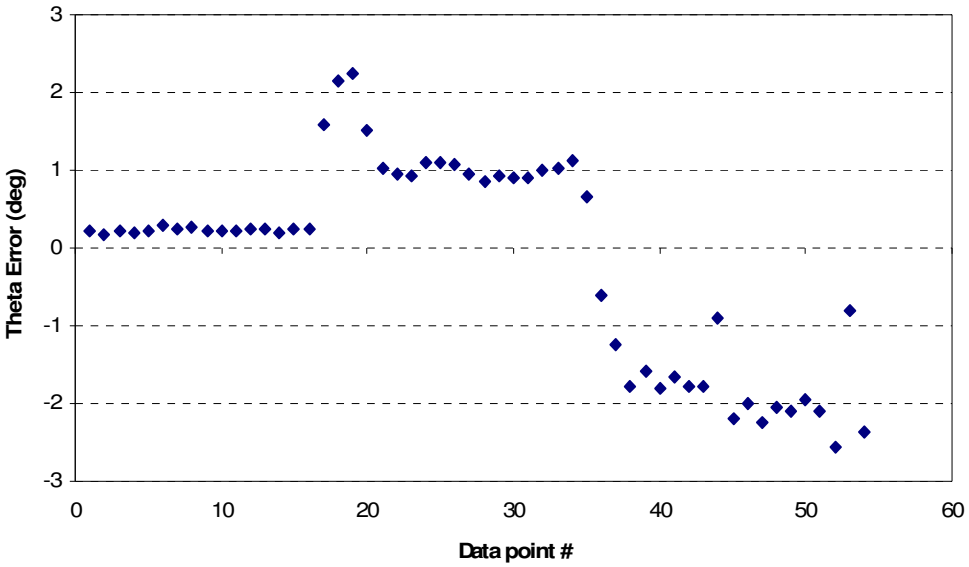

Fig. 4.4 ESP tests: Error in Θ – averaged data.

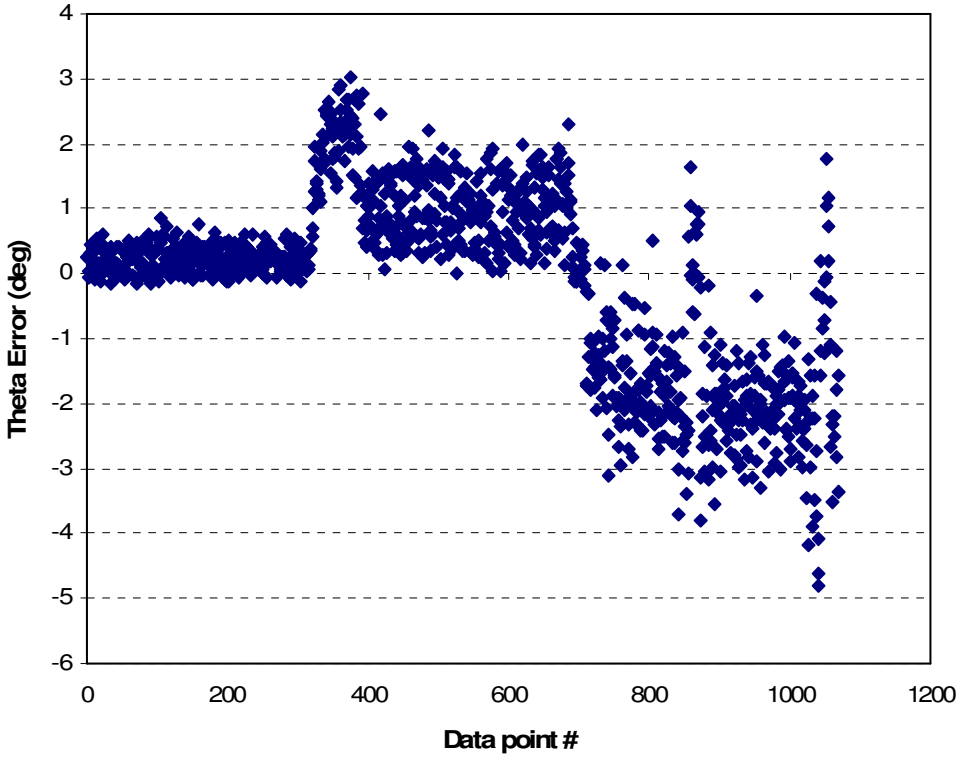

Fig. 4.5 ESP tests: Error in Θ – un-averaged data.

Table 4.4. Error data: full-configuration wind-tunnel tests (50 mmHg sensors).

	Maximum	Mean (μ)	Standard Deviation (σ)
Error in Θ (deg)	3.82	0.67	1.46
Error in Φ (deg)	3.36	0.49	1.14
Error% in U	5.11	0.48	1.90

The above translates to a prediction error of 3° in Θ, 2.5° in Φ and 1m/s in wind speed with 95% confidence.

During a typical probe calibration or testing in a wind-tunnel, compression of flow streamlines by the walls of the test section can cause blockage (Awbi and Tan,[49] Hensel[50]). In our case, the correction is limited only to the freestream velocity magnitude measured by the pitot. A small blockage correction of 1.01 (conservative estimate based on area ratios) was used to correct the flow speed measured by the pitot in the wind tunnel.

The mean errors in Θ and Φ are non-zero and can be subtracted off during field tests. The histograms of the above errors are shown in Figs. 4.6-4.8.

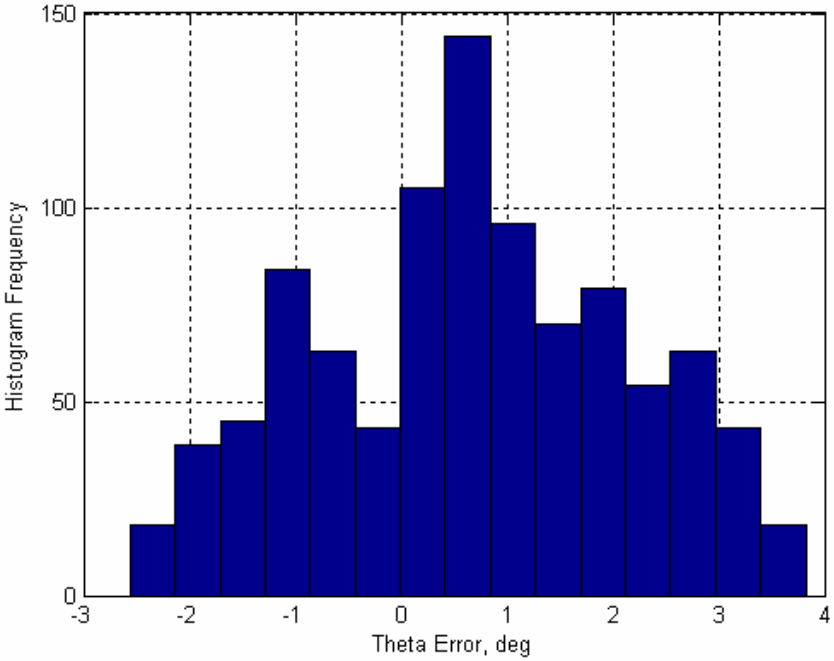

Fig. 4.6 Full-configuration wind-tunnel tests: Histogram of error in Θ.

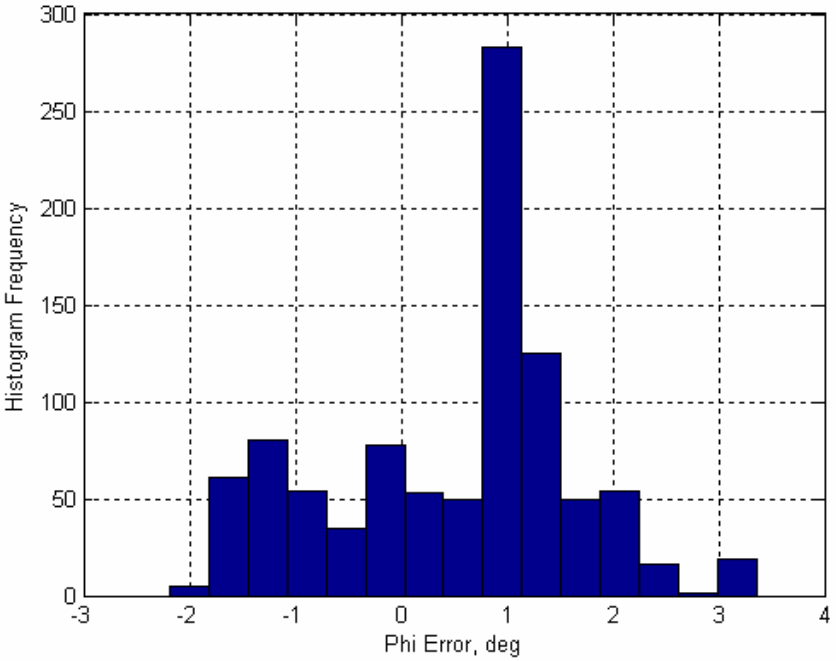

Fig. 4.7 Full-configuration wind-tunnel tests: Histogram of error in Φ.

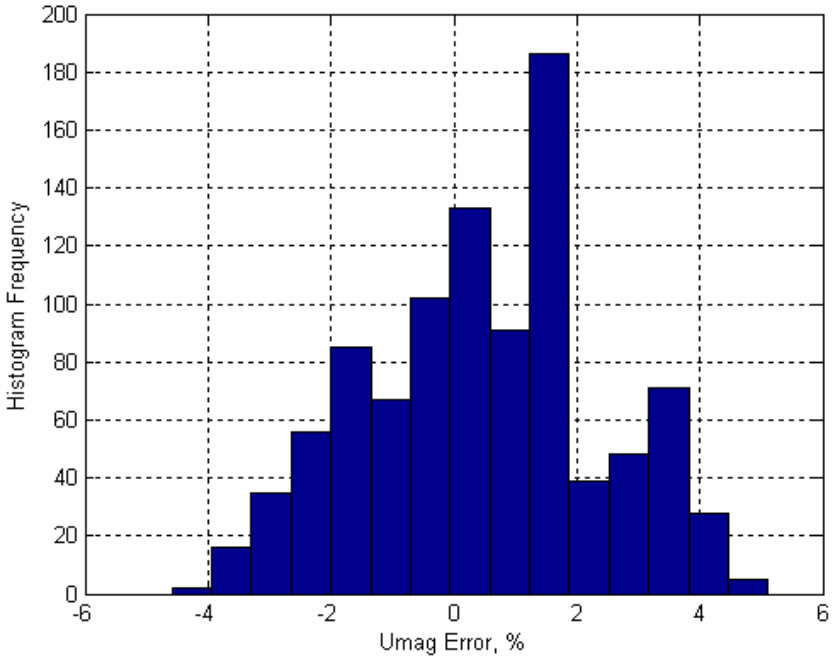

Fig. 4.8 Full-configuration wind-tunnel tests: Histogram of % error in U_{mag}.

Since initial field tests were intended to be done in a test site with wind speeds only up to 10-20 m/s, smaller range pressure sensors (ASDXL series, discussed in section 4) were more suitable. Hence the wind-tunnel tests were repeated with the ASDXL ±5 in. H_2O installed at the pressure ports. A typical comparison plot of the wind speed measured by the Weatherprobe and the pitot probe in the wind-tunnel is shown in Fig. 4.9. The flow speed was varied and set for a few seconds at different values. The Weatherprobe's reading resolutely followed the varying tunnel speeds with good accuracy.

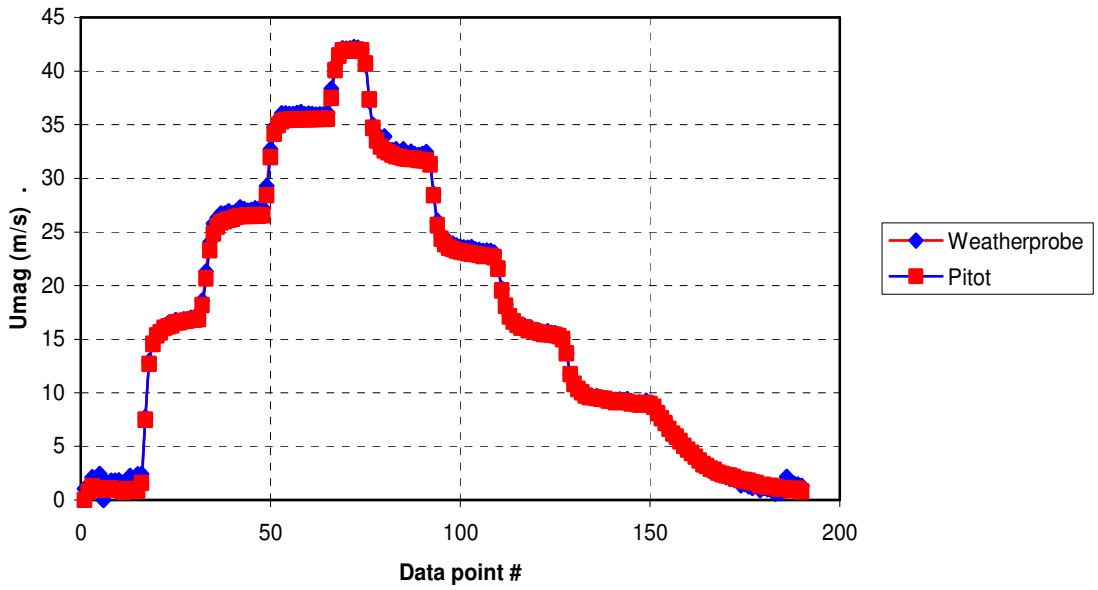

Fig. 4.9 Full-configuration wind-tunnel tests with ASDXL pressure sensors: U_{mag} comparison with pitot probe.

As with the higher-range sensors earlier, tests were conducted at different known orientations of the probe in order to estimate the accuracy in predicted flow angles (Θ and Φ). The overall prediction accuracy is summarized in Table 4.5. As can be seen, there is a notable improvement in the accuracy when compared to the earlier estimates with higher-range sensors (Table 4.4) – the standard deviations are much smaller.

However, the systematic/bias errors in Θ and Φ still persist albeit at a slightly smaller value. As mentioned earlier, the systematic errors can be subtracted off from readings during actual field tests.

Table 4.5. Error data: full-configuration wind-tunnel tests (±5 in.H2O sensors).

	Maximum	Mean (μ)	Standard Deviation (σ)
Error in Θ (deg)	2.80	0.46	1.03
Error in Φ (deg)	3.36	0.67	0.51
Error% in U	3.87	0.55	1.11

4.3 RAIN TESTS

In order to study the effects of rain on the quality of data obtained by the Weatherprobe, it was necessary to design and set up an experiment to simulate rainfall under controlled conditions in the lab. Rain can be simulated by the use of spray nozzles arranged vertically above the probe. The nozzles spew water droplets (and not streams of water) onto the area of interest, in this case the probe head. Full-cone nozzles can produce a round cone-shaped spray pattern completely filled with drops as shown in Fig. 4.10. Depending on the choice of nozzle and (water) supply pressure, any type of rain can be simulated.

For our preliminary study, two types of nozzles were used to produce light and moderate rain respectively. The categorization of the types of rain based on the size of droplets is generally found to be as shown in Table 4.6.

Fig. 4.10 Full-cone spray nozzle from Spraying Systems Co.

Table 4.6. Categorization of intensity of rain.

Type of rainfall	Intensity of rainfall	Droplet size (microns)
1	Light	100-500
2	Moderate	500-1000
3	Heavy	2000-5000

The two brass nozzles with standard NPT pipe threads were 1/4M-12 for light rain and 1/8HH-1 for moderate rain from Spraying Systems Company. The nozzles had a flow rating of 0.10 and 0.19 gpm (gallons per minute), respectively. The nozzle was positioned vertically above the probe. As seen in Fig. 4.11, a flow regulator valve controlled the flow pressure (just before the nozzle) in order to control (and repeat if necessary) the intensity of rain.

Fig. 4.11 Rain-simulation facility: Spray nozzle with pressure gauge.

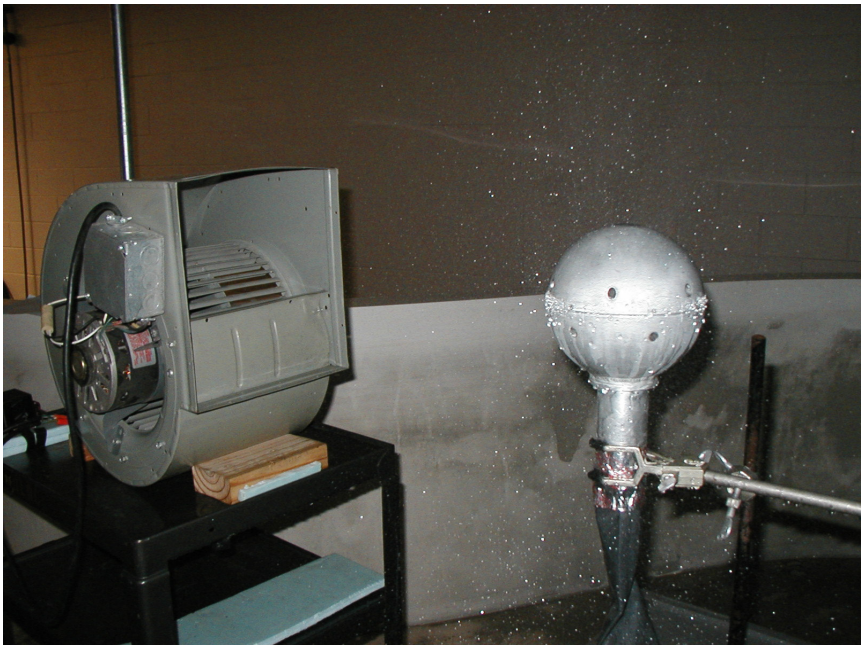

Fig. 4.12 Rain-simulation facility: Weatherprobe in front of a centrifugal blower.

The goal of this experiment was to see how the prediction of flow velocity (by the probe) during precipitation differs from the no-precipitation case. A 10 in. x 8 in. centrifugal blower able to produce speeds up to 15 m/s was set up to generate wind. The entire setup is shown in Fig. 4.12.

The test matrix drawn up for the experiment consisted of all (nine) combinations of the following scenarios 1) no rain or type 1 rain or type 2 rain, 2) V = 0 or V = 10 or V = 15 m/s. In each case the probe was positioned at different angles with respect to the flow velocity in order to eliminate any dependency of the analysis on probe orientation.

Let us consider a typical case where, at a constant blower setting and with the probe positioned at 24 in. from the blower exit, a flow of ~11m/s was generated at the location of the probe. Readings (U_{mag}, Θ and Φ) were taken over a number of points with and without rain. The data are compared in Figs. 4.13-4.15.

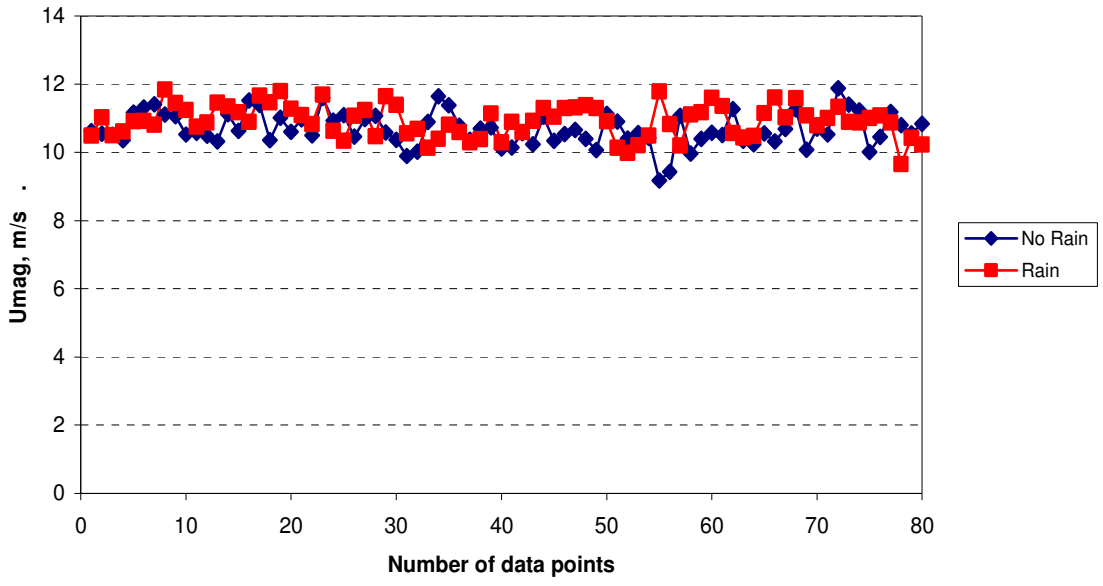

Fig. 4.13 Rain tests: Comparison of U_{mag} (moderate rain, 11m/s).

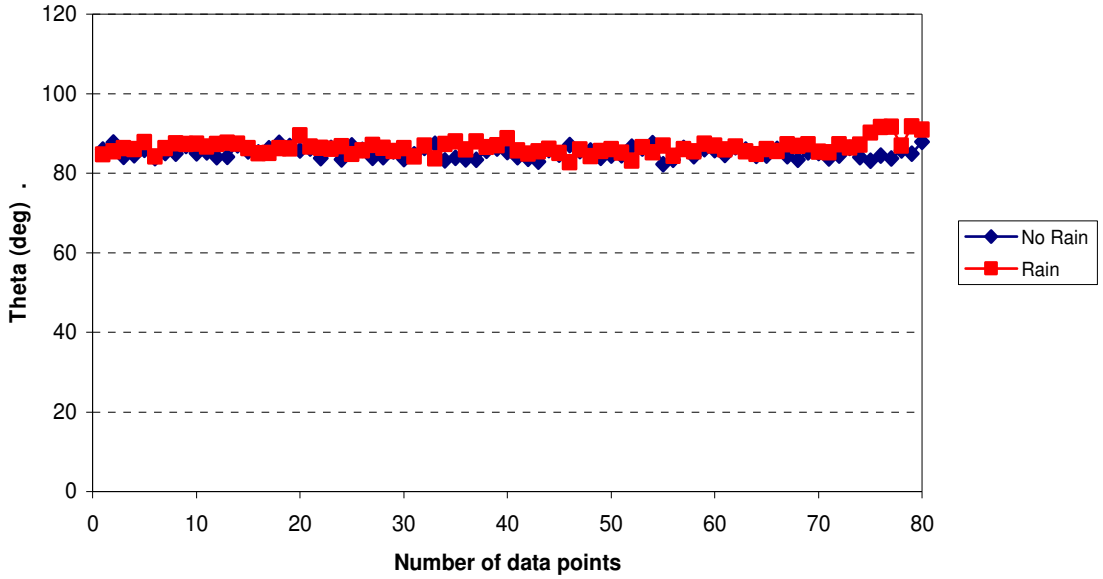

Fig. 4.14 Rain tests: Comparison of Θ (moderate rain, 11m/s).

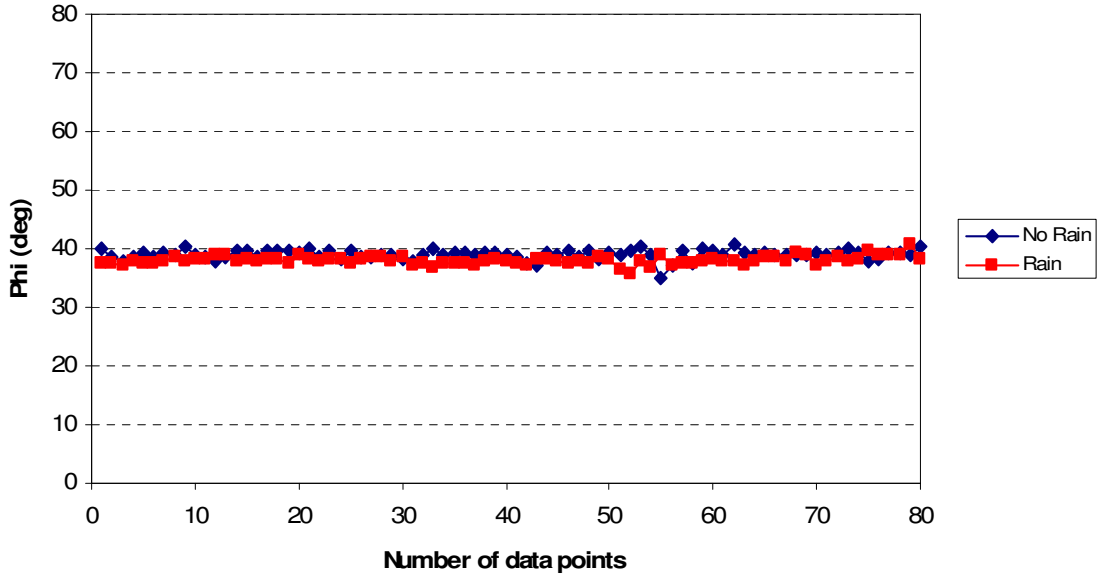

Fig. 4.15 Rain tests: Comparison of Φ (moderate rain, 11m/s).

The "noise" in the flow speed data is a result of the flow quality (turbulence) from the blower and can be ignored by looking at averaged data. The average U_{mag} was 10.68 m/s in the first case and 10.93 m/s in the second (rain) case. As can be seen from the figures, rain has minimal or no effect on the probe's readings. The pressure data itself was analyzed in both cases and no noticeable change was found. Similar results were obtained with other cases in the test matrix (other intensities of rain and at higher speeds (up to 15m/s)). This test thus proved the capability of the probe to work well in rainy conditions, an essential design requirement. This is an encouraging result especially when noting the fact that the performance of sonic anemometers in rain is highly suspect owing to their measuring technique being notoriously sensitive to raindrops crossing the sound propagation paths (Peters et al.[51]).

4.4 FIELD TESTS

The Weatherprobe was installed at the summit of a 25 meter tall tower (Fig. 4.16) next to an existing 3-D sonic anemometer and a rotating-cup anemometer of the Meteorology Department, Texas A&M University. The field test was intended to prove the stand-alone workability of all associated hardware of the Weatherprobe and also provide a further insight into the accuracy of the probe when compared to the two very popular anemometers.

A picture of the probe installed at the top of the tower is shown in Fig. 4.17. The sonic anemometer is a Campbell Scientific Inc. (model CSAT3) which measures three-dimensional wind speed with the following manufacture-specified accuracy:

- for wind vector within ±5° of horizontal → < ±2 percent of reading
- for wind vector within ±10° of horizontal → < ±3 percent of reading
- for wind vector within ±20° of horizontal → < ±6 percent of reading

Fig. 4.16 Weatherprobe installed at the top of a 25m tall tower.

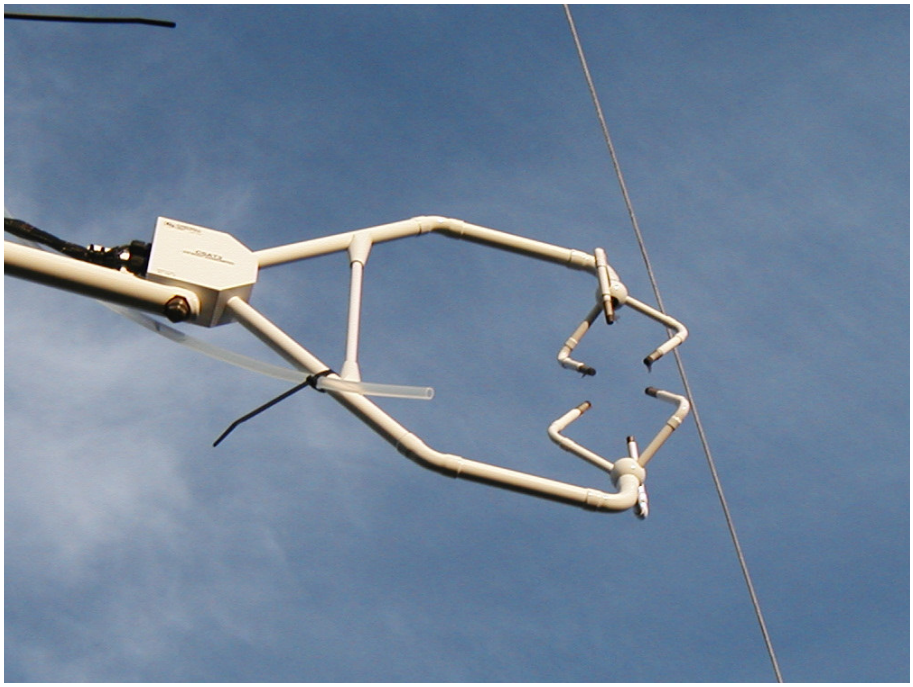

Fig. 4.17 Sonic anemometer: Model CSAT3 from Campbell Scientific Inc.

The sonic anemometer has a maximum range of 65m/s with a sampling rate up to 60Hz. However, the stated accuracy above is for wind speeds only up to 30m/s. Although not a crucial parameter in meteorological studies, the spatial resolution of the CSAT3 is ~4 in. which also is comparable to the Weatherprobe (6 in.). The sonic was at a height of approximately 26 meters from the ground.

The rotational cup anemometers in the field were Met One Instruments, Inc.'s models 034B and 014A. The 034B model was installed at a height of 26 m right next to the sonic anemometer. The 034B model has a range of 75 m/s. As specified in the manufacturer's sheet, this instrument had the following accuracy in wind speeds

- for wind speeds < 10m/s → ±0.1 m/s
- for wind speeds > 10m/s → ±1.1% true

and a wind direction accuracy of ±4°. The 014A model was installed at a height of about 22 m height, roughly 1 m below the Weatherprobe. The 014A model has a range of 45 m/s and the following wind speed accuracy (as specified in the manufacturer's sheet): ±0.1 m/s or 1.5% FS (full scale). Both instruments had a starting threshold speed of 0.4 m/s. A picture of the Model 034B from Met One Instruments, Inc. is shown in Fig. 4.18.

Data was acquired from all four instruments over a period of 3.5 days with the following sampling frequencies.

- Weatherprobe: 1 Hz
- Sonic Anemometer: 10 Hz
- Cup Anemometers (1 and 2): 1 min

In order to compare the data in the same platform, the data from the Weatherprobe and the sonic anemometer were averaged to get 1 min data. Since the goal of the field study is to validate the Weatherprobe, the following comparisons were performed: Weatherprobe vs. sonic anemometer and Weatherprobe vs. cup anemometer (014A).

Fig. 4.18 Cup anemometer: Model 034B from Met One Instruments, Inc.

Since the instruments were installed at different heights, the wind speed measured by the Weatherprobe was corrected using logarithmic profile law (equation (4.3)) commonly used in near-surface micrometeorological studies (Arya[52]).

$$U(z) = \frac{u^*}{k} \ln\left(\frac{z - z_0}{d}\right) \tag{4.3}$$

where, z = measurement height

u* = friction velocity

k = von Karman's constant

z0 = roughness length

d = displacement height

Hence, for two instruments at heights z1 and z2, the ratio of the wind speeds is given by:

$$\frac{U(z_1)}{U(z_2)} = \frac{\ln\left((z_1 - z_0)/d\right)}{\ln\left((z_2 - z_0)/d\right)} \tag{4.4}$$

Based on commonly used values (Arya[52]) z0 = 0.5 m and d = 8 m were used for our purposes. The wind speed readings from the Weatherprobe (at 23 m) were corrected by a ratio of 1.05 and 0.98 before comparing them with the sonic (at 26 m) and cup (at 22 m) anemometers, respectively. Further, in the latter case, only the horizontal component of wind velocity computed from the Weatherprobe was compared with the cup anemometer.

Weatherprobe vs. sonic anemometer

The wind speed (U_{mag}) data for the entire period of 3.5 days from the two instruments was first checked for synchronicity by cross-correlating the 1-second data (sonic anemometer's data was initially averaged from 10Hz to 1Hz). Fig. 4.19 shows this cross-correlation. As can be seen, there is a lag of about 18 seconds in the sonic anemometer's data probably as a result of errors in the data-acquisition timers/clocks of either instrument. Hence the time-stamp in the sonic data was adjusted for this lag before any further comparisons. Further, both data-sets were checked at the beginning to ensure that all (1Hz) time-stamps were logged. If a time-stamp was found missing due to software bugs, it was padded with dummy (zero) values. Such data points were very few and are unlikely to affect the analysis in any significant way.

Once the lag was adjusted, both data-sets were averaged into 1-minute data and compared in Fig. 4.20. The Weatherprobe's U_{mag} in the figure has been corrected for the height difference using the correction factor obtained earlier. By visual inspection, it is seen that there is a very good correspondence between the two instruments. As expected, the Weatherprobe does not perform well at low speeds (< 2 m/s). There is a base reading of ~ 2m/s even when there is no wind. This was seen earlier during wind-tunnel tests and is due to the noise in the pressure sensors which causes a very low signal-to-noise (SNR) ratio at low (or zero) wind speeds. It is important to note that this is *not* an offset error. At higher wind speeds, when the flow dynamic pressure is at least, say, 2% of the range of the pressure sensors (±5 in. H_2O), the signal is not drowned out by the noise and

reasonable wind speed (and direction) data are obtained. Hence the range of the probe can be stated to be from 2m/s to 45m/s. Use of better pressure sensors will alleviate this problem, but is an expensive solution. A better alternative is to include external circuitry to "clean" the sensor signal in future versions of the prototype. The latter option might require a trade-off in very-high-frequency data acquisition. To get a clearer picture of the correspondence between the two data sets, Fig. 4.21 shows a zoomed-in version over a period of half a day.

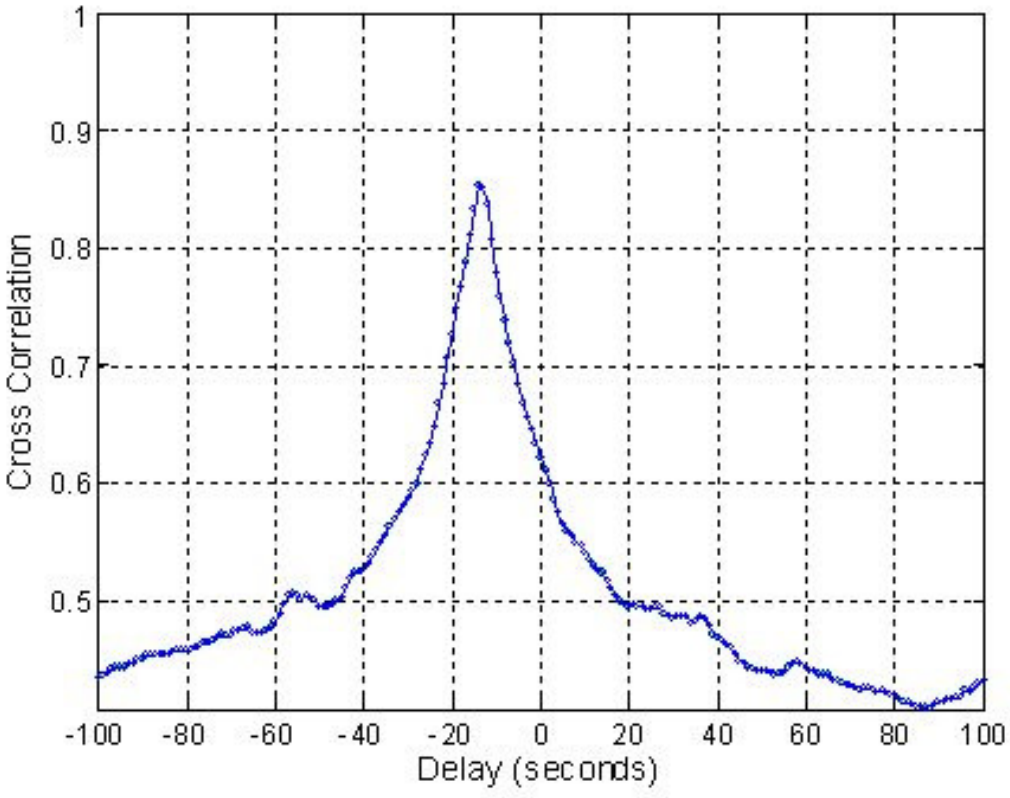

Fig. 4.19 Cross correlation between Weatherprobe and sonic anemometer – raw U_{mag} 1-second data.

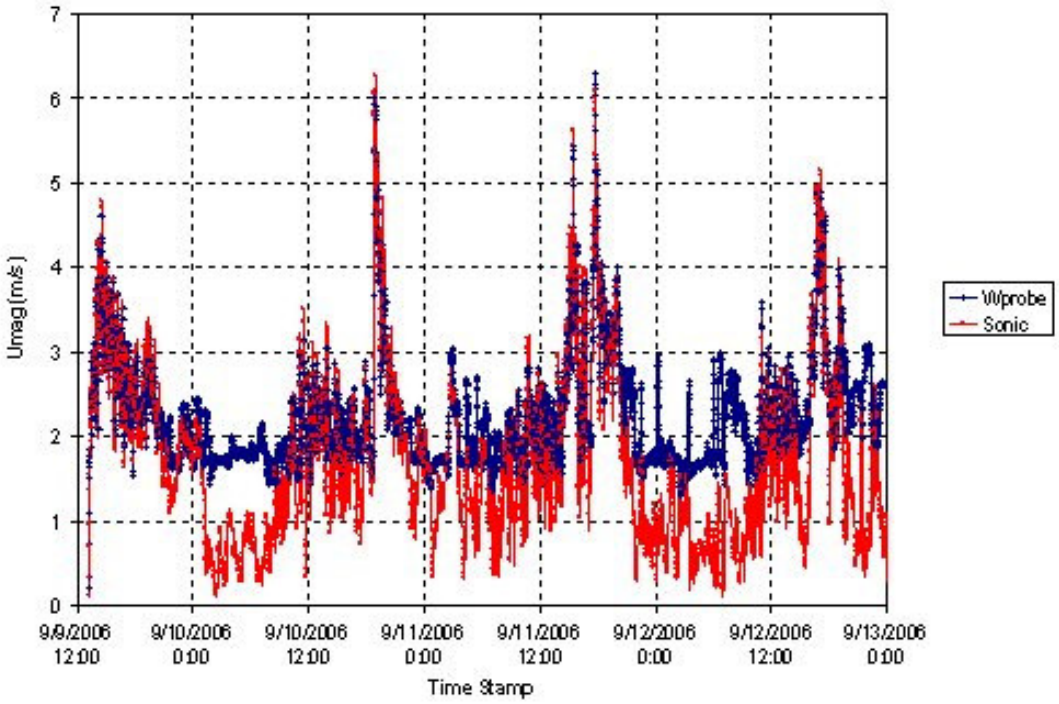

Fig. 4.20 Weatherprobe vs. Sonic Anemometer: U_{mag} – averaged 1-minute data over 3.5 days.

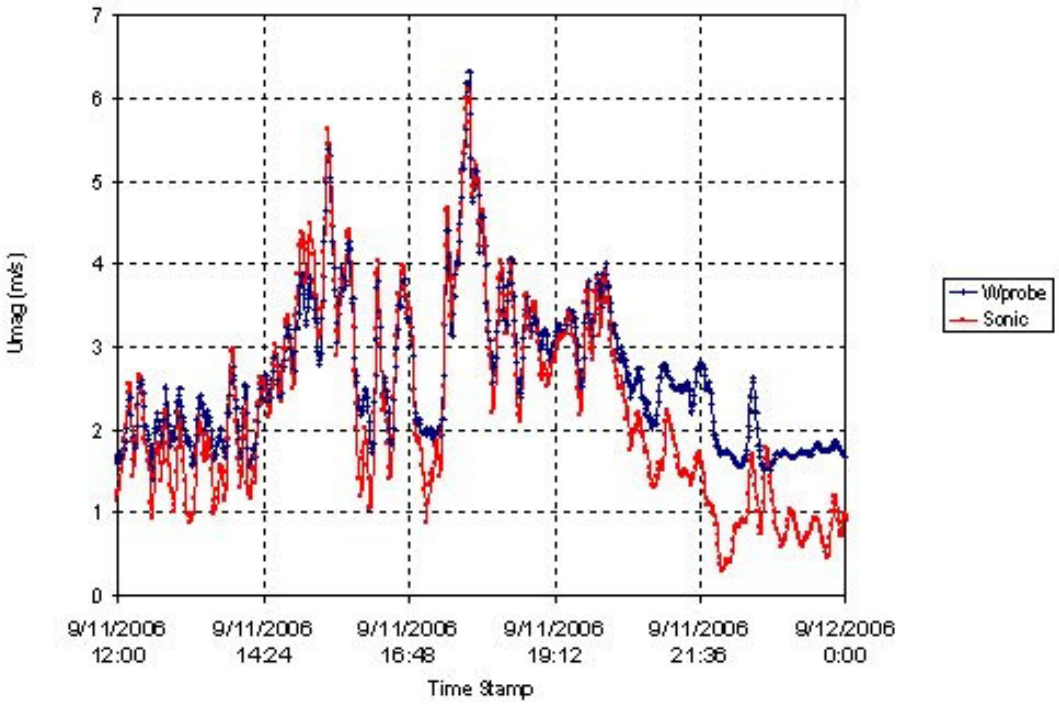

Fig. 4.21 Weatherprobe vs. Sonic Anemometer: U_{mag} – averaged 1-minute data over half a day.

Another way to compare the data is to juxtapose them directly on the x- and y- axes and see how they match up to the ideal x = y line as shown in Fig. 4.22. Again, there is a good correspondence between the two. If the sonic anemometer is considered as the reference (or true) measurement, an error parameter (ε) for the Weatherprobe can be defined – simply as the difference between the two measured values at every time-stamp. Hence the mean (μ) and standard deviation (σ) can be computed for this error. For the Weatherprobe-sonic anemometer comparisons, these error statistics are:

$\mu = 0.028$ m/s

$\sigma = 0.355$ m/s

which are small and hence indicative of good data.

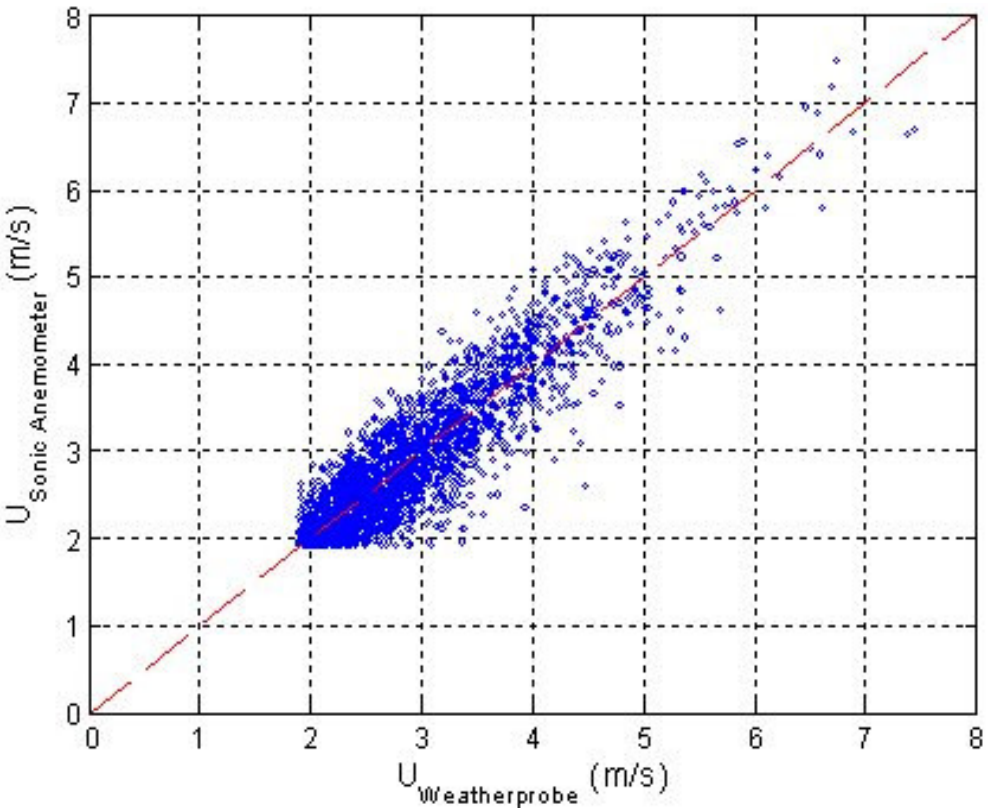

Fig. 4.22 Weatherprobe vs. Sonic Anemometer: U_{mag} – direct comparison of averaged 1-minute data over 3.5 days.

The cross-correlation for the above 1-minute data was also checked to ensure synchronicity (remember that the lag in the sonic data was checked and corrected earlier). Fig. 4.23 provides confirmation with the (near-unity) peak at zero delay (in minutes).

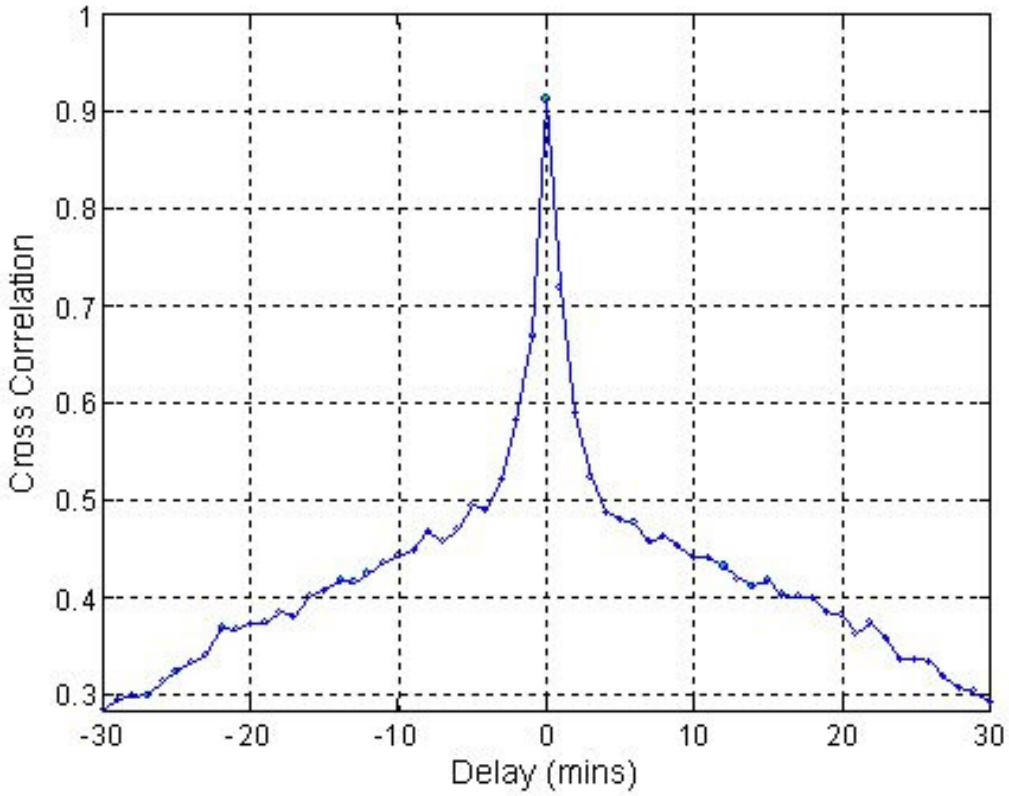

Fig. 4.23 Weatherprobe vs. Sonic anemometer: U_{mag} – cross-correlation after lag correction – averaged 1-minute data.

The two data sets were smoothed using a moving average of window-size 5 points (i.e., a 5-minute moving average) and the correspondence is shown in Fig. 4.24. The smoothing caused the error statistics to become even better as expected:

$\mu = 0.028$ m/s

$\sigma = 0.208$ m/s

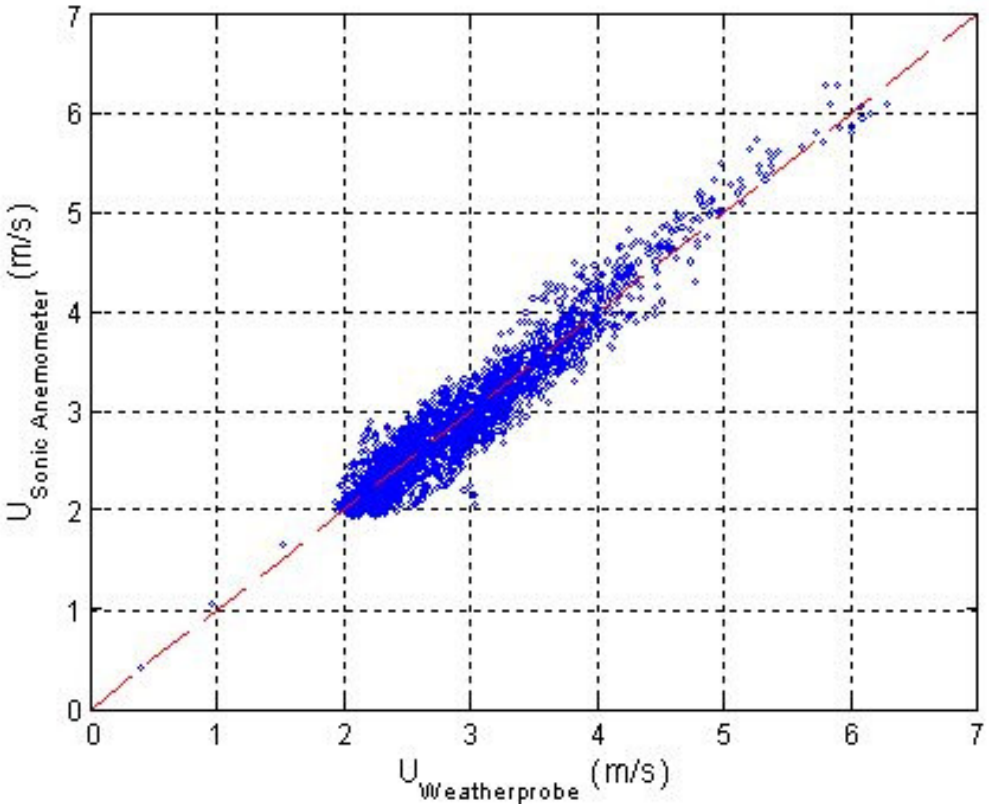

Fig. 4.24 Weatherprobe vs. Sonic anemometer: U_{mag} – direct comparison of moving-averaged (smoothed) 1-minute data over 3.5 days.

However the smoothing, of course, causes further loss of frequency information in the data and is suitable only if the time scale of interest is large. Many micrometeorological studies observe data over days, even weeks, with 30-min or 1-hour averages. The smoothing (even with a bigger window size) can be employed in such cases.

Up until now, only the total wind speed has been compared between the two instruments. The angles Θ and Φ (wind direction) are presently compared. The sonic anemometer's data is typically logged as three components of the wind-velocity. Earlier, its U_{mag} was obtained by calculating the resultant. The angles Θ and Φ for the sonic anemometer were calculated from the three components using the standard spherical coordinate system (Fig. 3.1b) and compared with those of the Weatherprobe in Figs.

4.25 and 4.26. Again, only a zoomed version over a short period is shown in for easy visual inspection. As can be seen, there is a good correspondence between the Θ values and the values are close to 90° (horizontal) most of the time. There are, however, high errors in Θ (at either end of the x-axis) at the points with U_{mag} < 2m/s. This indicates that the Weatherprobe's data is unusable at low wind speeds (< 2m/s). Fig. 4.26 shows the comparison in Φ. A good correspondence is seen here too. The reference planes for Φ for the two instruments were not coincident. The sonic anemometer was installed facing the south (by visual inspection) i.e., when the wind is blowing from the south, Φ = 0. Although the Weatherprobe was not aligned with the south, the angle its reference plane makes with the south was corrected before plotting Fig. 4.26.

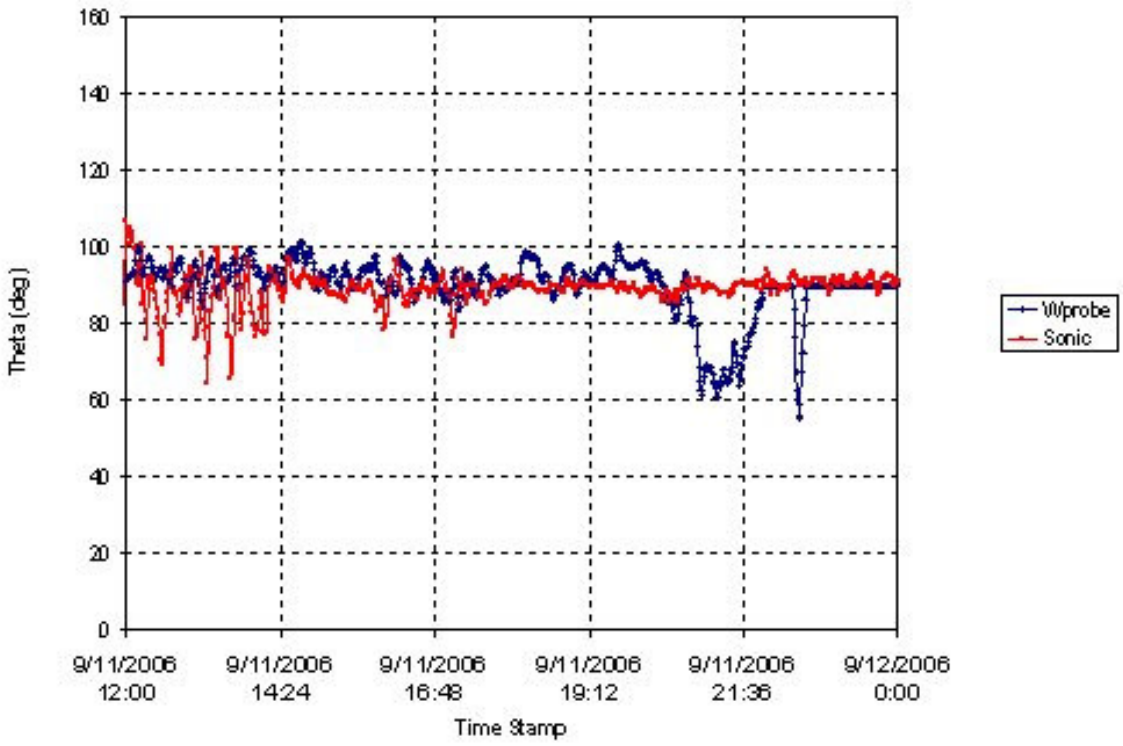

Fig. 4.25 Weatherprobe vs. Sonic Anemometer: Θ – averaged 1-minute data over half a day.

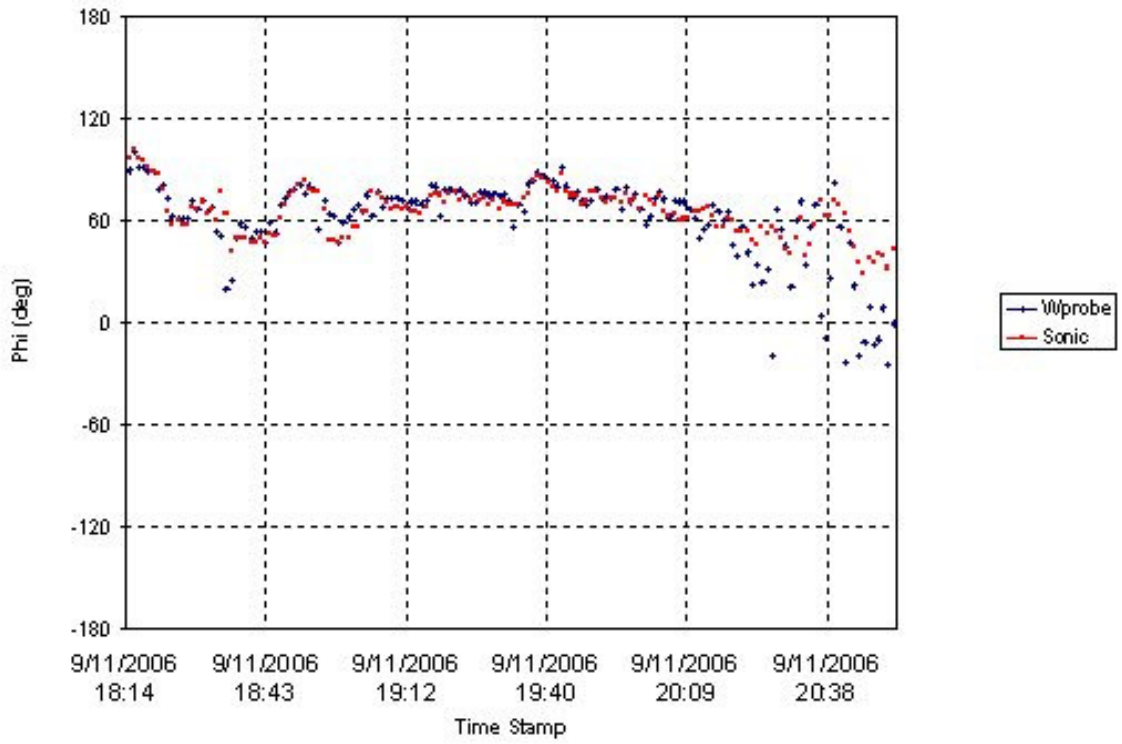

Fig. 4.26 Weatherprobe vs. Sonic Anemometer: Φ – averaged 1-minute data over half a day.

Weatherprobe vs. cup anemometer

Comparisons were performed, similar to the previous analysis, between the Weatherprobe (at 23 m height) and the cup anemometer (at 22 m height) with corresponding corrections for height. In this case, however, only the horizontal wind speed magnitude from the Weatherprobe was compared with the cup anemometer's wind speed reading, since the cup anemometer fails to respond to any vertical components in the wind velocity. Due to some damage in the cup anemometer's wind vane, direction data was not available for comparison. The comparison plot for U_{mag} over the same 3.5-day period is shown in Fig 4.27.

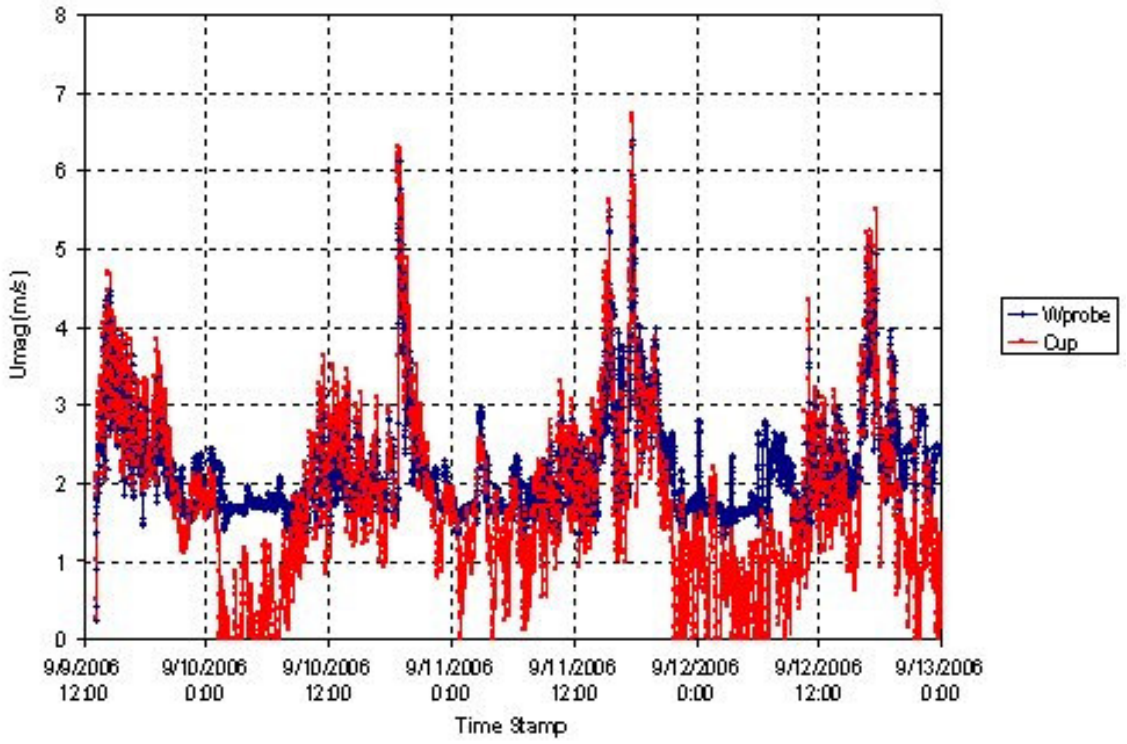

Fig. 4.27 Weatherprobe vs. Cup Anemometer: U_{mag} – averaged 1-minute data over 3.5 days.

Similar errors in the Weatherprobe's readings are seen at low speeds. The correspondence is more evident in Fig. 4.28 which has the following error statistics:

μ = -0.116 m/s

σ = 0.448 m/s

There is an overall bias error and this bias tends to get higher at higher speeds. The standard deviations are also higher. The cup anemometer is not an instrument as accurate as the sonic anemometer and that is conjectured as the reason. The cross-correlation between the Weatherprobe (averaged to 1-minute data) and the cup anemometer (1-minute data), however, was free of any lags as seen in Fig. 4.29.

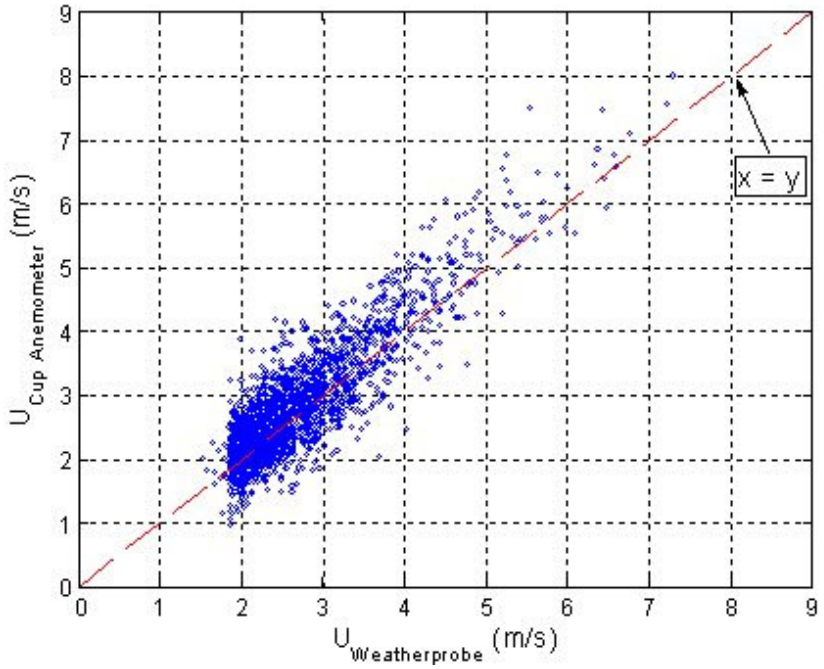

Fig. 4.28 Weatherprobe vs. Cup Anemometer: U_{mag} – direct comparison.

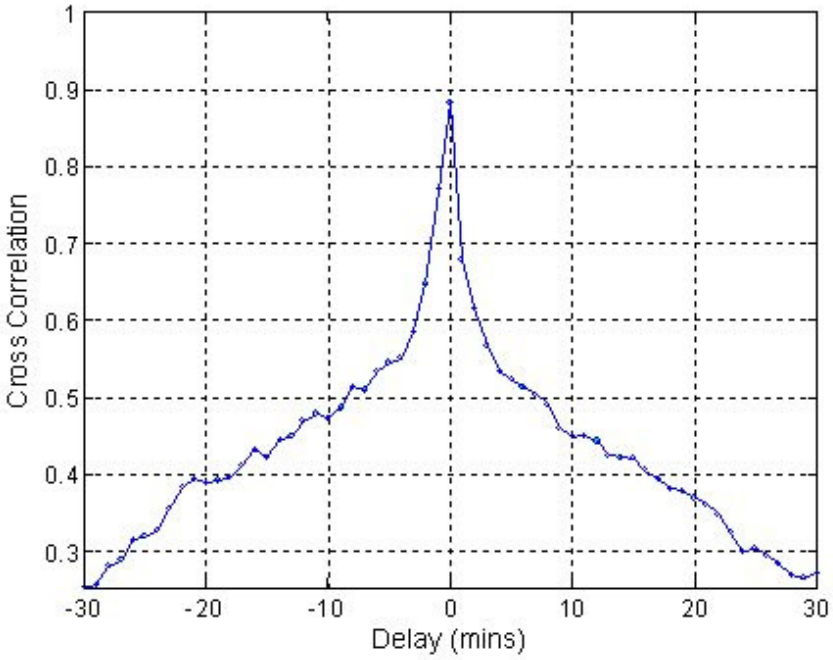

Fig. 4.29 Weatherprobe vs. Cup anemometer: U_{mag} – cross-correlation – averaged 1-minute data.

5 ALIGNMENT BIAS-ERROR CORRECTIONS IN PROBE CALIBRATIONS

5.1 PROBLEM DEFINITION

When calibrating multi-hole velocity probes in a wind-tunnel, an offset (or bias) error often exists in the recorded flow angles due to errors in aligning the traverse system exactly with the flow direction and due to the angularity of the tunnel flow itself. These offset angles are hard to quantify from direct measurements with any degree of accuracy. Although they are usually small (less than 0.5° in most good calibrations), these errors still need to be corrected in order to increase the flow measurement accuracy of the probe. In this work, a method is developed that computes offset errors in all types of multi-hole probes – from the traditional 5- and 7-hole probes to the omni-directional 18-hole probe and the next-generation 12-hole probe – using simply the pressure data obtained during their calibration. A mathematical expression, involving the original calibration angles and the predicted offset angles, was derived with which the calibration data can be corrected before the probe is put into use. The method faired well under tests for robustness and consistency with a multitude of experimental calibration data. The method, when compared to an earlier method, was found to perform much better in terms of accuracy.

The coordinate system widely used for straight probes is akin to a standard spherical coordinate system (the same as defined earlier) and is shown again here in Fig. 5.1 with angles Θ (cone angle) and Φ (roll angle) determining the stagnation-point location on the surface of a probe in a flow field of velocity vector $\mathbf{U}$. The x_p-y_p-z_p coordinate frame in the figure is a probe-fixed coordinate system and also the inertial frame of reference when the probe is in use for flow studies. A good way to interpret the coordinates is by visualizing that if the probe is first rolled by Φ about x_p and then coned by Θ about the *new* z_p the probe will now be aligned with $\mathbf{U}$.

During calibration, the probe is initially aligned (as perfectly as possible) with the velocity vector. The velocity vector is fixed in the inertial frame X-Y-Z. Therefore, to obtain calibration data at various $\{\Theta, \Phi\}$, a reverse process to the one described above is followed – i.e., rotating the probe by $-\Theta$ about z_p (rotation #1 in Fig. 5.2) and then rotating the probe by $-\Phi$ about the probe-axis x_{p1} (rotation #2 in Fig. 5.2). Note that, at the start of the calibration, the initial orientation of the probe coordinate system x_p-y_p-z_p is coincident with X-Y-Z. Also, note that the final orientation of the probe coordinate system (x_{p2}-y_{p2}-z_{p2}) with respect to **U** is equivalent to that in Fig. 5.1.

A picture of the probe mounted at its zero setting ($\Theta = 0$, $\Phi = 0$) at one of our jet calibration facilities is repeated here in Fig 5.3 (same as Fig. 2.5). Ideally, the point $\Theta = 0$, $\Phi = 0$ should be the stagnation point when the probe axis is initially aligned with the flow prior to calibration. In other words, x_p should be parallel to **U** in Fig. 5.2. But, as mentioned earlier, this is hardly ever the case. The alignment will be off by a small amount quantified by offset angles δ and ξ, the horizontal and vertical offset angles respectively. The geometric definitions of these angles are shown in Fig. 5.4. If the probe is yawed (i.e., rotated about Z) from its zero setting by δ (rotation #1 in Fig. 5.4) and then pitched (i.e., rotated about Y') by ξ (rotation #2 in Fig. 5.4), the probe axis will be perfectly aligned with the flow direction. Note that a yaw-pitch scheme has been used for the offset angles different from the cone-roll scheme for probe coordinates (Fig. 5.2). This scheme, as will be seen later, was found to greatly simplify the offset calculations. Offset angle errors, δ and ξ, will be referred to simply as "offsets" from now on.

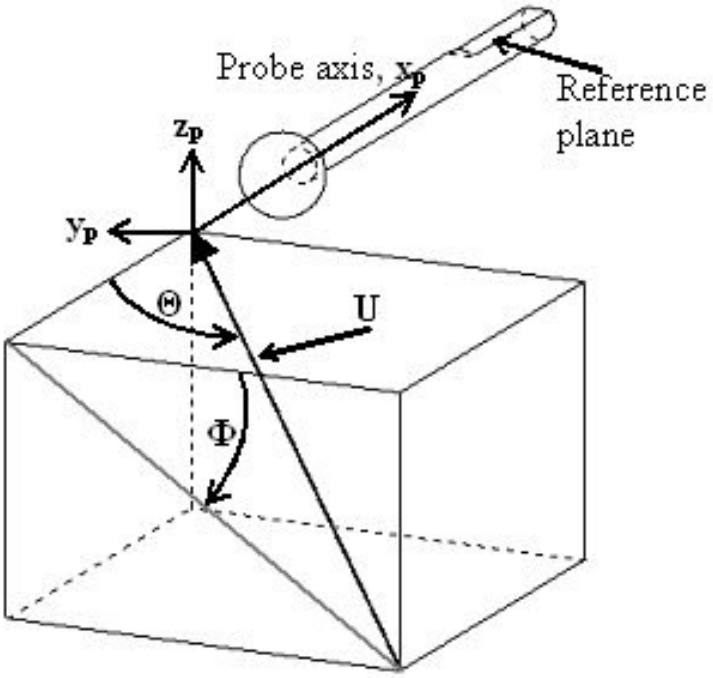

Fig. 5.1 Standard probe coordinate system.

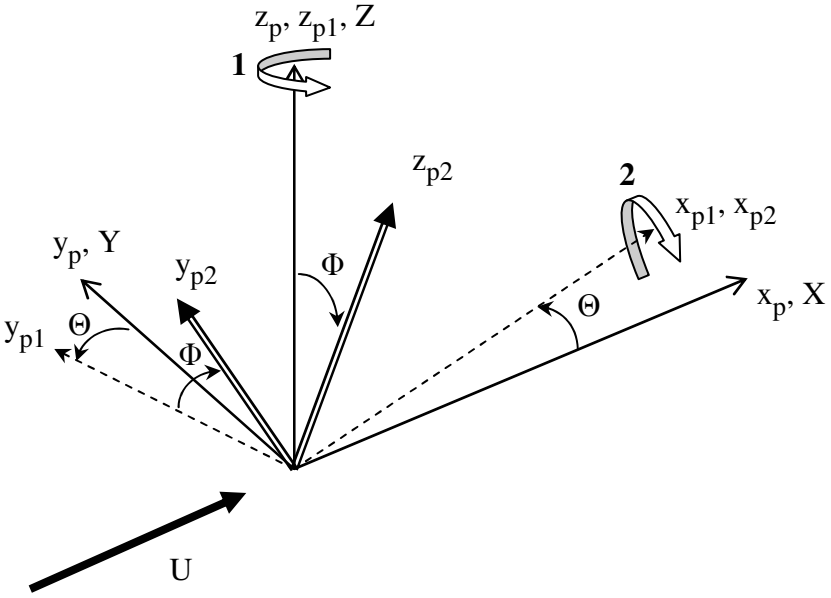

Fig. 5.2 Maneuvers to attain desired flow angles (Θ, Φ) during probe calibration.

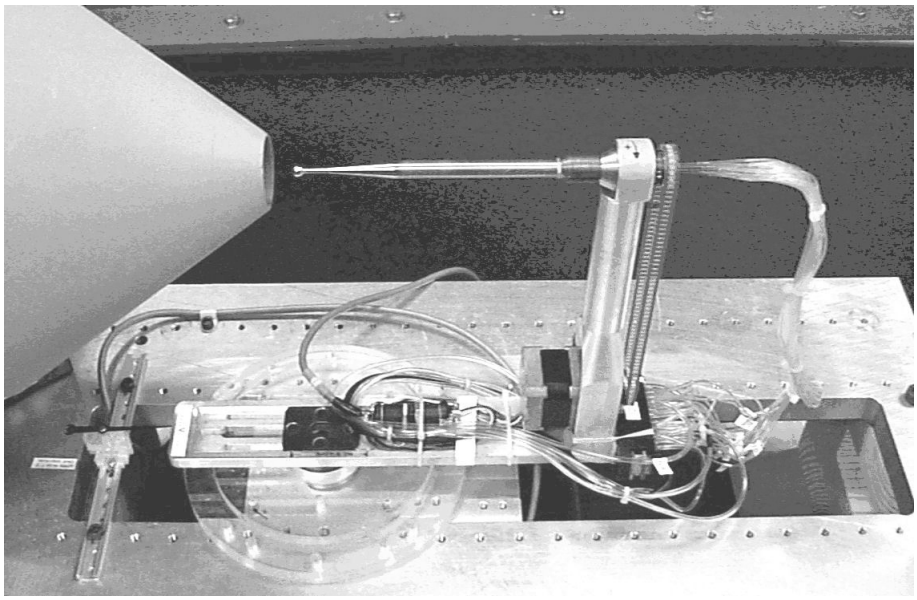

Fig. 5.3 Picture of our jet calibration facility with a probe mounted in its initial ("zero") setting.

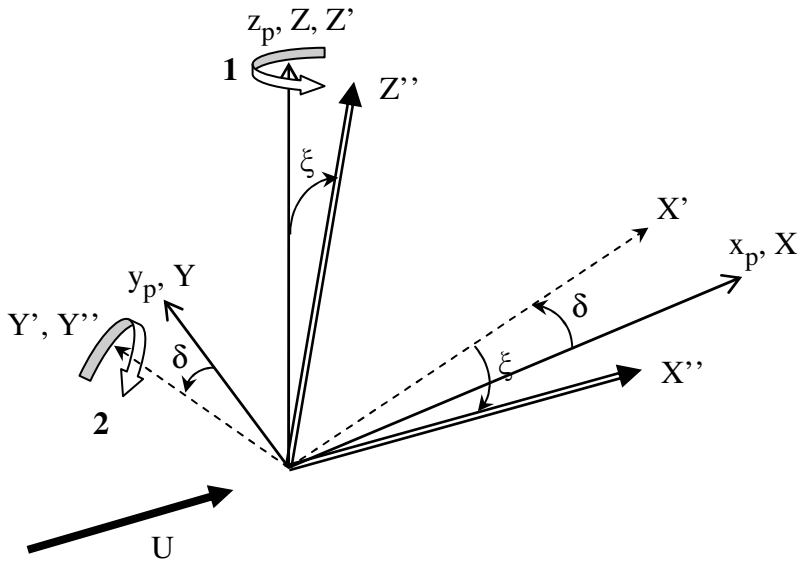

Fig. 5.4 Maneuvers to align probe axis with the actual flow direction, a.k.a offset angle errors (δ, ξ).

Our goal is to calculate {δ, ξ} directly from probe calibration data. Once the offsets are known, the probe's cone and roll angles {Θ, Φ} in the calibration data, originally

defined in the X-Y-Z frame, should be corrected to $\{\Theta_c, \Phi_c\}$ with respect to the new frame X''-Y''-Z'' in Fig. 5.4. In other words, it is required to find what rotations of Φ_c and Θ_c (Φ_c followed by Θ_c) will reset the probe-axis (x_{p2} in Fig. 5.2) to X'' (same as **U**) in Fig. 5.4. At the end of this maneuver, the probe's y_p-axis and z_p-axis need not necessarily be aligned with Y'' and Z'' (unless $\xi = 0$). The sequence of rotations can be summarized as:

a) From the inertial frame,

1. δ about Z (Fig. 5.4)
2. ξ about Y' (Fig. 5.4)

Mathematically, using rotation matrices:

$$\begin{bmatrix} X" \\ Y" \\ Z" \end{bmatrix} = \begin{bmatrix} c\xi & 0 & -s\xi \\ 0 & 1 & 0 \\ s\xi & 0 & c\xi \end{bmatrix} \begin{bmatrix} c\delta & s\delta & 0 \\ -s\delta & c\delta & 0 \\ 0 & 0 & 1 \end{bmatrix} \begin{bmatrix} X \\ Y \\ Z \end{bmatrix} \tag{5.1}$$

b) From the inertial frame,

1. $-\Theta$ about z_p (Fig. 5.2)
2. $-\Phi$ about x_{p1} (Fig. 5.2)
3. Φ_c about x_{p1} (Fig. 5.2; rotation not shown)
4. Θ_c about new z_p i.e., z_{p3} (not shown)

Mathematically, using rotation matrices:

$$\begin{bmatrix} X" \\ Y''' \\ Z''' \end{bmatrix} = \begin{bmatrix} c\Theta_c & s\Theta_c & 0 \\ -s\Theta_c & c\Theta_c & 0 \\ 0 & 0 & 1 \end{bmatrix} \begin{bmatrix} 1 & 0 & 0 \\ 0 & c\Phi_c & s\Phi_c \\ 0 & -s\Phi_c & c\Phi_c \end{bmatrix} \begin{bmatrix} 1 & 0 & 0 \\ 0 & c\Phi & -s\Phi \\ 0 & s\Phi & c\Phi \end{bmatrix} \begin{bmatrix} c\Theta & -s\Theta & 0 \\ s\Theta & c\Theta & 0 \\ 0 & 0 & 1 \end{bmatrix} \begin{bmatrix} X \\ Y \\ Z \end{bmatrix} \tag{5.2}$$

where, $s\Phi = \sin(\Phi)$ and

$c\Phi = \cos(\Phi)$, etc.

Now the components of X" (the axis that was aligned) can be equated and elementary algebra performed to obtain the following equations relating the corrected coordinates $\{\Theta_c, \Phi_c\}$ to the calibration coordinates $\{\Theta, \Phi\}$ and the offsets $\{\delta, \xi\}$.

$$\Theta_c = \cos^{-1}\left(\cos(\xi)\cos(\Theta + \delta)\right) \tag{5.3a}$$

$$\Phi_c = \tan^{-1}\left(\frac{\cos(\xi)\sin(\Phi)\sin(\Theta+\delta)-\sin(\xi)\cos(\Phi)}{\cos(\xi)\cos(\Phi)\sin(\Theta+\delta)+\sin(\xi)\sin(\Phi)}\right) \tag{5.3b}$$

As a quick check, if $\delta = \xi = 0$ is substituted in equation (5.3), the corrected coordinate values are obtained as $\Theta_c = \Theta$ and $\Phi_c = \Phi$, as expected. Alternately, if $\Theta_c = \Theta$ and $\Phi_c = \Phi$ is set in equation (5.2), the entire sequence of rotations collapses into an identity matrix which also serves as a basic check.

5.2 BASIC IDEA FOR SOLUTION METHOD

The offsets for any multi-hole calibration can be obtained from the pressures of any single port alone. Hence, for the sake of analysis, let us consider a spherical-head probe with just one port at $\Theta = \Theta_p$ and $\Phi = \Phi_p$ as shown in Fig. 5.5. It is a 2-D representation of the curved surface of the front of the probe i.e., as seen from the direction of the freestream in line with the probe-axis x_p. The axis of the probe passes through point A normal to the probe surface. Point O is the actual stagnation point (due to offset) at zero setting, the location of which has the angle coordinates $\{\delta, \xi\}$ as defined earlier in Fig. 5.4.

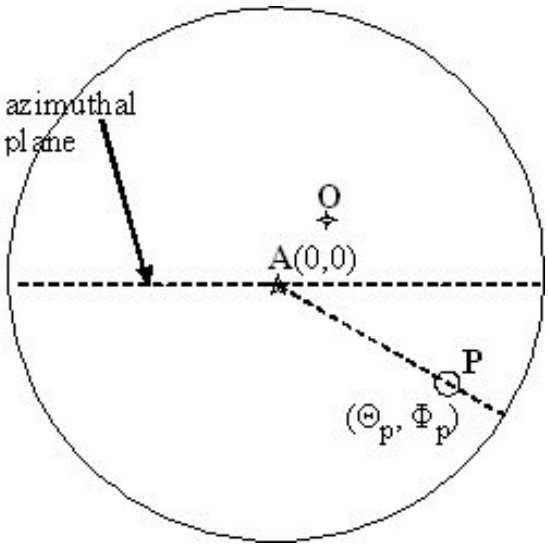

Fig. 5.5 Probe tip (view in line with probe axis) – at zero setting.

Obtaining a calibration data point at any Θ, Φ involves measuring the pressure at port P after moving the probe as described in Fig. 5.2 – along the azimuthal plane by Θ and then rotating by Φ (counter-clockwise in Fig. 5.5) about A. Now consider two calibration points obtained by the above maneuver, one at $\Theta = \delta$ and $\Phi = \Phi_p$ (point A' in Fig. 5.6a) and the other at $\Theta = \delta$ and $\Phi = 180° + \Phi_p$ (point A'' in Fig. 5.6b). The port is now in the azimuthal plane in both cases, at P' and P'' respectively. The stagnation point (or offset) is now "vertically" above at a pitch angle of ξ. Since these two calibration points are symmetrically opposite (irrespective of ξ), the pressure measured in each case should be the same assuming constant freestream dynamic pressure (q_{dyn}). Hence, δ corresponds to the cone angle at which the above is true. In actual calibrations, since q_{dyn} fluctuates by a small amount from point to point, a non-dimensionalized pressure can be used to check the above equality. This quantity is defined as the offset coefficient,

$$C_\delta = \frac{P_p}{q_{dyn}} \tag{5.4}$$

where, P_p is the pressure at port p.

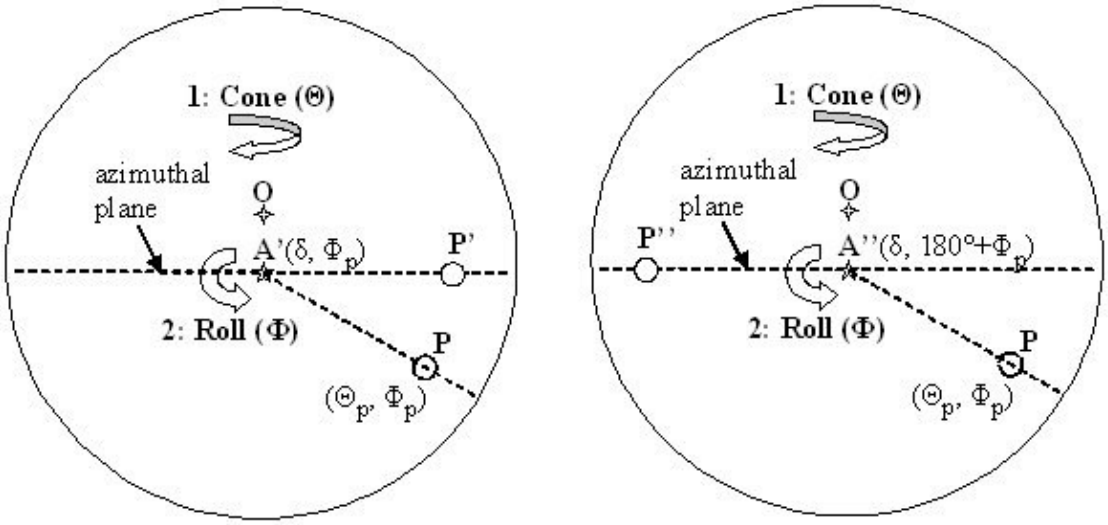

Fig. 5.6 Probe tip (view in line with probe axis) – a) after (δ, Φp) maneuver, b) after (δ, 180°+Φp) maneuver

To find ξ, the same process can be repeated, but with $\Phi = 90°+\Phi_p$ and $\Phi = 270°+\Phi_p$ as the two calibration locations. Of course, this is strictly true only if δ has already been corrected in some way or if $\delta = 0$. Actually employing this method in practice is tedious and impractical for multi-hole probe calibrations and impossible if ξ is non-zero. For negligible ξ, one can envision a trial-and-error process of setting different δ and finding the one that satisfies the required condition. The pitching movement required to find ξ cannot be physically achieved with the cone-roll setup of straight probes. Furthermore, manual correction cannot be done prior to calibration since the port locations (Θ_p, Φ_p) are not precisely known. Manually finding the offset angles after calibration is a waste of time if it can be found computationally using the data at hand. Hence, an algorithm that calculated δ and ξ from pressure (calibration) data was developed, while still using the same idea of equality of non-dimensionalized pressures at the two symmetric locations.

5.3 DEVELOPMENT OF ALGORITHM WITH THEORETICAL DATA

The *true* value of the offsets in an experimental calibration data is not known and cannot be measured with any acceptable degree of accuracy. Therefore, the offsets are calculated using some method, there are no known values with which to compare our results. Hence, for a basic feasibility study of an offset-calculation algorithm, theoretical calibration data (based on equation (1.2)) for our hypothetical 1-hole probe was generated first for testing. With theoretical data, one can introduce any offset while generating the data and thus check the accuracy of calculated values. In later sections of this paper, tests were done with actual calibration data and yielded good results. A typical calibration data for the 1-hole probe is shown in Table 5.1.

The first step is to find the coordinate location of the port. This involves plotting a 3-D surface with the port pressure (non-dimensionalized with dynamic pressure) on the z-axis and the coordinate angles Θ and Φ on the x- and y- axes as shown in Fig. 5.7. The port location $\{\Theta_p, \Phi_p\}$ will be at the apex of this surface where the pressure is maximum.

In the figure, that would be at {35, 30} degrees. An efficient maximization routine was coded in Matlab to this end.

Table 5.1. Typical format of a calibration data.

Θ	Φ	P_p	q_{dyn}
1.8	0	19.26	61.25
1.8	2.7	22.22	60.91
1.8	5.4	23.53	61.33
-	-	-	-
-	-	-	-
3.6	0	18.32	61.47
-	-	-	-

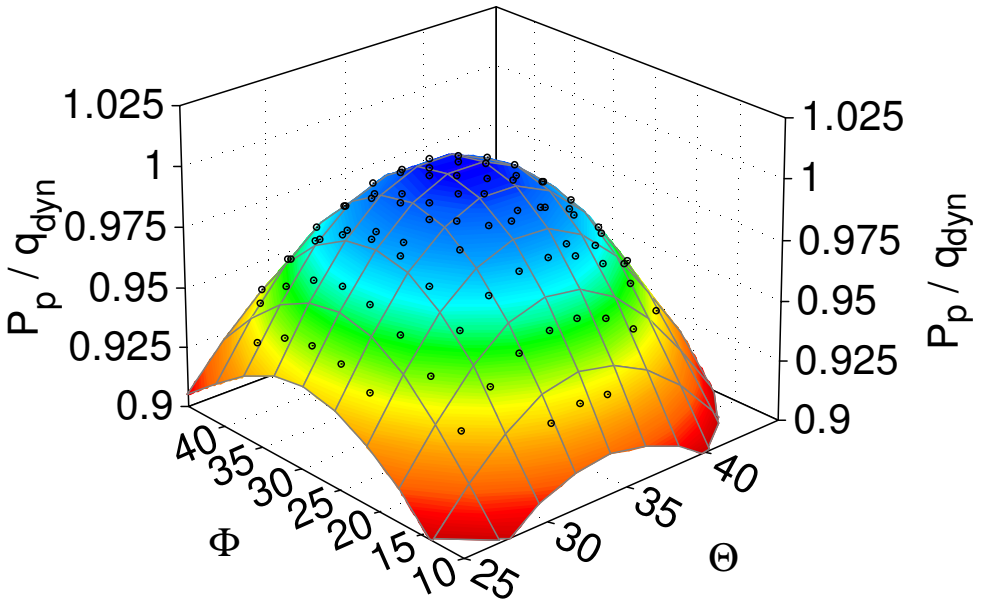

Fig. 5.7 Typical port pressure (normalized) at nearby calibration points.

From calibration data, the offset coefficient C_δ is calculated using equation (5.4) at all calibration points. The coefficient is then plotted at $\Phi = \Phi_p$ for cone angles ranging from some Θ_i to Θ_f (round dots in Fig. 5.8). Since the behavior of C_δ only near $\Theta = \delta$ is of interest and since δ is typically small, Θ_i of 2°-4° and Θ_f of 10°-12° was found to work

well. Θ_f was large enough to capture the trend of C_δ variation and yet not too far from the offset location. The coefficient is then plotted similarly for a range of cone angles at $\Phi = 180°+\Phi_p$ (square dots in Fig. 5.8). Since calibration data is almost always never available at the exact Φ_p (or $180°+\Phi_p$), a local least-squares surface fit was used that used all nearby calibration data points to calculate C_δ at any intermediate $\{\Theta, \Phi_p\}$.

The Θ value at the point of intersection in the offset plot is the horizontal offset (δ). The equivalence in the definitions of Θ and δ (Figs. 5.2 and 5.4) should be noted here. At the point of intersection, the C_δ value is equal at the symmetric port locations (Fig. 5.6) of Φ_p and $180°+\Phi_p$. The δ offset is about -1.0° in the plot. The calibration data is now corrected for the horizontal offset using equation (5.3) by setting $\xi = 0$. Then the vertical offset is calculated using the same principle i.e., using C_δ values calculated at $\Phi = 90°+\Phi_p$ and $\Phi = 270°+\Phi_p$ (not shown in figure). The coefficients for the line-fit in the offset plot for δ can directly be used for the ξ case. The calibration data is corrected again for ξ.

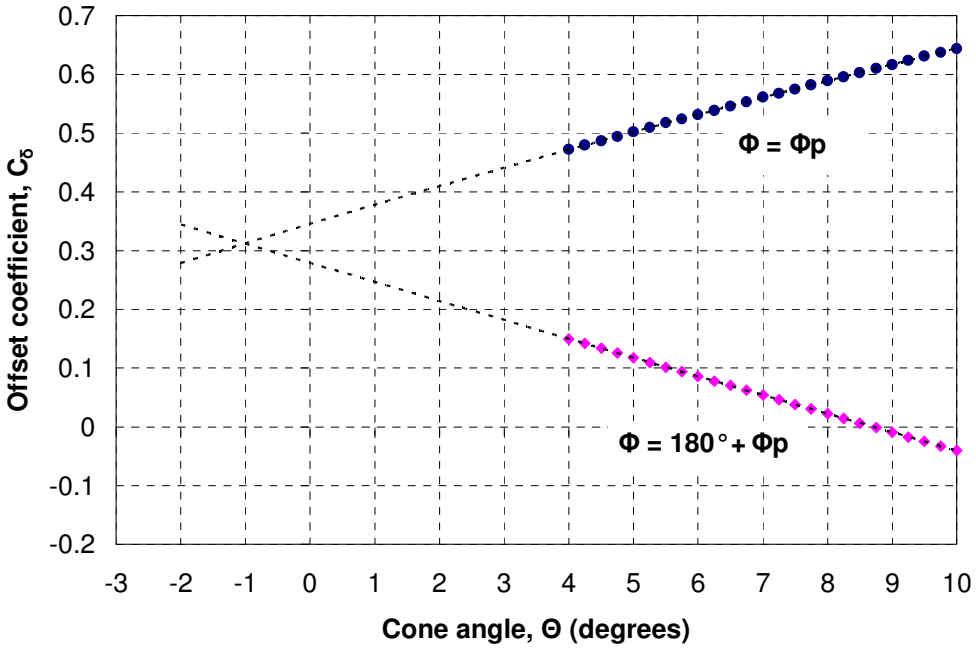

Fig. 5.8 Typical offset plot.

A few key elements of the algorithm excluded from the overall description above were:

1) Quadratic local-least-squares (LLS) surface-fit: As mentioned earlier, to find the port-pressure at a test point $\Theta = \Theta_{test}$, $\Phi = \Phi_p$ (typically not available directly from calibration data), nearby calibration points (Θ_{cal}, Φ_{cal}) are selected from the calibration database based on Euclidean distance in Θ-Φ space. The search routine to find the nearest points uses a quadrangulation check to ensure that the points are distributed in all "quadrants" around the test point as described in Ramakrishnan and Rediniotis[17]. A surface fit of these selected points (typically 15 to 20 in number depending of density of grid points) is performed, which is essentially a bi-variate polynomial with coefficients k_i:

$$C_\delta = k_0 + k_1 \cdot \Theta_{cal} + k_2 \cdot \Phi_{cal} + k_3 \cdot \Theta_{cal}^2 + k_4 \cdot \Phi_{cal}^2 + ... \qquad (5.5)$$

Then, C_δ is calculated at the desired point by substituting Θ_{test}, Φ_p in equation (5.5). A quadratic fit was found to be sufficient for good accuracy.

2) A second order fit was found to be essential for the offset plot also, as opposed to linear fits used in earlier methods. The need for a second order fit is evidenced in Fig. 5.9. The dotted lines are the quadratic fits. The solid line is a linear fit. The difference in the calculated δ between the two is about 0.3°, which, although small, is on the order of current multi-hole probes' prediction accuracies.

3) δ is calculated by iterative convergence. In each iteration, the calculated δ is used to correct the calibration data (equation (5.3)) and this corrected calibration data is used for the next iteration. Iterations are necessary since Φ_p gets modified with any change in calibration data (due to offset correction). Typically three to four iterations were found to be sufficient to compute δ. The ξ value is calculated after δ is fully corrected. This is because, the offset-plot method for ξ is strictly valid only when the calibration data has no horizontal offset errors as described earlier. Furthermore, the vertical offset calculation uses the fit-coefficients from the horizontal offset plots. If ξ is corrected simultaneously, any error in δ can progressively induce errors in the corrected calibration data over each iteration thus drifting the solution away.

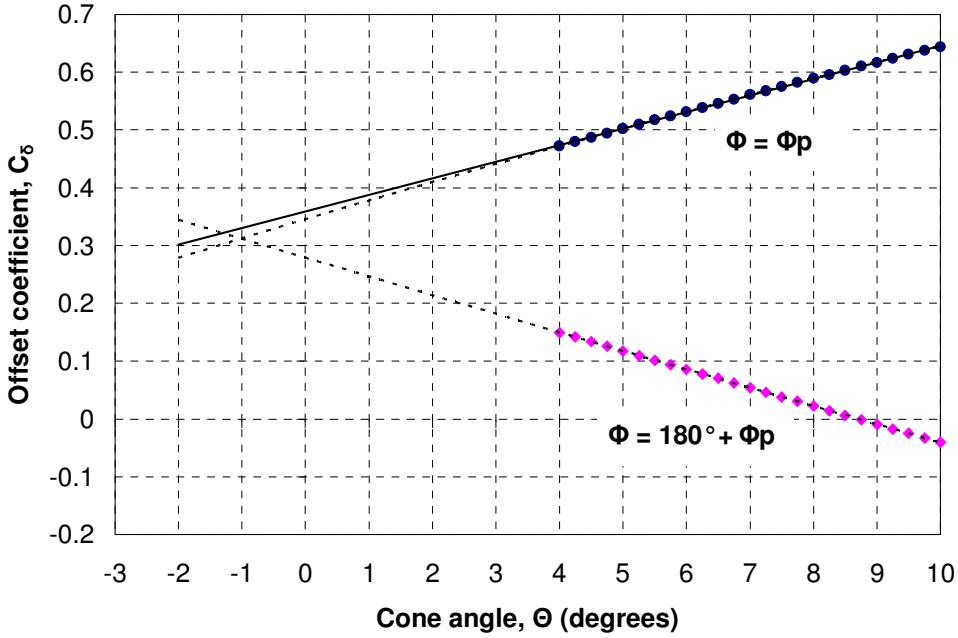

Fig. 5.9 Offset plot showing linear and quadratic fits.

Different offsets were artificially introduced in the theoretical data to see if the code predicts the offsets and corrects the data. A comparison of the offsets set (actual) and predicted is shown in Table 5.2.

Table 5.2. Comparison of predicted offsets to actual offsets (theoretical data).

Actual (δ, ξ)	(0, 0)	(0, 1)	(2, 0)	(2, 1)
Predicted (δ, ξ)	(-0.01, -0.07)	(0.00, 0.95)	(1. 89, 0.05)	(1.85, 1.06)

The algorithm predicts the offsets very well. Since Θ and Φ in the original calibration data are progressively corrected in each iteration, the final form of the calibration data handled by the algorithm is free of offset errors and ready for use. The original calibration data was also corrected directly (using actual δ and ξ in equation (5.3)) for comparison. The two corrected data matched well. The offset-prediction algorithm can be expected to work well with experimental data, especially for the omni-directional 18-

and 12-hole probes (since they have a spherical head). There is reasonable confidence at this point in its applicability to experimental 5-hole (and 7-hole) calibration data also.

5.4 COMPARISON WITH AN EARLIER METHOD

The algorithm developed in the previous section has its roots in a previous work by Zeiger and Schaeffler[25]. The earlier method was developed for 5- and 7-hole probes, the port locations for which are shown in Fig. 5.10 as seen from the direction of the calibration freestream. Also shown in the figures are the standard numbering schemes for the ports.

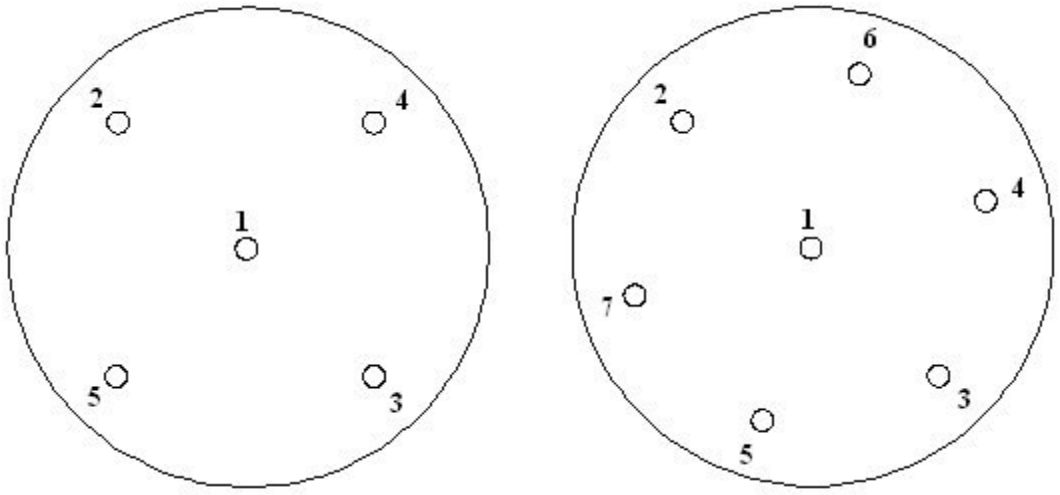

Fig. 5.10 Port numbering and arrangement: a) 5-hole, b) 7-hole.

The earlier method used an offset coefficient (C_δ) which was defined the same as the conventional definition for non-dimensional yaw-angle coefficient (C_β).

$$C_\delta = C_\beta = \frac{P_1 - P_p}{P_1 - P_{ave}} \tag{5.6}$$

where, P_1 = the center-port pressure,

P_p = any peripheral port pressure (P_2, P_3, etc.), and

P_{ave} = the average pressure of all peripheral ports

The horizontal offset was calculated by finding the yaw angle (β) at which C_δ was equal in diametrically opposite locations Φ_p and $180°+\Phi_p$ for each port p. A few comments on the main procedural differences in the earlier method are in order. Using the offset coefficient as C_β requires the use of all port pressures when only one port is needed. This leads to uncertainties being introduced from all five (or seven) pressure readings. If the actual ξ happens to be zero in a particular calibration set and the probe has been yawed to the correct horizontal offset, then the flow path (stagnation streamline) from the stagnation point to any port is the exact same in the two orientations and this coefficient can be expected to work well. But if ξ is not negligible, then ports in the vertical plane (Fig. 5.6), that are being used to calculate C_δ, introduce more errors. The method calculated offsets iteratively, but it corrected the calibration data for both offsets simultaneously in each iteration, which is not desirable as was observed when developing the new method (previous section). Furthermore, only a linear fit was used in the offset plot. This could be a source of error as amply demonstrated earlier. Lastly, the method finds the port location $\{\Theta_p, \Phi_p\}$ by simple averaging which can also be a minor source of error. Since probe reduction techniques have come a long way since this earlier method, the higher prediction accuracy of current-generation probes requires a commensurate offset angle correction.

The old method was applied to the same theoretical data used earlier and the results are compared in Table 5.3. Actual offset angles $\{\delta, \xi\}$ artificially set (four different cases) are shown in the first row. Offset predictions from the new algorithm have also been included (from Table 5.2) in the second row of Table 5.3 for quick reference. Row #3 has the predictions from the old method.

The earlier method performed poorly mainly in the horizontal offset prediction for our theoretical spherical-head probe. Its prediction was better in some respects for experimental 5- and 7-hole probes as is shown in the next section. These probes typically have conical-heads which might be a factor in the older method's performance. Based on

Table 5.3, however, the older method can be said to be inadequate for spherical-head probes.

Table 5.3. Predicted offset angles – comparison with an earlier method.

(δ, ξ) Actual	(0, 0)	(1, 0)	(0, 2)	(1, 2)
(δ, ξ) New method	(-0.07, -0.01)	(0. 95, 0. 00)	(0. 05, 1.89)	(1. 06, 1. 85)
(δ, ξ) Old method	(-1.11, 0.00)	(-0.08, 0.00)	(-1.00, 1.58)	(-0.00, 1.59)
(δ, ξ) Old (q_{dyn})	(0.43, 0.00)	(1.43, 0.00)	(0.35, 2.17)	(1.33, 2.13)

The denominator in equation (5.6) is an estimate of the flow dynamic pressure used simply to non-dimensionalize the pressures. Hence the old method was modified to have the actual dynamic pressure q_{dyn} (column #4 in Table 5.1) directly as the denominator and the results shown in row #4 of Table 5.3. This seemed to improve the predictions, but it was still poor compared to the new method. For the sake of completeness, various coefficient definitions similar to the one in equation (5.6), but with different numerators and denominators, were tried. These gave unreasonable results and are hence not shown here.

5.5 TESTS WITH EXPERIMENTAL DATA – 5- AND 7- HOLE PROBES

Calibration data of many multi-hole probes calibrated over the years at Aeroprobe Corporation's facility were available for our purposes (20 sets of 5-hole and 53 sets of 7-hole data). For any given probe data, offset angles were calculated with pressure data of each port (if it was within $\Theta_p = 35°$) separately. These calculated values were then averaged to obtain the final offset angles. The exact offsets for a given calibration data are not available for direct comparison with predicted results. The best indication of a good prediction is that the offset calculated from each of the ports compares well with the others. This also justifies the averaging of these offsets. This was the primary check in this section and the next when assessing the validity of the calculated values.

All the peripheral ports (2 through 5 for 5-hole; 2 through 7 for 7-hole) were used. The calculated offsets were compared with each other to see if they were fairly close and then averaged to get the final offset error of the probe calibration. The averaged offsets, calculated for a sample of two 5-hole probes, are shown in Table 5.4.

Table 5.4. Predicted offset angles – experimental 5- and 7-hole data.

Probe Name	Algorithm type	δ	ξ
5h-5C	New	-0.272	0.649
	Old	-0.969	0.598
5h-3C	New	-0.514	0.502
	Old	-0.896	0.662

The results from 7-hole probes were similar and are not shown here to avoid redundancy. For the 5-hole probes, the offsets were calculated using the old method (described in the previous section) also for comparison. The vertical offset predictions are comparable (within ±0.2°), while the horizontal offset predictions are off by about ±0.5° or more. To check if the difference in prediction was perhaps due to a difference in how the offset correction (of the calibration data) is implemented in the two codes, the corrected calibration files themselves were compared point-by-point. The corrected calibration files were different and each was consistent with its corresponding (predicted) offsets. In many data sets corrected with the earlier method, there was widespread mismatch in the offsets from different ports, further indicating that the earlier method is inadequate in terms of accuracy for current-generation high-accuracy probes.

The mismatch of offsets from different ports was seen in some cases with the new method also. Only about 75% of the many 7-hole probes conformed to this requirement. The percentage was smaller (about 60% of data sets tested) with 5-hole probes. The bad

prediction seems to be more prominent at high-speed calibrations (60m/s or higher). There might be a dependence on the tip-shape also, but this information was not readily available. Any "wobble" of the probe-tip gone unnoticed, if the probe does not spin true when it is rotated by the roll motor, is also a potential source of such errors. However, knowledge of any such occurrence was not available for most data sets and could not be cross-checked. Furthermore, much of the 5- and 7-hole data were dated (unlike the other two probes in the next section) and the calibration facility has undergone many changes recently. It is hoped that tests with future calibrations will help resolve the issue.

5.6 TESTS WITH EXPERIMENTAL DATA – 18- AND 12- HOLE PROBES

The port locations in these types of probes are shown in Fig. 5.11. Ports 13 through 18 for the 18-hole and ports 9 through 12 for the 12-hole are on the reverse side and hence not shown. For the 18-hole probe, only ports 1, 2 and 3 were used for calculating offsets, since they were the nearest at $\Theta_p = 35°$. Ports 4, 5 and 6 (at $\Theta_p = 55°$) were also tried. They gave reasonable results, but the errors were not low enough to encourage their use. In any case, three ports are quite sufficient for our purposes.

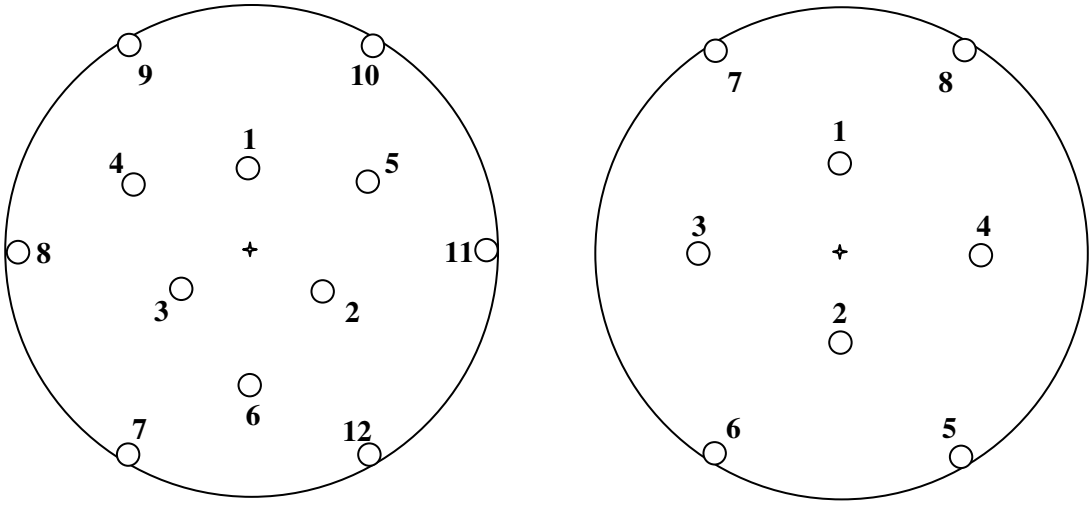

Fig. 5.11 Port numbering and arrangement: a) 18-hole, b) 12-hole.

For the 18-hole probes, of the 20 calibration sets tested, one sample result (of probe# D02-13-6) at Mach 0.16, which is representative of all, is analyzed here. As mentioned earlier, the horizontal offset is calculated iteratively until convergence. The iterations are necessary because the port location coordinates (and hence Φ_p) are changed in every iteration to account for the offset changes. Table 5.5 shows the horizontal offset (δ) calculations in each iteration from ports 1, 2 and 3.

Table 5.5. Predicted horizontal offset (δ) – experimental 18-hole data.

	δ (degrees)	**δ (degrees)**	**δ (degrees)**	**δ (degrees)**
Iteration #	1	2	3	4
Port #1	0.591	-0.192	0.008	-0.058
Port #2	0.622	-0.211	0.010	-0.046
Port #3	0.719	-0.108	0.108	0.056
Mean	0.644	-0.170	0.042	-0.016
Cumulative	0.644	0.473	0.516	**0.500**

δ values calculated from each port are very close to each other in each iteration. This validates our calculations. Since the calibration data is corrected in every iteration, the mean offset (absolute value) decreases from one iteration to the next. The cumulative offset is seen to oscillate before convergence. The final cumulative value is the horizontal offset error of the calibration data set.

The vertical offset (ξ) can now be calculated at one go using the method explained earlier. For this calibration data set, ξ was found to be 1.004° (Table 5.6). Here also, an excellent agreement between different ports is seen. Two of the data sets showed similar problems as earlier regarding mismatch of offset values and had the same characteristic bad surface-fits (while calculating C_δ) seen in most bad offset results. The source of this problem is as yet unknown, although the quality of calibration data is suspected.

Table 5.6. Predicted vertical offset (ξ) – experimental 18-hole data.

	ξ (degrees)
Port #1	1.051
Port #2	0.978
Port #3	0.983
Mean	1.004

The 12-hole probe uses only two ports (1 and 2 in Fig. 5.11b) to calculate the offsets. Since the 12-hole probe is a recent design undergoing prototype testing, only two sets of calibration data at Mach 0.05 and Mach 0.1 were available. The calculated δ values are shown in Table 5.7 for Mach 0.1 data. It needed only three iterations to converge. The vertical offsets from the two ports were 1.026° and 1.095°, giving a mean ξ offset of 1.061°.

Table 5.7. Predicted horizontal offset (δ) – experimental 12-hole data.

	δ (degrees)	**δ (degrees)**	**δ (degrees)**
Iteration #	1	2	3
Port #1	-0.656	-0.083	-0.017
Port #2	-0.680	-0.069	-0.001
Mean	-0.668	-0.076	-0.008
Cumulative	-0.668	-0.745	-0.754

The agreement between offset values from different ports corroborates the calculation and also indicates a good calibration data. This trend was observed in nearly all 18- and 12-hole probe data as expected. The algorithm's excellent performance with the spherical probes is a good validation of its worthiness.

5.7 RELIABILITY TESTS AND REFINEMENTS

Due to the lack of true offset angles for comparison (in experimental calibration data) and due to the sub-par performance with 5- and 7-hole probes, a battery of tests were undertaken to test the robustness and consistency of the offset-correction algorithm and identify shortcomings if any. All tests were done on a number of calibration data sets covering all types of probes and, unless explicitly mentioned as theoretical, were done on experimental data.

1) A check to see if the offset prediction has any dependence on the symmetry of arrangement of ports either in cone or in roll was done. This was achieved during our initial tests with theoretical data by changing the location of the ports arbitrarily by up to 10° in cone and/or roll. No dependence was found.

2) A perturbation of 0.5° in δ was introduced *after* the value had converged in the final iteration step. Over the next few iterations, the solution oscillated again and converged back to the initially predicted offset thus indicating a stable solution.

3) The calibration data sets were corrected in one shot, based on the *final* predicted vertical and horizontal offset values. This was to check if any error was introduced by progressively correcting the data over many iterations. No discrepancy was found. However, it is noted that the algorithm gives slightly better results if run a second time using the corrected calibration data from the first run.

4) A notable feature in the code is the use of a 3-D maximization routine to find the ports' angle coordinates $\{\Theta_p, \Phi_p\}$. This technique when compared to a simpler averaging technique (used in earlier methods) was found to reduce the errors in offset angles to some extent.

5) For a few calibration sets (probe# 5h-5c, 5h-3c, NASA_03), the calibration data was first corrected as usual for offset errors by the algorithm. Then, a 1° horizontal offset was introduced into the corrected data thus changing all the recorded Θ and Φ. Then the algorithm was run again with the changed data set. The offset (1°) was predicted back.

6) The range of Θ in the x-axis of offset plots (C_δ vs. Θ) was typically chosen as 4° to 10°. This gave good results for most cases. A few tests were conducted to see if the

calculated offsets were sensitive to this range. A similar test was done by trying different numbers of points for the local-least-squares (LLS) surface fitting routine. 35 points for Θ between 4° to 6° and 20 points for Θ between 6° to 10° was usually sufficient. δ and ξ varied within only ±0.1° over the different scenarios above.

7) The offset plots of a given calibration data, before and after offset correction, speak volumes for the correctness of the algorithm. If there are no offset errors in the calibration, the C_δ value should be continuous across the Θ=0, Φ=0 point. A sample 18-hole calibration data with a horizontal offset of 1° was chosen for illustration. Fig. 5.12a is an offset plot, but with a difference. The C_δ values for $\Phi=180°+\Phi_p$ have been plotted against the negative of the cone angle. Fig. 5.12b corresponds to the same calibration data after it has been corrected for offset errors. Notice how the two lines (top and bottom) align themselves after offset-correction thus indicating that the offset predicted was correct.

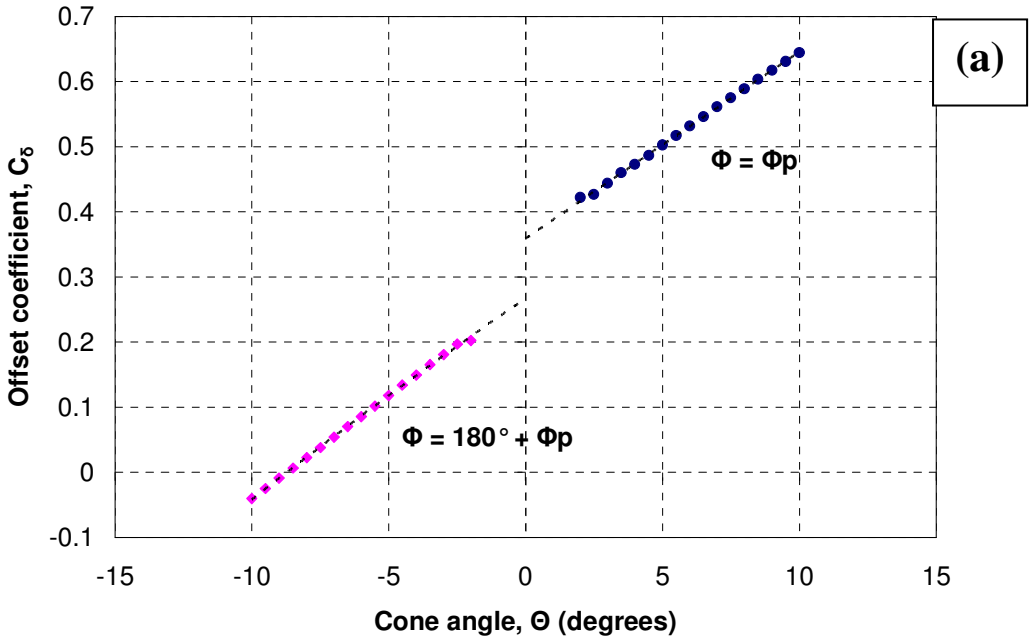

Fig. 5.12 Modified offset plot – a) before error correction, b) after error correction.

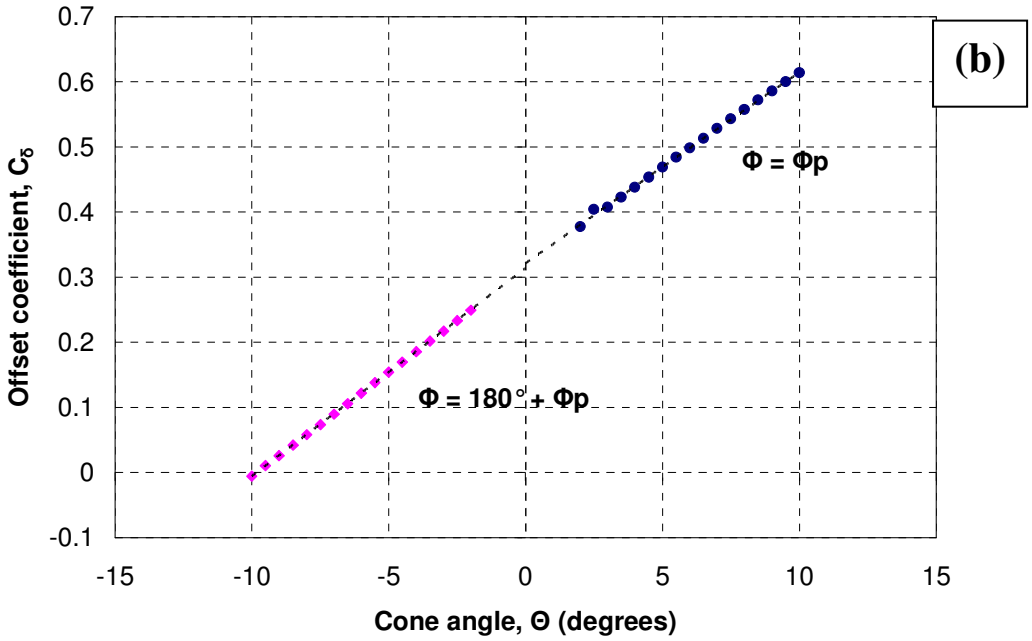

Fig. 5.12 (continued).

8) In order to ensure a good surface fit during LLS fitting, TableCurve-3D was used to inspect the nearest points returned by the search routine. Good surface-fits were a feature of all good offset calculations. Bad surface-fits were seen in some 5-hole calibrations (e.g. probe# GM_100C) which resulted in bad offset prediction. There is ample confidence in the reliability of the search routine and the LLS fitting scheme in the algorithm. Hence, the bad cases are probably a result of bad calibration data in some regions of the probe or unknown tip effects.

9) The algorithm speed was improved by trimming the calibration data (right at the start) to include data only within $\Theta = 30°$. This is because, although the offset errors affect the entire calibration data, its effect can be effectively gleaned from port pressures close to $\theta = 0$, $\Phi = 0$. All other data is extraneous to offset calculations.

10) There are two ways to find the nearest points for the LLS fit while calculating C_δ – the Euclidean distance between the cone-roll coordinates in Θ-Φ space or the direct angular separation (or central angle) between the data points in question. The latter, though it slows down the code, provided better accuracy.

6 ERROR CORRECTIONS IN SPECIFIC FLOW SCENARIOS

6.1 POINT VALIDATION

7-hole probes typically measure flows that are within 70°-75° with respect to the probe axis. If the flow happens to be beyond its working range, the probe fails to identify it. In other words, the probe could be facing the wrong direction and there is no way to know it. This can be a big disadvantage because, in such a situation, the probe data being measured would be used as proper or valid data, when ideally, the data should be marked as being beyond the probe's angular range and not used at all. The coordinate system for a straight 7-hole probe is the same as that for a spherical probe. The figure depicting the coordinate system is repeated here for quick reference (Fig 6.1). Note, however, that the probe head for a 7-hole probe is typically conical unlike what is shown.

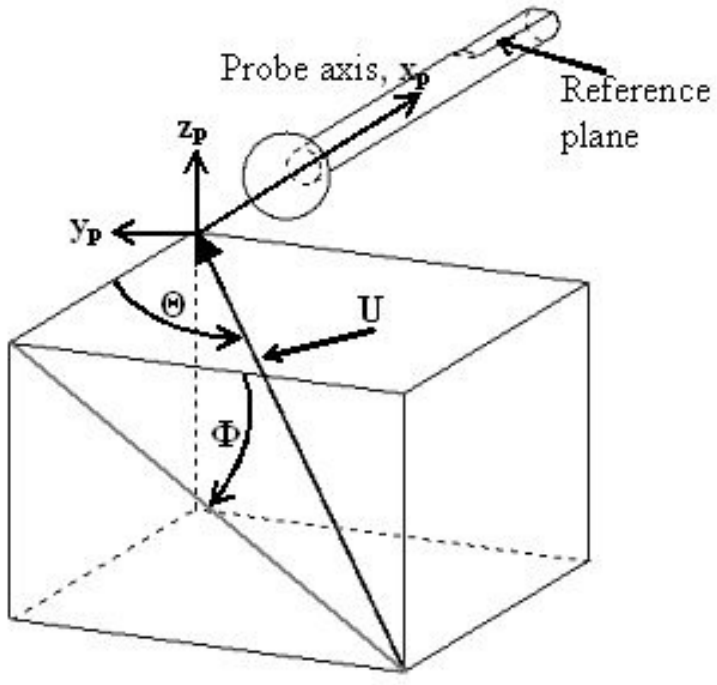

Fig. 6.1 Coordinate system of 7-hole probe.

To illustrate the point, an example of a case where the probe gives erroneous readout is analyzed here for a 7-hole probe. The actual stagnation point location in this example was at Θ_{test} = 115, Φ_{test} = 0 at a flow speed ($U_{mag\text{-}test}$) of 17 m/s. The probe calibration data is typically available only till about Θ = 75°. Since the reduction algorithm for the probe (Johansen and Rediniotis[15]) is unaware that the flow is beyond its range, it will use the pressure data from its seven ports and solve for flow speed and direction using the probe calibration data as usual. The flow prediction results for this case were found to be Θ_{pred} = 52, Φ_{pred} = -31 and $U_{mag\text{-}test}$ = 13. As can be seen, a highly erroneous reading has been taken by the probe without any warning to the experimenter. This type of erroneous predictions was seen for many stagnation point locations in the range of $\Theta > 75°$.

Before a technique or criterion is developed to identify the above occurrence, it is necessary to define, for a given 7-hole probe, its angular "range". This is done by observing how the prediction errors for Θ, Φ and U_{mag} deteriorate as the stagnation point location (Θ_{test}) is increased for the probe. If the errors go beyond an acceptable error band (set by the experimenter) at some Θ, that Θ would be called the range of the probe. The range thus obtained will of course depend on the chosen error band. It should be noted that, for most good reduction algorithms (and reasonable error bands), this dependence is seen only for $\Theta \sim 65°$ to $\Theta \sim 75°$. Beyond an angle of, say, 80°, the errors become so high that the prediction capability of the probe can be said to have broken down completely. Further, the range can vary from probe to probe even if the error bands were set the same. Our first goal, hence, is to define an error band and find the range of a given probe.

To this end, a 7-hole probe (# D04-32-1) was calibrated up to 153° in Θ. Test data for different angular limits were obtained directly from the calibration data. In other words, a test data for the probe up to, say, 60° would comprise of all points up to 60° in the calibration data itself. Four sets of test data were thus obtained corresponding to Θ limits of 65, 67.5, 70 and 75. A standard reduction algorithm was used to compute the flow

properties for each test data set. In each case, the predicted flow properties were then compared to the "true" value from the calibration data and the standard deviation of the errors calculated. The standard deviations of the errors in cone (Θ), roll (Φ) and U_{mag} were then plotted in Fig. 6.2. The mean errors for all sets were nearly zero and are not considered here. As is evident from the graph, the prediction errors take a steep upward turn at around $\Theta_{range} = 70$. Hence the range of the probe can be set as 70° beyond which prediction accuracy of flow variables become unacceptable. Now that the range of the probe is known, a technique can be developed to identify stagnation points beyond this range.

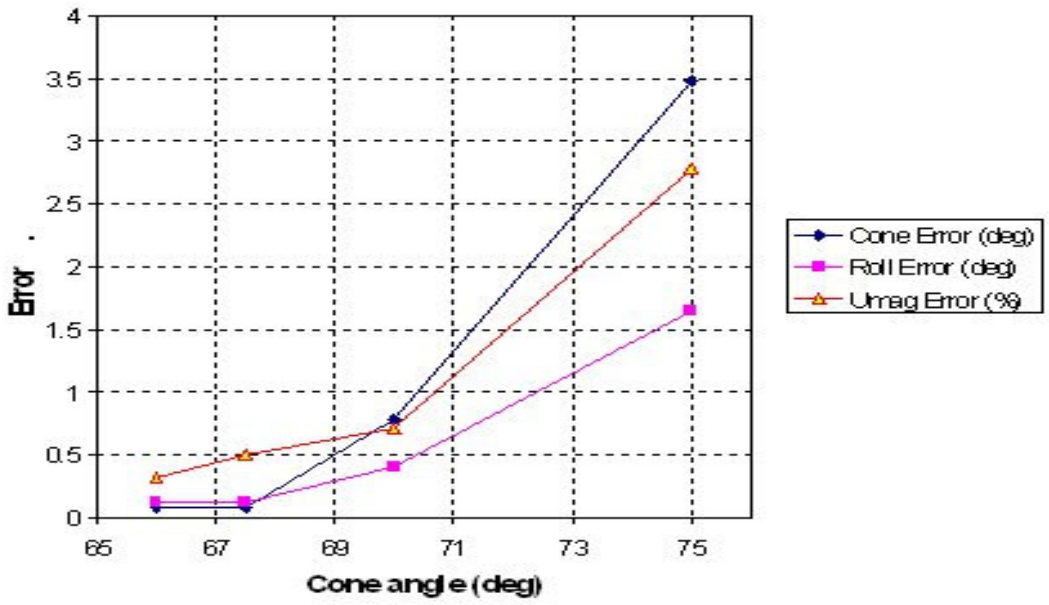

Fig. 6.2 Errors in predicted flow properties from calibration data up to different cone angles.

For a probe employed in a flow study, only the pressure data (from its ports) is available. Any method to identify invalid points beyond its range must hence use only some combination of these pressures. Many such combinations are popularly used in most multi-hole probe reduction algorithms as non-dimensional coefficients. These coefficients (collectively called C in equation (6.1)) follow a desired pattern:

$$C = \frac{x1 - x2}{x3 - x4} \tag{6.1}$$

where x1, x2, x3, x4 are port pressures or some linear combination of them. The coefficients are defined thus for two good reasons:

1) The difference of pressures eliminates any dependence of the coefficient on the reference pressure of the readings. This also means that, for incompressible flows, the dependence on the flow static pressure is eliminated.

2) The denominator is typically an estimate of the freestream dynamic pressure (q_{dyn}). Thus, apart from non-dimensionalizing the coefficient, the division helps to reduce the dependence on q_{dyn}. Hence, the coefficient becomes acceptable for a wide range of Reynolds numbers (or Mach numbers) the probe might encounter.

Following this lead, if a coefficient that behaves in a marked way as the flow rolls over at the range limit of the probe can be defined, that coefficient can be used to check the validity of a data point. It is desirable for this coefficient, hereby called the cut-off coefficient C_x, to have the following properties to identify the roll over:

1) monotonically increase/decrease within the range (Θ_{range}) of the probe,

2) noticeably jump in its value at or near the range

3) continue to monotonically increase/decrease after Θ_{range}.

The second condition will identify the roll over. The first and third conditions ensure that there is no overlap of C_x values on either side of Θ_{range} i.e., C_x value of a valid point does not match that of an invalid point beyond the probe's range.

Using the form prescribed in equation 6.1, a multitude of choices exist for x1…x4 and it is inelegant to try any and all of these hoping to chance upon a good definition for C_x that satisfies the three conditions above. Therefore, it is prudent at this point to look at the behavior of the port pressures at very high angles of attack and hopefully extract some information (or constraints) that will narrow down our choices. Consider a 7-hole probe in a flow field of velocity vector **U** at an angle of Θ_{test} as shown in Fig. 6.3 (front and side views). The stagnation point is at a cone angle Θ_{test} which is beyond the range

of the probe (Θ_{range}). The small deviation of the stagnation from Θ_{test} (due to bending of streamlines) in actual flows has been ignored. For our analysis the ports have been named as shown. P_{max}, as the name suggests, is the pressure of the highest port i.e., the port nearest to the stagnation point. P_{side1} and P_{side2} are the peripheral ports adjacent to it. P_{opp} is the port directly opposite to it. The other port names are self-explanatory.

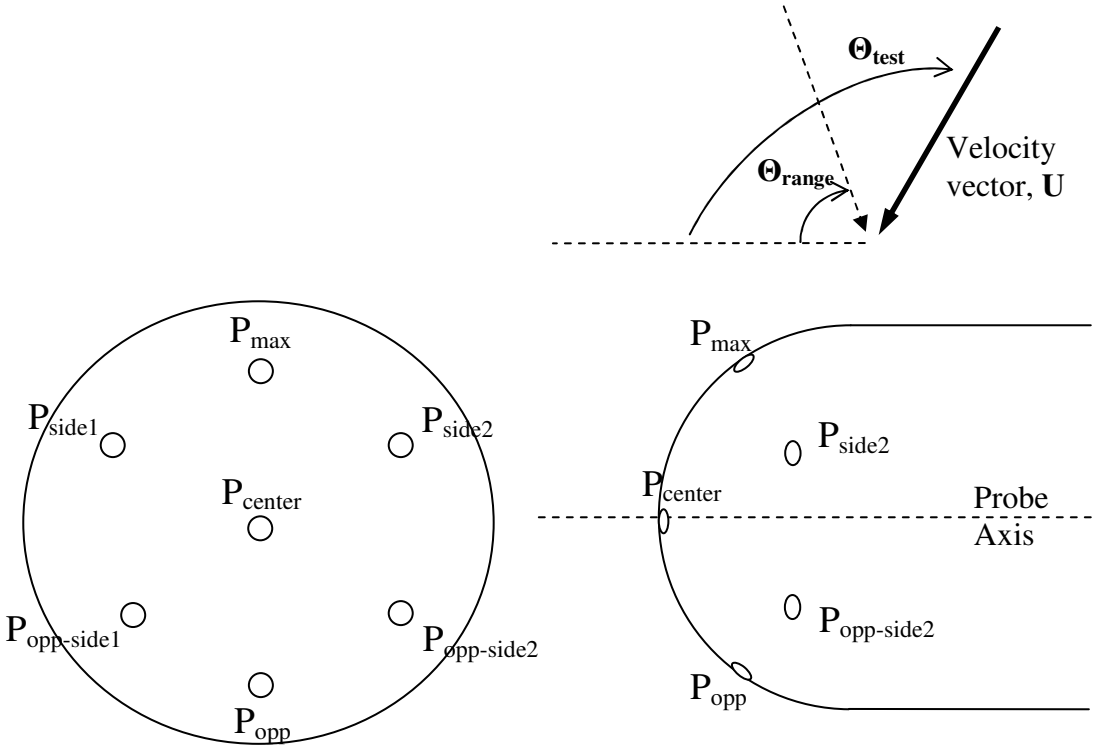

Fig. 6.3 Port designation based on maximum pressure port.

Since there are four unknowns (Θ, Φ, U and P_s) to be calculated by the probe, four pressure ports (nearest to the stagnation point) are used by the reduction algorithm at any one measurement (test) point. For our case above, the ports P_{max}, P_{side1}, P_{side2} and P_{center} can be used provided they are all in attached flow. At high angles of attack, say even at $\Theta_{test} > 40°$, the ports at the bottom of Fig. 6.3, namely, $P_{opp\text{-}side1}$, $P_{opp\text{-}side2}$ and P_{opp}, are already stalled. For higher angles, the reduction algorithm is likely to fail when the center port is also in the stalled (separated) region. Hence, the stalling of the center probe

is a likely indicator of the range limit of the probe. It is a known fact that the pressures from all stalled ports are roughly the same. Hence, the cut off coefficient (C_x) should be able to capture the angle at which P_{center} becomes equal to the other three already-stalled ports.

Thus, the different possibilities for C_x have presently been narrowed down. Based on this new constraint, many different definitions for C_x were tried and the final one that worked best is defined below.

$$C_x = \frac{P_{max} - P_{center}}{P_{max} - \left(\frac{P_{opp-side1} + P_{opp-side2}}{2} \right)} \tag{6.2}$$

As can be seen, near the range limit of the probe, P_{center} will match the already-separated P_{opp1} and P_{opp2}, making C_x approach unity. This C_x was plotted as a 3-D surface against the angle coordinates Θ and Φ to study its behavior and is shown in Fig. 6.4. This plot is confined to all points in the calibration data which had the same peripheral port as P_{max}. In other words, this plot looks similar regardless of which peripheral port was chosen as P_{max}.

Fig. 6.4 shows a distinct jump in C_x in the 72°-75° region. An important feature of this surface is that the surface is nearly planar and well-behaved. A common problem with other C_x definitions (not shown in this work) was that, even if the monotonic change and the jump were present, points near the ends of the surface (i.e., near Φ=120° and Φ=180° in Fig. 6.4) were very high or very low when compared to the rest of the surface and hence untenable. Due to planarity and near-independence from Φ, the C_x plot is shown as a 2D plot (up to Θ = 115°) in Fig. 6.5 for further analysis.

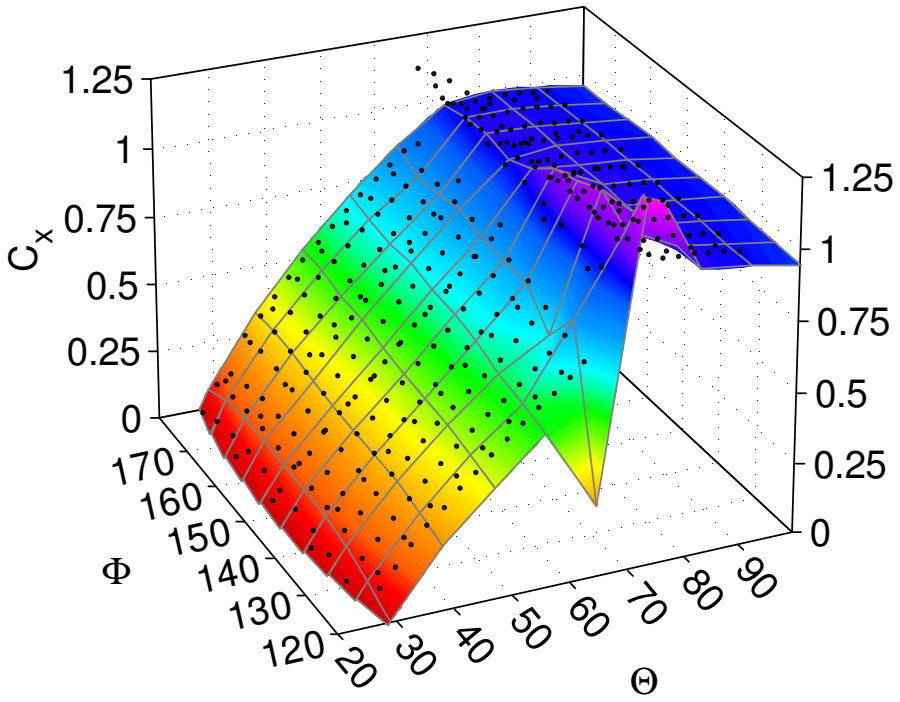

Fig. 6.4 Typical cut-off coefficient (C_x) for a 7-hole probe: 3D plot.

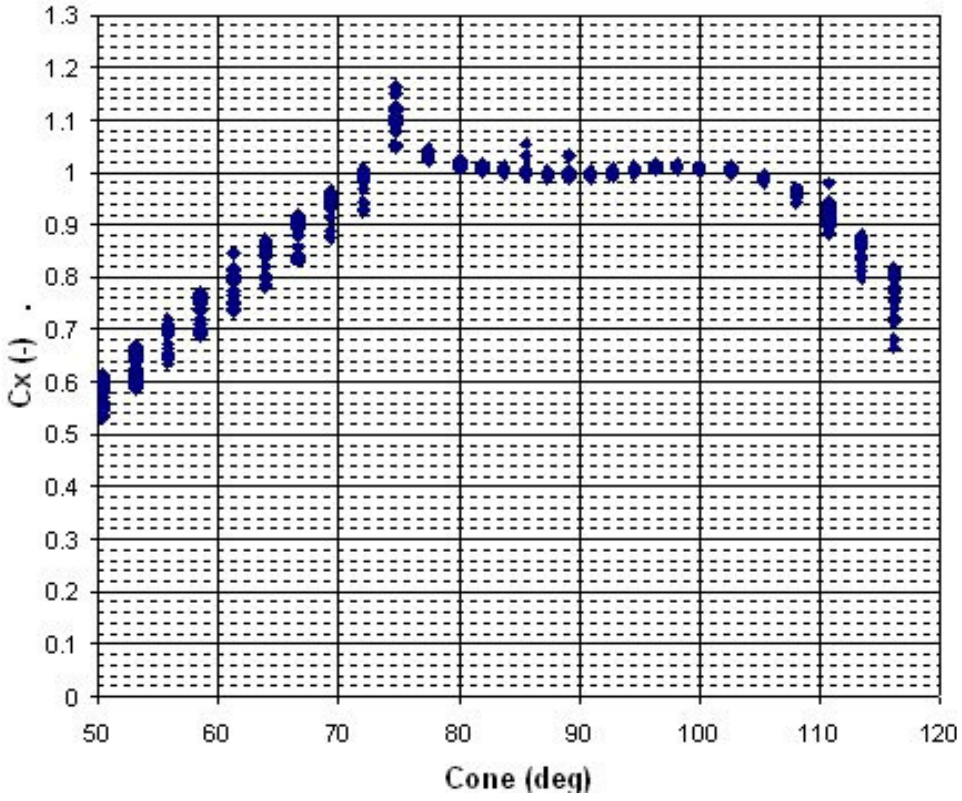

Fig. 6.5 Cut-off coefficient (C_x): 2D plot – probe #1.

The range of the probe being analyzed is 72°. The goal is to define a threshold value for C_x, such that all data above this threshold can be identified as beyond the probe's range. By inspection, if a threshold value of 0.96 is used, all data beyond 70.0° can be removed. This, however, results in a loss of 2° in the viable range of the probe. Further, the behavior of C_x is as desired until about 110°, after which it decreases and overlaps with "valid" C_x values within the probe's range. Hence, the threshold value holds up only if the flow is known to be within 110°. This is still useful in many flow situations where the uncertainty in the flow direction is not more than 30° beyond the range limit of the probe.

The entire analysis was repeated for another probe (#D05-28-1) which was calibrated up to 90°. The C_x plot for this probe is shown in Fig. 6.6.

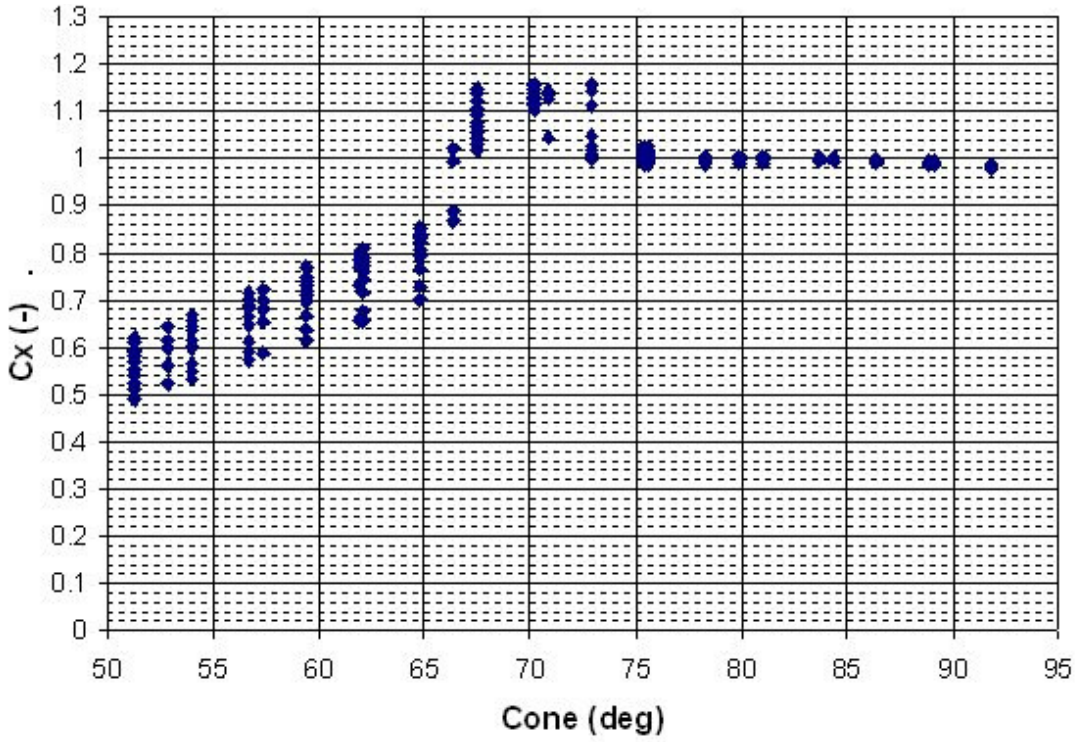

Fig. 6.6 Cut-off coefficient (Cx): 2D plot – probe #2.

The range of the probe was determined as 67.5° using the method described earlier. The threshold value obtained from the plot in this case is 0.90. This also indicates that the C_x threshold value for each probe has to be found individually.

To summarize, when the probe is being used in a flow study, at every test point, C_x is calculated. If this value is beyond the probe's C_x threshold value, the data point is flagged as being beyond the range and not used.

6.2 STEP RESPONSE OF PRESSURE TUBING

The pressure tubing from the port (at the probe surface) to the pressure sensor (in the probe body) can cause attenuation and phase lag in the measured port pressures. The pressure tubing assembly can involve multiple cylindrical tubes of varying diameters and lengths. The transducer (or pressure sensor) cavity volume at the end of the tubing assembly also effects the tubing frequency response. The transfer function, which is a combination of the amplitude ratio and the phase lag, can be found either by theory (Bergh and Tijdeman[29]) or by experiment in an acoustic calibration facility.

A two-speaker acoustic calibration facility is employed in calculating the frequency response of tubing in the frequency range of 0 Hz to 3000 Hz. The data acquisition was upgraded to perform multiple acoustic calibrations simultaneously and the resultant GUI is shown in Fig. 6.7. Frequency response (pressure ratio and phase) of up to three sensors, based on the time-traces of the input and output sinusoidal signals, can be measured at the same time. A Fast-Fourier-Transform (FFT) of the time-trace keeps track of all signals' frequencies. Over the years, the facility has been validated many times by comparing experimental results with theoretical results (using Bergh and Tijdeman[29]). Hence, for the step response analysis of tubing assemblies in this section, only theoretical calculations of frequency response are performed with the knowledge that an experimental validation can be achieved if needed.

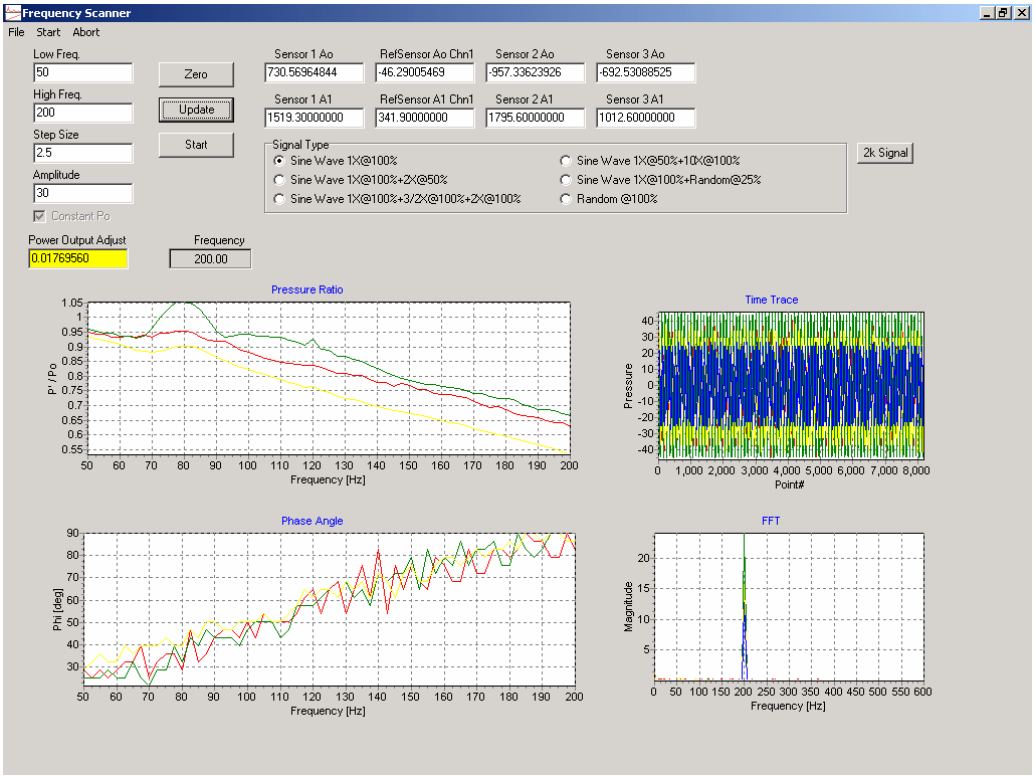

Fig. 6.7 GUI for the acoustic calibration facility: simultaneous calibration of up to three tubes.

Two general test cases (underdamped and overdamped) were studied. The frequency response in each case was obtained in terms of the amplitude ratio (magnitude) and the phase shift. From this, the transfer function was obtained using an algorithm implemented in Matlab. The order of the transfer function, as derived by Matlab's inbuilt routines, is user-specified depending on what order of the model is desired. This transfer function's response to a unit step input at t = 0 was then studied (also using Matlab's inbuilt routines). The entire code is listed in Appendix C.

Case 1: L1 = 10mm, D1 = 5mm, L2 = 80mm, D2 = 2mm

The amplitude ratio and phase lag up to 1000 Hz is shown in Figs. 6.8 and 6.9, respectively.

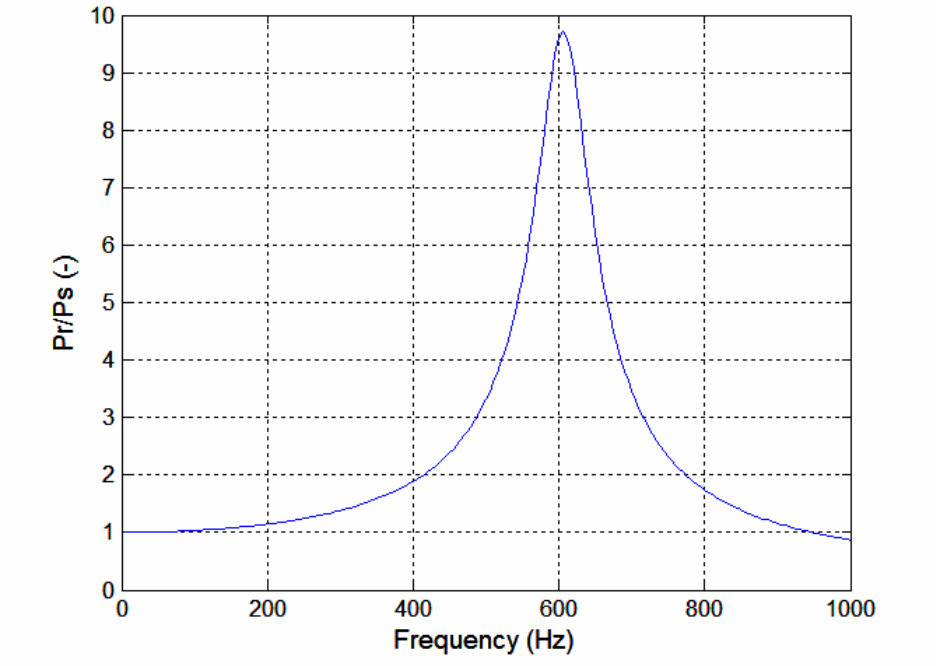

Fig. 6.8 Case 1: Amplitude ratio.

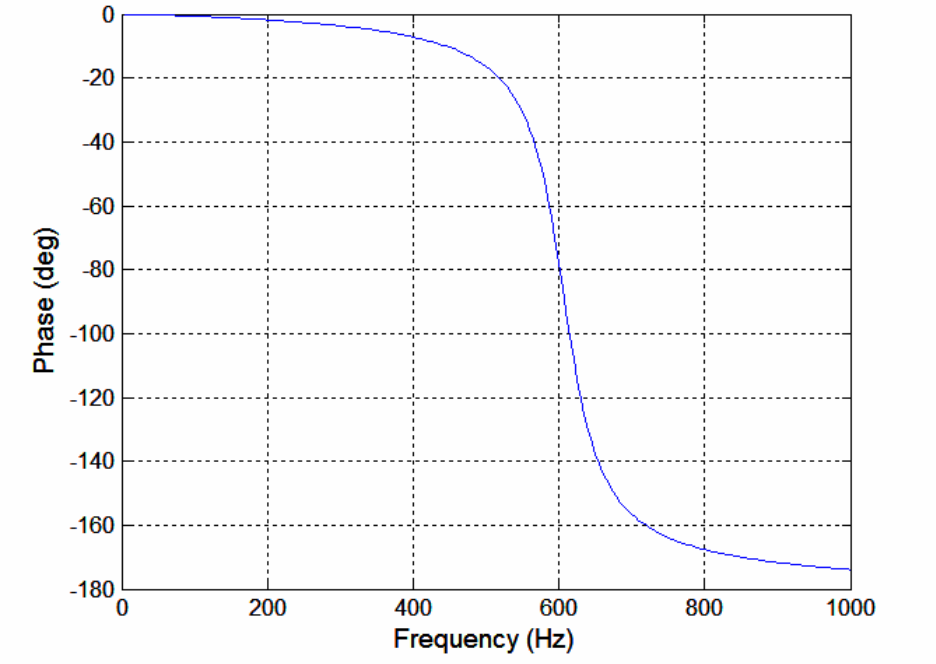

Fig. 6.9 Case 1: Phase shift.

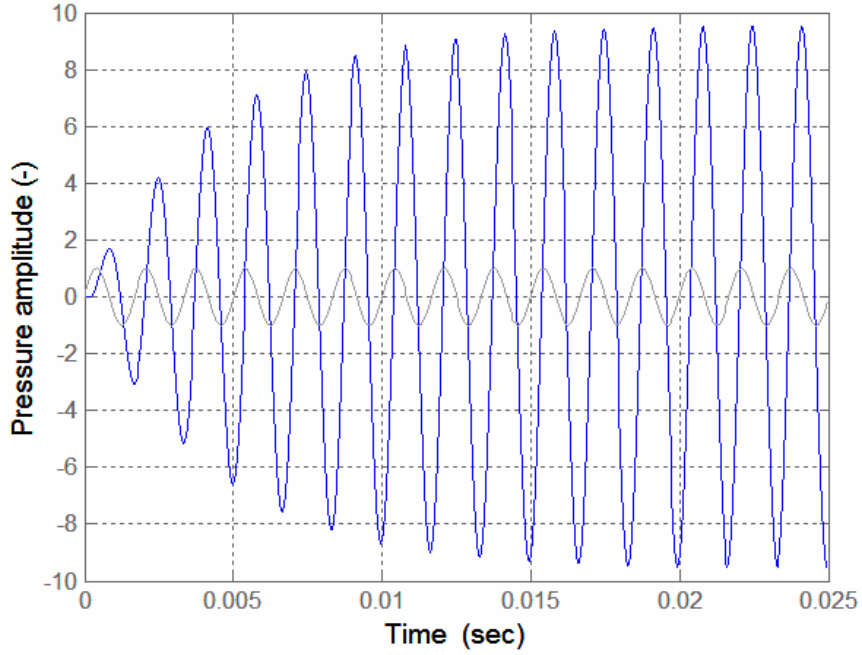

Fig. 6.10 Case 1: Output corresponding to unit sine input at 600Hz.

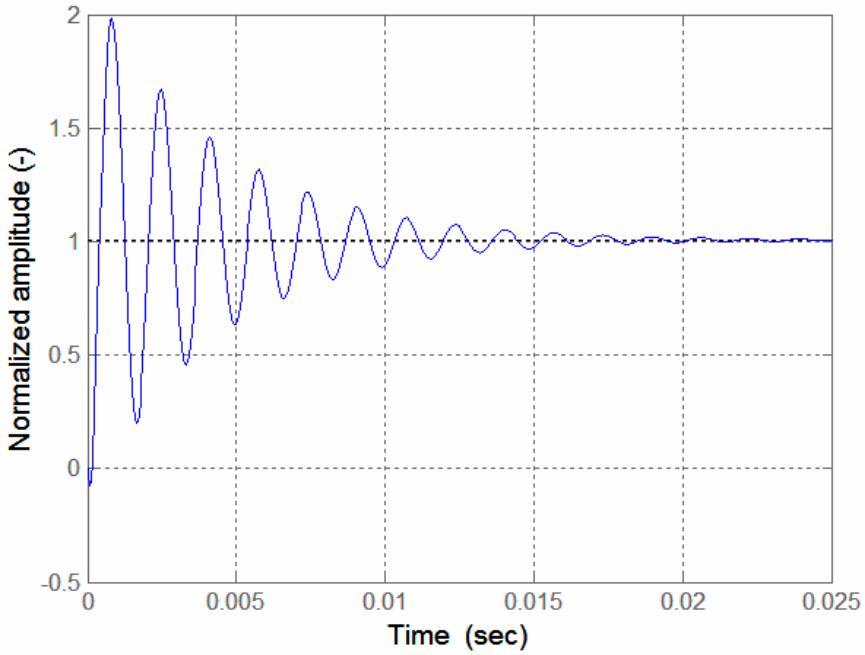

Fig. 6.11 Case 1: Step response.

The transfer function for the system is computed. The correctness of the transfer function is tested by using a sample sinusoidal signal of 600 Hz and unit amplitude as the input. From frequency curves (Figs. 6.8 and 6.9) the output should have the output amplified by 9.5 and a phase lag of 80°. This is confirmed as shown in Fig. 6.10, which is the output for the above input (unit amplitude sinusoidal at 600Hz) from the computed transfer function.

This is a short stocky tube expected to be an underdamped system. The step response of the transfer function to a unit input is plotted in Fig. 6.11. The output oscillates before it converges to the unit input amplitude thus indicating an underdamped system.

Case 2: L = 150mm, D = 0.25mm

The amplitude ratio and phase lag up to 1000 Hz for this case is shown in Figs. 6.12 and 6.13, respectively. The transfer function for the system is computed. The correctness of the transfer function is tested again for this system also. A sample sinusoidal signal of 800 Hz and unit amplitude as the input is shown as a grey line in Fig. 6.14. From frequency curves (Figs. 6.12 and 6.13) the output should have the output reduced to 0.35 of the input with a phase lag of 185°. This is confirmed in Fig. 6.14 as shown by the blue line, which is the output for the above input from the computed transfer function.

This is a long thin tube expected to be an overdamped system. The step response of the transfer function to a unit input is plotted in Fig. 6.15. The output does not oscillate or overshoot before it converges to the unit input amplitude, thus indicating an overdamped system.

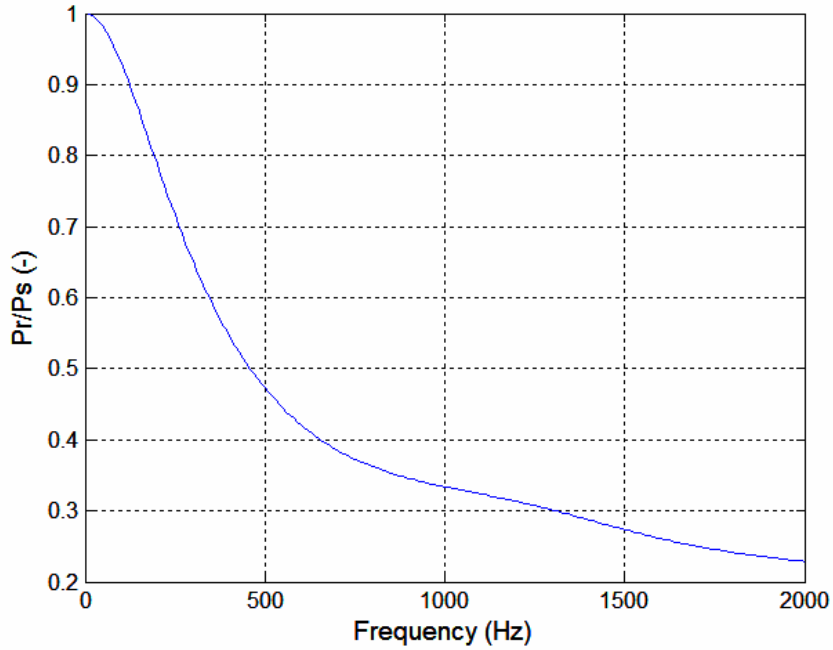

Fig. 6.12 Case 2: Amplitude ratio

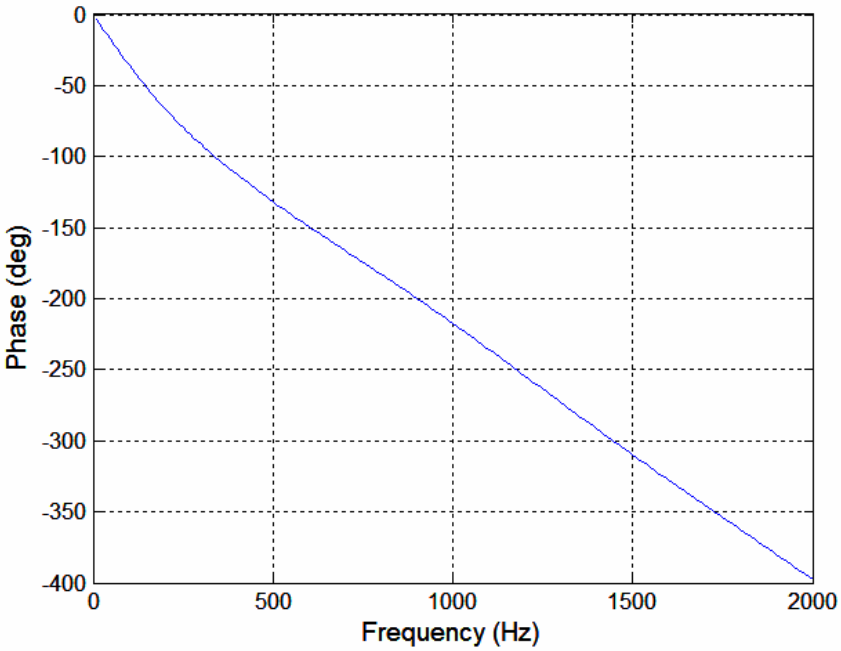

Fig. 6.13 Case 2: Phase shift.

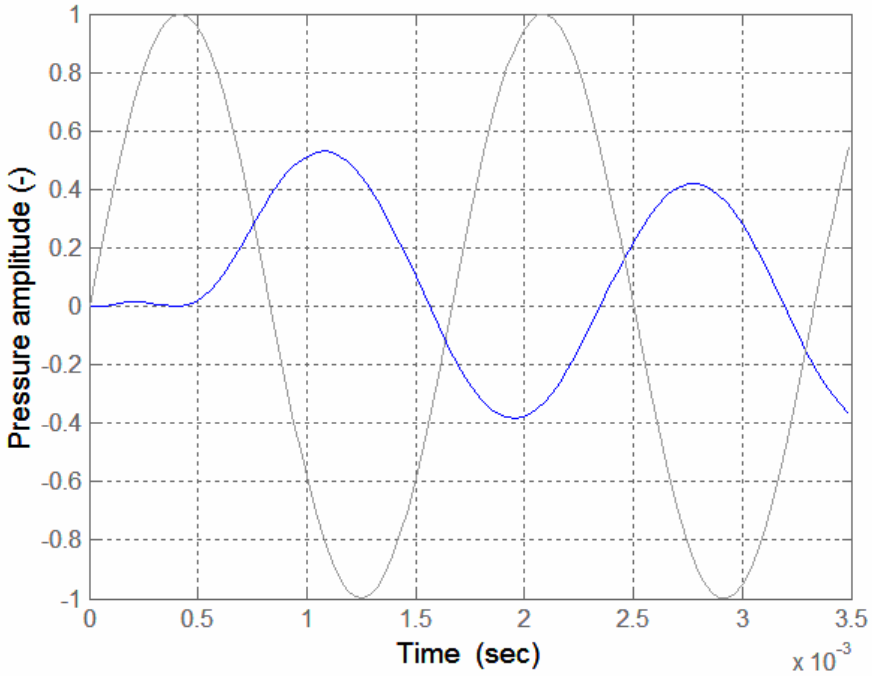

Fig. 6.14 Case 2: Output corresponding to unit sine input at 800Hz.

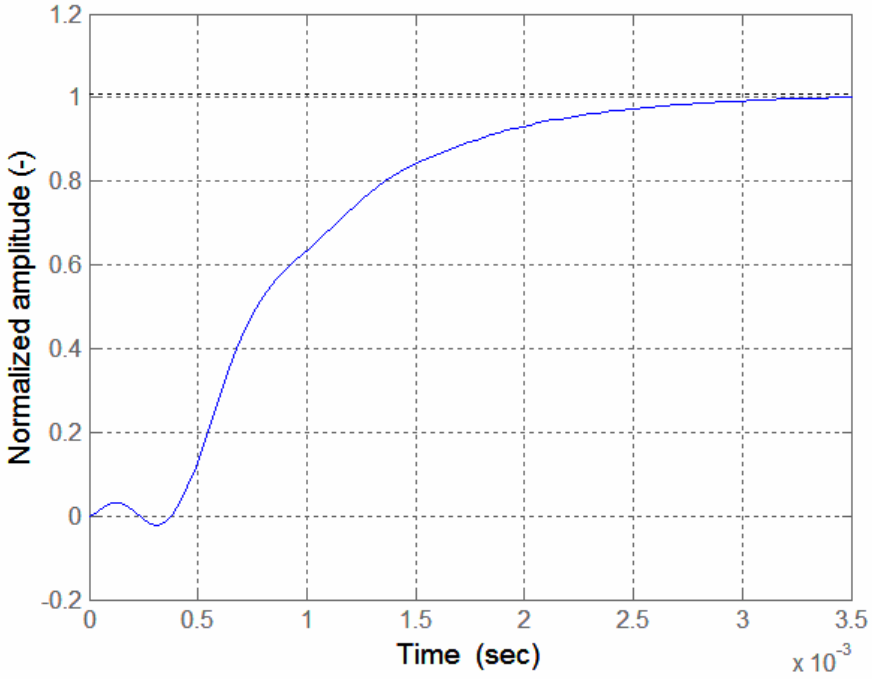

Fig. 6.15 Case 2: Step response.

The step response of the system completely characterizes the system. In real flows, the pressure is measured at the end of the tube i.e., near the sensor. The actual pressure at the probe's port (i.e., at the probe's surface) can now be reconstructed from the transfer function of the tubing system.

A more complicated input pressure signal was generated and the output pressure signal was calculated (based on the transfer function) for the second case and is shown in Fig. 6.16. The synthetic input signal was a combination of a polynomial curve, a constant stretch and multiple sines.

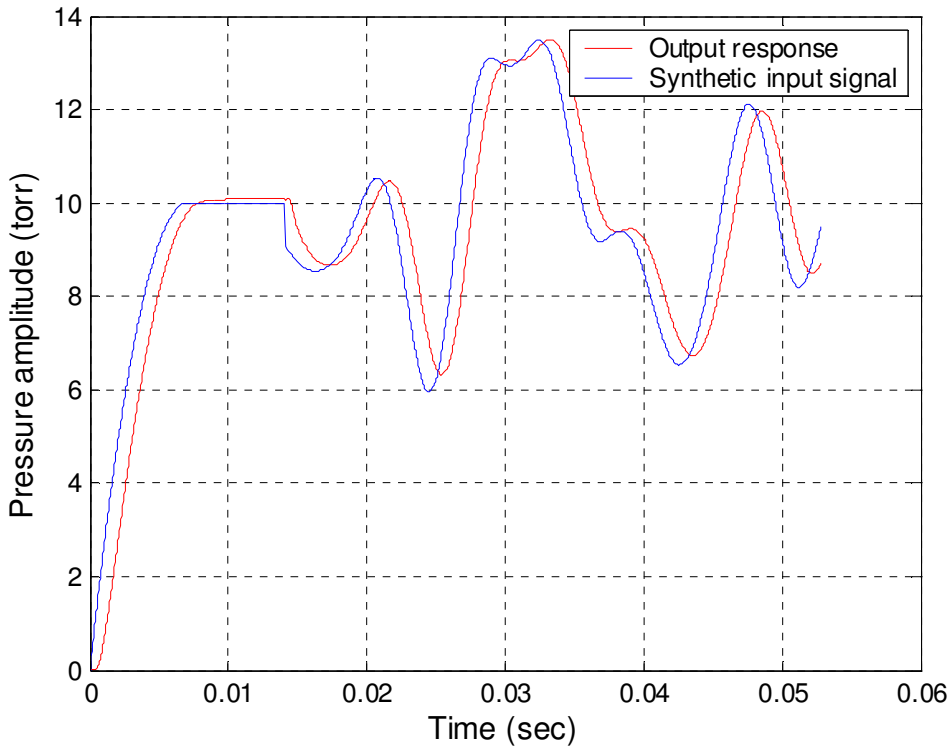

Fig. 6.16 Case 2: Out put response to a synthetic input pressure signal.

6.3 PORT REDUNDANCY AND BLOCKAGE

If one of the ports is discovered as a bad sensor, a new port (not present in the original sector) has to be chosen and the reduction repeated with the resulting new sector. This

can be done, however, only if the new port is available within a reasonable angle from the stagnation point (preferably within ~85°). Since a redundant back-up port was not part of the original design, the availability of a fifth port was checked for all stagnation points within ±45° from the horizontal. For the Weatherprobe, the highest angle a fourth-highest port can reach in any sector is 81.1°. The highest angle for the fifth-highest port is 82.8°. (Aside: The lower extremes of these two angles are 46.0° and 56.5° respectively.) The coordinates of the ports as obtained from calibration data was used in the above calculations so as to avoid errors due to machining imperfections. As a side note, it is observed that the values for the above two angles for the 12-hole omni-directional probe (section 2) are 81.3° and 91.7°, respectively. Hence, there is always a redundant port available for any sector in the Weatherprobe (although, this is not the case for the 12-hole probe). Hence, in case of blockage of one of the ports in the sector, the blocked port can be replaced (in the reduction scheme) with the extra port and the reduction performed using calibration coefficients of the resultant new sector. A blockage in a 12-hole probe, however, can be corrected only by removing the probe from the setup and manually cleaning the pressure tubing by blowing compressed air through it.

This leaves us with the question of how to identify a port that has been blocked (by debris in the flow field) purely by analyzing the pressure data. An easy way to check if a port is blocked is to find the standard deviations of the pressure signal for all the highest ports. If one of the ports is blocked, the standard deviation would be very small (of the order of the sensor signal noise). This is because the volume behind the blockage would not change and the temperature will be fairly constant over short periods – i.e., the pressure, as seen by the sensor, will be fairly constant. Thus, if the frequency spectrum of the pressure data is taken and the amplitudes at higher frequencies (short period) analyzed, the results can be used to indicate a blocked port. The limitation of short period data is required to avoid any effects due to ambient temperature (hence pressure) changes. Data at 100Hz for 3 to 4 seconds is considered sufficient for this check.

Further, the amplitudes (or standard deviations) of the port in question must be compared with that of other ports to ensure that it is not a no-flow case. The following error parameter (ε_i) for each port "i" is suggested:

$$\varepsilon_i = \frac{\sigma_i}{\sqrt{\sum_{i=1}^{5}(\sigma_i)^2}} \tag{6.3}$$

If ε_i is smaller than a specific value (that depends on the pressure sensor), then the port can be deemed to be blocked. This value depends on the noise characteristics of the sensor and can be found experimentally.

Another rigorous method to find a blocked port is through the reduction algorithm. Since, for any stagnation point, there is an extra valid port available, there are five ($5C_4$) different combinations of the ports that can be used to define the sector. Any one of the five sectors can be used in the reduction algorithm to calculate the flow quantities and get the same solution (within a reasonable error margin). Therefore, for every test point in an unknown flow field, the pressure data can be reduced using five different sectors and it can be checked if all five solutions are comparable. A mismatch (typically all five will be dissimilar) would indicate a blocked port.

Consider the variation of C_p (non-dimensional coefficient of pressure) for a typical port obtained from calibration data shown in Fig. 6.17. The scatter in the data is due to surface imperfections and sensor errors. Only the general trend of the curve is of concern here. Five different solutions for the stagnation point from five different sectors are available, namely, ($\Theta_{calc\text{-}i}$, $\Phi_{calc\text{-}i}$, $U_{calc\text{-}i}$) (i = 1...5) of which only one is correct. Now, the coordinate location of all the ports is a known quantity. Hence, the angle of the stagnation point from each of the five ports (j = 1…5) for each case "i" can be found. From the graph above an approximate $C_{p\text{-}ij}$ could be found and hence an approximate port pressure $p_{ij} = C_{p\text{-}ij}1/2*\rho* U_{calc\text{-}i}{}^2$ can be calculated. For the "i" corresponding to the correct solution (i = c) there will be a reasonable agreement between the p_{cj} (j = 1…5)

and the measured pressure data. The port that is not part of this sector “c” is the blocked port.

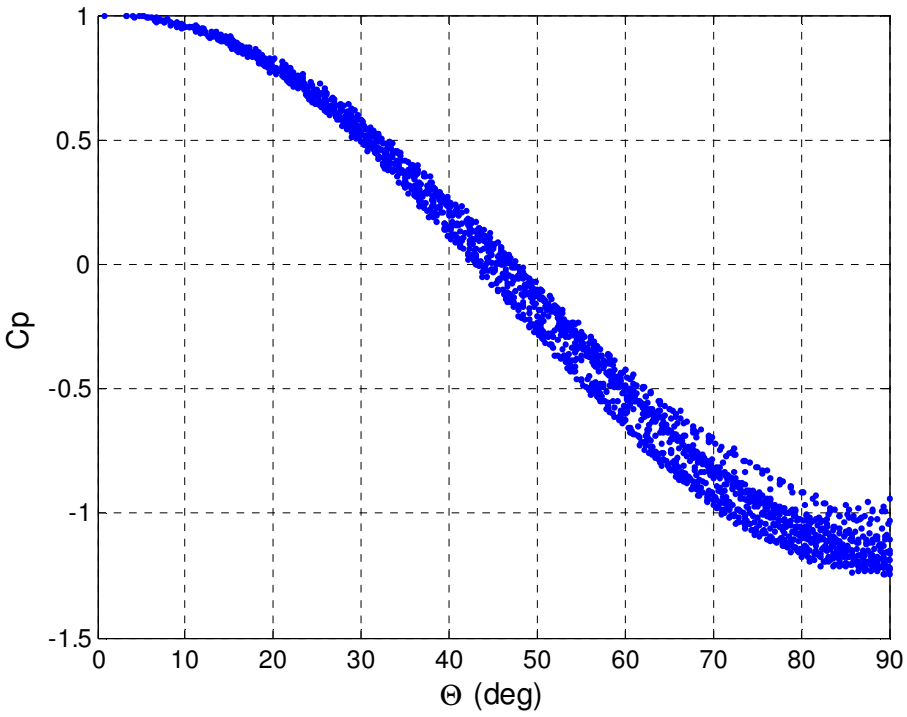

Fig. 6.17 Typical C_p variation from Weatherprobe’s calibration data.

This port can be flagged and kept unused for all subsequent reductions until a maintenance visit to the probe to clear the blockage. Good readings can be obtained until the port is cleaned. However, a second blockage in the neighborhood of the first cannot be detected and will affect the readings. Hence the probe should be cleaned as soon as the first one is detected. It is prudent at this point to note that, if the static pressure of the flow field is known, the required number of pressure ports for the reduction algorithm goes down by one i.e., to three. The atmospheric pressure (as obtained from a barometer) is a good estimate of the static pressure in wind speed measurements. In such a case, a double redundancy in port availability can be achieved in the event of blockage.

Purging system to remove contaminants in pneumatic lines

Two purging systems were designed to remove contaminants and condensates from Weatherprobe's pneumatic lines and are described here. The pros and cons of each are also explored. The design can be implemented in future versions of the prototype.

Design 1: Scanivalve Corporation's 'off-the-shelf' purge valve (Fig. 6.18) which uses eight independent pneumatic-controlled valves inside that work in tandem. In RUN mode, all pressure inputs (top surface of Fig. 6.18) are directly connected to the pressure sensors (bottom surface of Fig. 6.18). In CAL mode (Fig. 6.18), the sensors are isolated from the pressure inputs and then connected to a calibration pressure (side surface in Fig. 6.18). In purge mode, the sensors stay isolated and the purge supply pressure (side surface in Fig. 6.18) is brought in line with the input ports. The different modes (run, cal and purge) of the valve are set by applying 90-120 psi to SWITCH-1, SWITCH-2 and SWITCH-3 ports (side surface in Fig. 6.18) in that sequence (Fig. 6.18). First SWITCH-1 is charged and the sensors isolated. Then, the SWITCH-2 is charged and the sensors brought in line with the calibration manifold supply. Next step is, and this is very important to safeguard the sensors, to pause for at least 5-15 seconds before SWITCH-3 is charged to engage the purge mode. This is necessary to ensure that complete isolation of ports was achieved after SWITCH-1. Now, the calibration of the ports (or zeroing) and purging can be performed simultaneously. In order to switch back to RUN mode, a reverse sequence to the above is followed. Purge mode is turned off by SWITCH-3. Again, a pause is needed for 15 seconds to bleed out any residual pressure in the lines. The CAL mode is turned off using SWITCH-2 and finally the sensors are brought back in line with the pressure input lines using SWITCH-1.

The three control ports in turn are controlled by a system of solenoid valves all assembled in a single module (model MSCP3200 from Scanivalve Corporation). This module has three individual control voltage inputs for SWITCH-1, SWITCH-2 and

SWITCH-3 and a single 90-120 psi pressure line input. The pressure line splits into three (one each for SWITCH-1, SWITCH-2 and SWITCH-3) through an internal 4-way solenoid valve controlled by the input voltages. With three separate 5V analog outputs directly from the Data acquisition (Daq) board, in the proper sequence and with proper timing (described earlier), the purge valve can be switched from run mode to purge (and cal) mode and back.

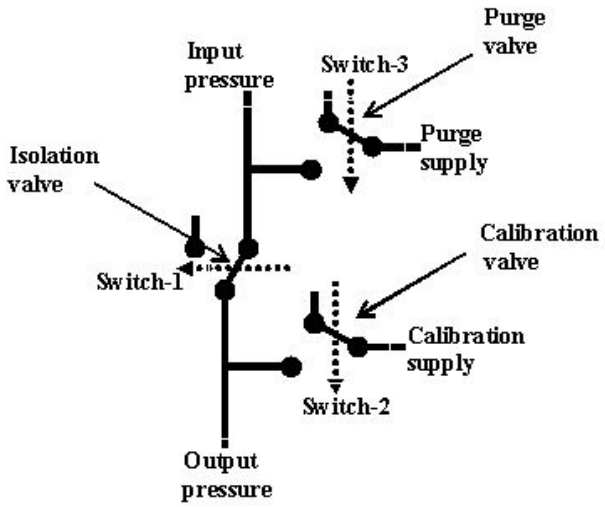

Fig. 6.18 Purge valve: internal plumbing (Courtesy: Scanivalve Corporation).

For our probe, since there are twelve pressure sensors, two purge valves will have to be used (custom design was not available). The additional ports can be sealed off. The purge valves (2.7in. x 2.6in. x 1.5in. in dimension) can be installed inside the spherical head of the probe (to minimize pressure attenuation), but with some modifications to the internal arrangement of sensors and wires. However, only a single control module (MSCP3200, 2.75in. x 1.25in. x 1.20in.) is needed and this can be installed within the enclosure next to the data acquisition system. Another control valve, ENETCPM, by the same company, has the exact same functionality and is much easier to use because of its Ethernet controllability where the relay logic is handled by an embedded web server. But that option was discarded due to its bigger size (9in x 7in. x 4in.).

For outdoor applications such as ours, a stand-alone 90-psi pressure line is needed. This can be achieved by the use of a half-size nitrogen (N_2) bottle and a regulator (both of which can be rented from suppliers for initial prototype tests). Nitrogen, a dry gas ideal for our purposes, is compressed at 2000 psi in these cylindrical bottles which are typically about 2.5 ft long and about 0.5 ft in diameter. The pressure can be stepped down to the required 90 psi with a regulator. The N_2 bottle can be installed next to the data-acquisition-enclosure with some basic protection from the elements (sun and rain). For applications where the probe is installed on top of a tower, the N_2 bottle (and regulator) can be installed at the foot of the tower and 0.25 in. diameter pressure lines can be run all the way up to the MSCP3200. The bottle can be replaced when used up. The entire purging system would cost $1575 (for the three main units).

Design 2: The second design is based on the purging system in PSI Inc.'s Electronic Pressure Scanner (ESP). This design uses a pneumatically controlled sliding bar that simultaneously valves all pneumatic lines. It should be noted that this is different from the earlier design where each valve module was a combination of eight different valves. To illustrate this point, the schematic depicting the internal plumbing of the ESP sensor is shown in Fig. 6.19.

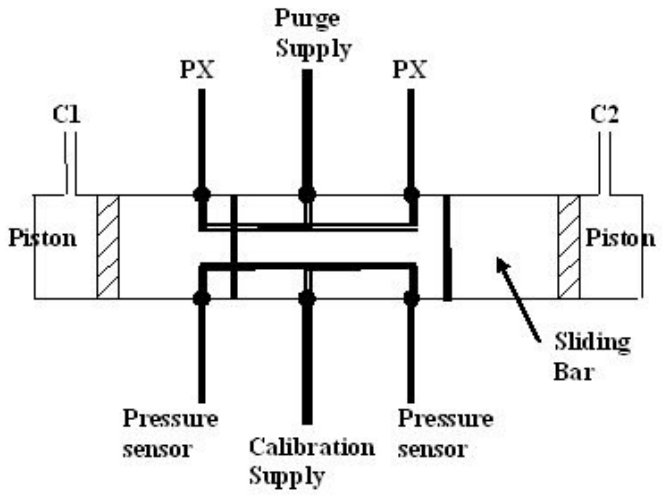

Fig. 6.19 Purging system of an Electronic Pressure Scanner (ESP) – (Courtesy: PSI, Inc.).

The ports named PX are the input pressure channels. The sliding bar (sandwiched between the pistons) has a rectangular cross-section and is controlled by applying 90 psi pressure to the pistons at C1 and C2. In the figure, the valve system is in purge mode, where all the input channels have been manifolded to a purge port which is typically charged at 90 psi. In this mode, as can be seen, the calibration manifold is simultaneously aligned with the pressure sensors. Hence, a calibration or zeroing of the sensors can be performed in parallel. When the purging and/or zeroing is finished, by applying a 90 psi pressure to C2, the sensor is switched back to RUN mode (not shown in figure), for flow pressure data acquisition. In this mode, the input channels are aligned with the bank of transducers at the bottom and the purge (and calibration) manifolds are completely isolated. A similar design with twelve input ports can be employed for the Weatherprobe. All pneumatic lines in the sliding bar can be precision machined using Computer Numerical Control (CNC) machines. At each tubing interface of the sliding bar, an O-ring with some grease for lubrication will ensure good sealing and smooth sliding. It is also necessary to ensure that the size of the module does not exceed 2.5 in. x 2 in. x 1in due to limited availability of space inside the probe's spherical head. Since this design can be developed "in-house", it is preferred over the previous one based on cost considerations.

During field tests, only a zeroing of the sensors is intended (and necessary). Hence, the calibration manifold supply is connected simply to the reference pressure of the sensors (typically just the atmospheric pressure). The zeroing can be performed at intervals of every 1 hour or 2 hours to account for temperature drift of the sensor voltages. Each zeroing takes only about a few hundred milli-seconds. The purging of the tubes, however, takes longer. It is recommended that the purging of the tubes to eliminate contaminants and condensed water is performed for at least 2-3 minutes. This is because of the tendency of any condensed water droplets to split into smaller ones and stick to the tube walls before they are successfully extricated. Purging can be done less frequently, say every 6 hours. For outdoor applications, it is a good idea to ensure a

purge at dawn when the dew point of the atmosphere is at its lowest (relative humidity can reach as high as 90% at this time of day).

6.4 INERTIAL EFFECTS ON SPHERICAL PROBES

This section is a study of how fluid inertia-related unsteady aerodynamic effects affect data-reduction of spherical probes and how to correct for them using a simple iterative technique. Only a quasi-steady calibration of the probe can be performed in a wind-tunnel. In an accelerated (unsteady) flow field, the pressure distribution over a sphere (based on potential flow theory) depends on both the instantaneous velocity and the rate of change of velocity (Karamcheti[53]). Therefore, unsteadiness in the flow can change the instantaneous port pressures, thus introducing errors in the calculated (instantaneous) flow properties. Therefore, a correction needs to be performed on the calculated properties during reduction.

From the general potential flow-over-a-sphere equation for unsteady flows, the instantaneous pressure at any port is given as:

$$p_1(t) = P_s + q(t)\cdot C_{ps}(\theta_1^*) + q(t)\cdot K(t)\cdot\cos(\theta_1^*) \qquad (6.4)$$

where

P_s is the flow static pressure,

Θ_1* is the central angle between the stagnation point and the port location,

$q(t) = 1/2\cdot\rho\cdot U(t)^2$ {U(t) is the instantaneous flow speed}, and

$$K(t) = \frac{R}{U(t)^2}\frac{dU}{dt} \quad \text{the non-dimensionalized acceleration} \qquad (6.5)$$

where, R is the radius of the sphere

Equation 6.4 shows that port pressures are not only dependent on the dynamic pressure of the fluid and the tip geometry (in this case, spherical), but also on an additional term that is proportional to the flow acceleration. As can be seen from equation 6.5, the

magnitude of the unsteady effect is proportional to the radius of the sphere and the flow acceleration, and is inversely proportional to the square of the instantaneous velocity magnitude. First, the effects of K, on the data-reduction of probes that have been calibrated in steady flow, will be demonstrated. To test the unsteady errors introduced in reduction, at different stagnation point locations on the surface of the probe, a sinusoidally oscillating air stream was used to generate pressure data at all ports using the following U(t) in equation (6.4).

$$U(t) = U_{mean}(1 + A\sin(2\pi ft)) \tag{6.6}$$

Only purely axial oscillations are considered, since angular oscillations do not contribute to inertial effects. The Θ, Φ, and U_{mag} errors were found to be as follows:

Standard deviations ("steady" prediction: $K_{max} \sim 1$):

- Θ 1.58°
- Φ 0.87°
- U_{mag} **13.6 %**

As can be seen, although the Θ and Φ predictions are not bad, the U_{mag} error is very high and needs correction. The significant inertial effects in the port pressures are not transmitted down to the calculated flow angles. This is very remarkable and fortunate since it implies that the angle coefficients from steady calibration can be also used in unsteady flow fields for the calculation of the flow angles. Calculation of the velocity magnitude, however, requires quantification of and correction for the fluid inertial effects.

The iteration scheme

In the reduction routine, U_{mag} is calculated from the non-dimensionalized static pressure coefficient Cs.

$$C_S = \frac{p_1 - P_s}{q_{est}} \tag{6.7}$$

where, q_{est} is the dynamic pressure estimate.

The unsteady equation for the port pressure is given as

$$p_1(t) = P_s + q_{est} \cdot C_s + q(t) \cdot K(t) \cdot \cos(\theta_1^*) \quad (6.8)$$

where the "steady" pressure at the port is simply

$$p_{steady} = P_s + q_{est} \cdot C_s \quad (6.9)$$

The correction scheme strives to find this "steady" pressure for all ports (at least for the 4 highest ones) because the probe calibration data itself is in steady flow. It takes advantage of the fact that the non-dimensionalized angle coefficients C_Θ and C_Φ (and hence Θ, Φ) do not have significant errors in them due to inertial effects. Since C_s is calculated from (C_Θ, C_Φ), it can be used (if known) in equation (6.8) and the unsteady term attained. (It should be noted that smaller case θ-ϕ and bigger case Θ-Φ have been used interchangeably above without any loss of generality.) The unsteady term is analogous to an error term or residual. The K(t) value can then be estimated as

$$K(t) = (p_1(t) - P_s - q_{est} \cdot C_s) \; / \; q_{calc} \; / \; \cos(\theta_1^*) \quad (6.10)$$

Again, since the (Θ, Φ) prediction is fairly good (even without unsteady corrections), that can be used to calculate Θ_1* also (in equation (6.10)). This K value is a very rough approximate mainly because q_{est} (the estimated dynamic pressure), although is a good approximation, has some errors in it. Hence iterations are needed – each iteration progressively calculating the K value for that data point. During every iteration, the highest four port pressures are corrected with the above K. The q_{est}, and hence the predicted U_{mag}, can be expected to approach the correct value with every iteration. The Θ, Φ values can also be expected to improve. The main assumption in this technique is that the unsteady pressure variation follows the theoretical equation (Johansen and Rediniotis[34-36]). The steady part itself is calculated entirely from experimental probe calibration data.

Theoretical data using equation (6.4) was generated to study the scheme's capabilities. The following sinusoidal flow was used on a sphere of 3 in. radius.

U_{mag} mean = 20m/s

Oscillation amplitude (A) = 20%

Oscillation frequency (f) = 200Hz

This produced a K(t) variation with a maximum of ~1.0 as shown in Fig. 6.20.

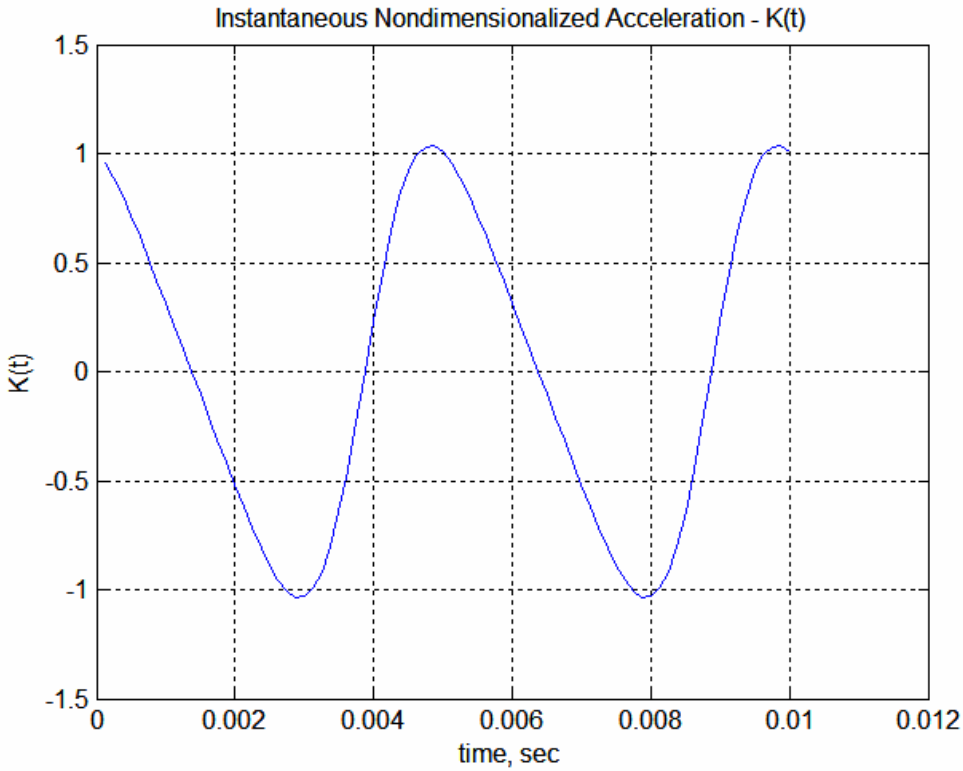

Fig. 6.20 Instantaneous non-dimensionalized acceleration (K(t)): U_{mag} mean = 20m/s; A = 20%; f = 200Hz.

The prediction accuracy without the unsteady correction scheme is repeated here:

Standard deviations ("steady" prediction: K_{max} ~ 1):

- Θ 1.58°
- Φ 0.87°
- U_{mag} **13.6 %**

After employing the correction routine, the accuracy in U_{mag} was greatly improved. Even the Θ and Φ predictions were much better.

Standard deviations (using the scheme: K_{max} ~ 1):

- Θ 0.12°
- Φ 0.09°
- U_{mag} **0.30 %**

Using U(t) that is not a well-behaved sine wave but with the same bounds for K gives the same errors. This is expected because the scheme does not require a time series data. Another check was to see if the iterations introduce any errors in predicting a steady flow itself. None was found with theoretical data. When this was checked on actual calibration data, the Θ and Φ errors were unchanged. The U_{mag} error, however, increased by about 0.1%. This is a small price to pay to be able to account for inertial effects in the prediction.

Standard deviations (without the scheme: on steady (wind-tunnel) calibration data):

- Θ 0.34°
- Φ 0.26°
- U_{mag} 0.56 %

Standard deviations (with the scheme: on steady (wind-tunnel) calibration data):

- Θ 0.34°
- Φ 0.26°
- U_{mag} 0.68 %

For values of K higher than 1, the reduction accuracy deteriorated rapidly. But, a K value of 1, in spite of the big radius of the probe, is sufficiently high. To see what a K value of 1 would mean to wind speed data from the Weatherprobe, consider a mean wind speed of say 5m/s. For the flow to attain a K value of 1, the wind has to shift to 8.3m/s in just 0.01s or to 38.3m/s in just 0.1 seconds. For higher mean wind speeds the jumps will be much higher. Such scenarios are unlikely and outside the region of our interest.

6.5 REYNOLDS NUMBER EFFECTS

The Reynolds number of a flow over any body is defined as

$$Re = \frac{\rho V D}{\mu} \tag{6.11}$$

where, ρ = density of fluid medium

V = velocity magnitude

D = reference length = diameter (for a sphere)

μ = viscosity of fluid medium

For our Weatherprobe in standard atmospheric conditions, the parameters have values as follows:

$\rho = 1.225$ kg/m^3

$D = 6$ inches $= 0.15$ m

$\mu = 1.8 \times 10^{-5}$ kg/m/s

Based on the range of its pressure sensors (±5 in. H_2O), the Weatherprobe in its current state operates up to flow speeds (V) of about 45 m/s assuming standard atmospheric conditions (note that 1 in. H_2O = 248.845 Pa). Hence it operates in a Reynolds number range of up to $5*10^5$. Uniform flow over a sphere is divided chiefly into two regimes based on Reynolds number – the subcritical regime with laminar boundary layer separation and the supercritical regime with turbulent boundary layer separation. The critical Reynolds number (Re_{cr}) is around $3.7*10^5$. Thus the range of operation of the Weatherprobe exists on both regimes – and in the transition regime.

If the following facts are also considered: a) the transition from laminar to turbulent occurs over a range of Reynolds numbers in the region of $5*10^4$ to $5*10^5$, b) the sphere is mounted on a cylindrical shaft which could affect the flow and c) the turbulence in the flow itself is unknown and not accounted for, it is seen that no reasonable estimate can be made of the type of flow over the Weatherprobe. This means that the flow and hence

the pressure distribution on the surface could be different during the calibration and during operation. This difference could induce errors in the calculated flow properties. The magnitude of such errors needs to be estimated and corrected if necessary (and if possible). The worst-case scenario is when the calibration is done in a pure laminar regime and the probe operation is in the fully turbulent regime or vice versa.

Constantinescu and Squires[54, 55] calculated the flow over the sphere over the entire transition regime numerically using detached-eddy simulation (DES). They validated their results using comparisons to experimental results. The pressure distribution over a sphere in the laminar regime is also given in White[46] and is the same as equation (4.2). The pressure distribution in the fully turbulent regime[54] has a good correspondence to our C_p curve (turbulent) in Fig. 6.21 obtained from calibration data. A polynomial curve-fit to our calibration data provided the following equation for the pressure distribution over a sphere in fully turbulent flow.

$$C_p = 0.5394 \cdot \Theta^6 - 1.7044 \cdot \Theta^5 + 2.1187 \cdot \Theta^4 - 0.4138 \cdot \Theta^3 - .... \\ 1.9935 \cdot \Theta^2 + 0.0125 \cdot \Theta^1 + 1.0000 \qquad (6.12)$$

Using equations 4.2 and 6.12, theoretical data (both calibration and test) can be generated. Hence, the prediction accuracies for “turbulent” test data can be checked by reducing them with “laminar” calibration data and vice versa using our reduction algorithm. The corresponding error data is given in Table 6.1. Similar errors were seen when the calibration and test data were switched.

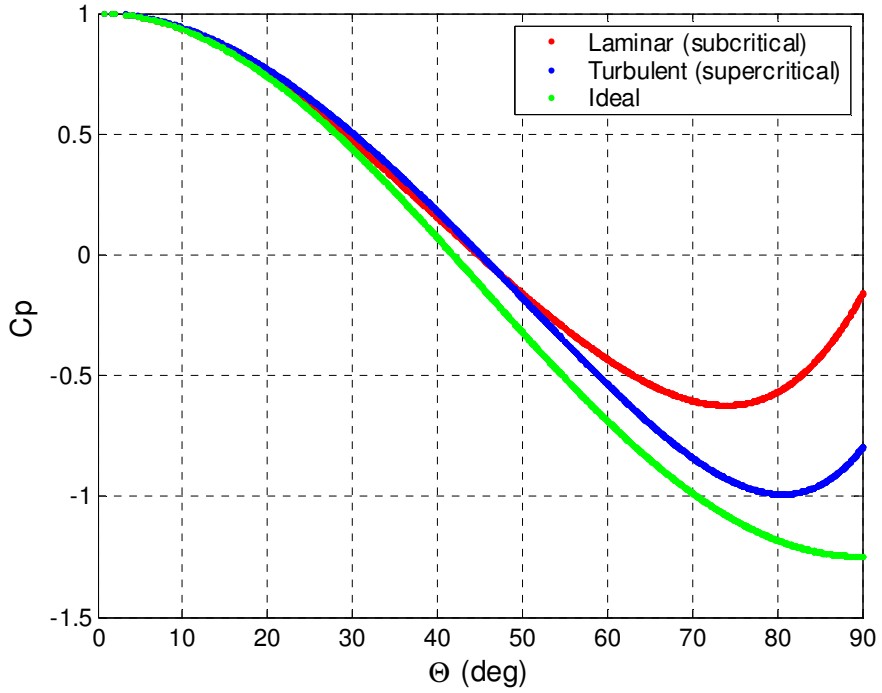

Fig. 6.21 Pressure coefficient C_p over the sphere in different regimes.

Table 6.1. Predicted flow variables: theoretical data – "laminar" calibration; "turbulent" test.

Flow variable	Mean (μ)	Standard deviation (σ)
Θ (deg)	-0.34	1.70
Φ (deg)	0.04	0.62
U_{mag} (%)	4.61	2.66

These are the worst-case-scenario errors. Due to high turbulence in the flow in real field operations of the Weatherprobe, it is highly unlikely that the probe would ever be in the laminar regime. The calibration data as demonstrated in Fig. 6.21 is also in the turbulent regime. Hence a scenario giving rise to the errors in Table 6.1 is highly unlikely in real applications. An easy solution, if necessary, is to roughen up the probe surface to ensure turbulent separation.

7 CONCLUSIONS

Taking advantage of the new definitions previously developed by the author for non-dimensional coefficients in multi-hole probes (which obviate the necessity for a symmetric arrangement of ports), an omni-directional velocity measurement probe was developed with a mere twelve pressure ports. Only four pressure ports are used at any measurement point thus avoiding redundancy. The probe was designed with a spherical head of 0.375 in. and fabricated in brass with stainless steel internal pressure tubing. It was calibrated at multiple Mach numbers in a jet facility and tested to assess its accuracy of prediction of the flow variables – three velocity components and static pressure.

The 12-hole probe, which is essentially an optimized version of the 18-hole probe, is a valuable tool in detailed omni-directional flow field measurement. It has the same functionality as the earlier 18-hole design but with many more advantages in terms of spatial resolution, frequency response and cost. The probe can be employed in the entire subsonic regime. Sensitivity estimates reveal the contributions of the pressure sensor accuracy on the output (calculated flow variable) variability. Error estimates with experimental data show good prediction capability – 0.5° in Θ, 0.7° in Φ and 0.6% in velocity magnitude (95% confidence).

A new method was developed that effectively predicts offset angle errors (horizontal and vertical) due to misalignment of multi-hole probes in wind-tunnel calibrations. The offset-correction algorithm implemented in Matlab was initially tested with theoretical data and was found to predict horizontal offsets within ±0.05° and vertical offsets within ±0.1° for spherical-head probes. There was excellent agreement between the corrected calibration data obtained from the algorithm and the actual corrected data computed directly. The algorithm was shown to be independent of any symmetry requirement in the arrangement of ports. Since the offsets are calculated from each port separately, the results obtained from different ports of the same probe should match well. This was

confirmed with the initial theoretical data tests. These offsets from all the ports are then averaged to find the final offset error in the probe calibration.

The algorithm was then used for offset calculations with experimental calibration data of different multi-hole probes. It provided good results with many 5- and 7-hole data. For some of the 5- and 7-hole probes, however, there were cases of mismatch in the values calculated from different ports i.e., the offsets calculated from different ports of the same probe were as much as 1° off from one another, indicating a bad prediction. On the other hand, spherical-head probes (18- and 12-hole) fared extremely well. The predictions were good for almost all of them even at Mach numbers as high as 0.7. The offsets were generally on the order of 0.5° to 1° in horizontal and vertical angles and sometimes as high as 1.5° to 2°. The accuracy (based on the difference between the maximum and the average from all ports) was within ±0.1° in horizontal offsets and ±0.2° in vertical offsets. Although the algorithm cannot yet be reliably used for 5- and 7-hole probes, it is ready for the omni-directional 12- and 18-hole probes, as long as one confirms that the offsets calculated from different ports match within at least ±0.2°. Although these offset corrections address issues in standard multi-hole probes, their application is not limited to them. The technique can be readily extended to all probes including the wind speed probe.

An all-weather pressure-based anemometer for measurement of accurate real-time 3-D wind speeds was successfully developed and field tested. The probe had a 6-in. spherical head and a 4-in.-long cylindrical sting, all fabricated in aluminum. It achieved the goal of a measurable velocity inclination range of ±45° from the horizontal plane and a range of 50 m/s with minimum number of pressure ports. The design also achieved the smallest probe size, given the necessity to mount (and easily access) all heating and sensing hardware inside the spherical probe head.

All associated instrumentation (with stringent ruggedness requirements for outdoor applications) was set up. The generic reduction algorithm was modified to suit the Weatherprobe design and incorporated into the data-acquisition system. A GUI was developed in order to interface with the data acquisition and to acquire and display real-time wind data. The probe was safeguarded from sub-zero weather conditions by heating elements inside the probe. The temperature inside the probe head was constantly monitored while a feedback circuitry (involving a temperature controller) maintained the desired temperature. The probe was extensively calibrated (prior to use) to get pressure-velocity relations at two different speeds of 10 m/s and 28 m/s.

The probe's performance was evaluated in a low-speed wind-tunnel to demonstrate hardware functionality and to estimate prediction errors. Two different sensors were tried – one with ±50 mmHg range and the other with ±5 in.H_2O range. With the latter, due to its higher sensitivity (lower range), very good prediction was obtained in the wind-tunnel and at the test site. Based on the means and standard deviations of the prediction errors, the Weatherprobe's prediction accuracy can be stated as 2.5° in the flow angles and 2.5% in the wind speed magnitude with 95% confidence. A rain simulation experiment was designed and built to study the effects of rain. The Weatherprobe provided reliable accurate data even in rainy conditions. Wind data at frequencies as high as 100 Hz can be achieved with the probe. To this end, the frequency response of the pneumatic lines was analyzed for pressure correction. Effects of fluid inertia in unsteady flows and of Reynolds number were also studied and necessary correction procedures outlined.

Field tests were performed on top of a 25m tall tower next to a sonic anemometer and two cup anemometers for comparison and overall validation. The field tests were intended mainly to prove the hardware's capability for extended unattended operation outdoors. Over the many days the probe was installed in the field, there were days with heavy rain and high mid-day temperatures (103°F). The probe and its system performed

reliably under all these circumstances. Wind speed and direction data at 1Hz was obtained over a period of 3.5 days. Although the measurement accuracy of the probe was validated initially through wind-tunnel tests, the excellent correspondence with data from the cup anemometer and more importantly the sonic anemometer served to clearly demonstrate reliable and accurate performance of the Weatherprobe.

In terms of technology marketability, the Weatherprobe's stiffest competition is a 3-d sonic anemometer. The Weatherprobe, with its advantages in terms of cost, accuracy, high-frequency data-acquisition, real-time data-reduction and rugged operation in hostile environments (all of which have been proved in this work) makes it a potential tool of choice for real-time 3-dimensional wind speed measurements spanning a wide range of applications.

REFERENCES

[1]Everett, K. N., Gerner, A. A., and Durston, D. A., "7-Hole Cone Probes for High Angle Flow Measurements: Theory and Calibration," *AIAA Journal*, Vol. 21, No. 7, 1983, pp. 992-998.

[2]Gallington, R. W., "Measurements of Very Large Flow Angles with Non-Nulling 7-Hole Probe," USAFA-TR-80-17, U.S. Air Force Academy, CO, 1980.

[3]Rediniotis, O. K., Hoang, N. T., and Telionis, D. P., "The 7-Hole Probe: Its Calibration and Use," *Forum on Instructional Fluid Dynamics Experiments*, Vol. 152, edited by R.S. Budwig, J.F. Foss, and D. E. Stock, American Society of Mechanical Engineers, New York, 1993, pp. 21-26

[4]Houtman, E. M., and Bannink, W. J., "Calibration and Measuring Procedure of a 5-Hole Hemispherical Head Probe in Compressible Flow," Delft University of Technology, Report LR-585, Apr. 1989.

[5]Zilliac, G. G., "Modelling, Calibration, and Error Analysis of 7-Hole Pressure Probes," *Experiments in Fluids*, Vol. 14, No. 1/2, 1993**,** pp. 104-120.

[6]Bryer, D.W., and Pankhurst, R. C., *Pressure-Probe Methods for Determining Wind Speed and Flow Direction*, Her Majesty's Stationary Office **/** National Physics Laboratory, The Campfield Press, St. Albans, 1971.

[7]Flanagan Jr., M. J., and Hiltner, D. W., "Calibration of a Transonic 5-Hole Probe for a Multi-Element Airfoil Cascade Facility," AIAA 93-2471, 29th Joint Propulsion Conference and Exhibit, Monterey, CA, June 1993.

[8]Bare, E. A., Reubush, D. E., and Haddad, R. C., "Flow Field over the Wing of a Delta-Wing Fighter Model with Vortex Control Devices at Mach 0.6 to 1.2," NASA TM-4296, April 1992.

[9]Dominy, R. G., and Hodson, H. P., "An Investigation of Factors Influencing the Calibration of 5-Hole Probes for Three Dimensional Flow Measurement," *Journal of Turbomachinery*, Vol. 115, No. 3, July 1993, pp. 513-519.

[10]Naughton, J.W., Cattafesta III, L.N., and Settles, G.S., "A Miniature, Fast-Response 5-Hole Probe for Supersonic Flow Field Measurements," AIAA-92-0266, 30th Aerospace Sciences Meeting and Exhibit, Reno, NV, Jan. 1992.

[11]Naughton, J.W., Cattafesta III, L.N., and Settles, G.S., "Miniature Fast Response 5-Hole Conical Probe for Supersonic Flow Field Measurements," *AIAA Journal*, Vol. 31, No. 3, Mar. 1993, pp. 453-458.

[12]Porro, A. R., "Pressure Probe Designs for Dynamic Pressure Measurements in a Supersonic Flow Field," NASA/TM-2001-211096, July 2001.

[13]Smart, M. K., Kalkhoran, I. M., and Bentson, J., "Measurements of Supersonic Wing Tip Vortices," *AIAA Journal*, Vol. 33, No. 10, Oct. 1995, pp. 1761-1768.

[14]Milanovic, I. M., and Kalkhoran, I. M., "Numerical Calibration of a Conical 5-Hole Probe for Supersonic Measurements," *Measurement Science and Technology*, Vol. 11, No. 12, 2000, pp. 1812-1818.

[15]Johansen, E. S., Rediniotis, O. K., and Jones, G., "The Compressible Calibration of Miniature Multi-Hole Probes," *Journal of Fluids Engineering*, Vol. 123, 2001, pp. 128-138.

[16]Rediniotis, O. K., and Vijayagopal, R., "Miniature Multihole Pressure Probes and Their Neural-Network-Based Calibration," *AIAA Journal*, Vol. 37, No. 6, Jun. 1999, pp. 666-674.

[17]Ramakrishnan, V., and Rediniotis, O. K., "Calibration and Data-Reduction Algorithms for Nonconventional Multihole Pressure Probes," *AIAA Journal*, Vol. 43, No. 5, 2005, pp. 941-952.

[18]Kinser, R. E., and Rediniotis, O. K., "Development of a Nearly Omni-directional Velocity Measurement Pressure Probe," *AIAA Journal*, Vol. 36, No. 10, 1998, pp. 1854-1860.

[19]Ashby, N., and Brittin, W. E., "Thomson's Problem," *American Journal of Physics*, Vol. 54, No. 9, Sept. 1986, pp. 776-777.

[20]Edmundson, J. R., "The Distribution of Point Charges on the Surface of a Sphere," *Acta Crystallographica Section A: Foundations of Crystallography*, Vol. 48, Part 1, 1992, pp.60-69.

[21]Erber, T., and Hockney, G. M., "Equilibrium Configurations of N Equal Charges on a Sphere," *Journal of Physics A. Mathematical and General*, Vol. 23, No. 7, Dec. 1991, pp. L1369-L1377.

[22]Glasser, L., and Every, A. G., "Energies and Spacings of Point Charges on a Sphere," *Journal of Physics A. Mathematical and General*, Vol. 25, No. 9, May 1992, pp. 2473-2482.

[23]Clark, E. L., Henfling, J. F., and Aeschliman, D. P., "Calibration of Hemispherical-Head Flow Angularity Probes," AIAA-92-4005, 17th Aerospace Ground Testing Conference, Nashville, TN, 1992.

[24]Gonsalez, J. C., and Arrington, E. A., "Five–Hole Flow Angle Probe Calibration for the NASA Glenn Icing Research Tunnel", AIAA-96-2201, 19th Advanced Measurement and Ground Testing Technology Conference, New Orleans, LA, 1996.

[25]Zeiger, M. D., and Schaeffler, N. W., "Correcting Multi-Hole Probe Alignment Bias Errors Post Calibration," AIAA-2001-0900, 39th Aerospace Sciences Meeting and Exhibit, Reno, NV, 2001.

[26]Thompson, S. A., and Hackett, J. E., "Range Extension for 7-holed Probes," AIAA-98-0635, 36th Aerospace Sciences Meeting and Exhibit, Reno, NV, Jan. 1998.

[27]Pisasale, A. J., and Ahmed, N. A., "Examining the Effect of Flow Reversal on 7-Hole Probe Measurements," *AIAA Journal*, Vol. 41, No. 12, 2003, pp. 2460-2467.

[28]Rediniotis, O. K., and Pathak, M. M., "A Simple Technique for Frequency Response Enhancement of Miniature Pressure Probes," *AIAA Journal*, Vol. 37, No. 7, 1999, pp. 897-899.

[29]Bergh, H., and Tijdeman, H., "Theoretical and Experimental Results for the Dynamic Response of Pressure Measuring Systems," NLR-TR-F.238, Jan. 1965.

[30]Johansen, E. S., "Development of a Fast-Response Multi-Hole Probe for Unsteady and Turbulent Flow Fields," Ph.D. Dissertation, Aerospace Engineering Department, Texas A&M University, College Station, Texas, Dec. 2001.

[31]Sieverding, C. H., Arts, T., Denos, R., and Brouckaert, J.-F., "Measurement Techniques for Unsteady Flows in Turbomachines," *Experiments in Fluids*, Vol. 28, No. 4, Apr. 2000, pp. 285-321.

[32]Kupferschmied, P., Koppel, P., Gizzi W., Roduner C., and Gyarmathy, G., "Time-resolved Flow Measurements with Fast-response Aerodynamic Probes in Turbomachines," *Measurement Science and Technology*, Vol. 11, Part 7, 2000, pp. 1036-1054.

[33]Humm, H. J., Gossweiler, C. R., and Gyarmathy, G., "On Fast-Response Probes: Part 2 – Aerodynamic Probe Design Studies," ASME International Gas Turbine and Aeroengine Congress and Exposition, The Hague, Netherlands, June 1994.

[34]Johansen, E. S., and Rediniotis, O. K., "Unsteady Calibration of Fast-Response Pressure Probes, Part 1: Theoretical Studies," *AIAA Journal*, Vol. 43, No. 4, 2005, pp. 816-826.

[35]Johansen, E. S., and Rediniotis, O. K., "Unsteady Calibration of Fast-Response Pressure Probes, Part 2: Water-Tunnel Experiments," *AIAA Journal*, Vol. 43, No. 4, 2005, pp. 827-834.

[36]Johansen, E. S., and Rediniotis, O. K., "Unsteady Calibration of Fast-Response Pressure Probes, Part 3: Air Jet Experiments," *AIAA Journal*, Vol. 43, No. 4, 2005, pp. 835-845.

[37]Kristensen, L., "The Perennial Cup Anemometer," *Wind Energy*, Vol. 2, No. 1, Aug. 1999, pp. 59-75.

[38]Makkonen, L., Lehtonen, P., and Helle, L., "Anemometry in Icing Conditions," *Journal of Atmospheric and Oceanic Technology*, Vol. 18, No. 9, Sep. 2001, pp. 1457-1469.

[39]Papadopoulos, K. H., Stefanatos, N. C., Paulsen, U. S., and Morfiadakis, E., "Effects of Turbulence and Flow Inclination on the Performance of Cup Anemometers in the Field," *Boundary-Layer Meteorology*, Vol. 101, No. 1, Oct. 2001, pp. 77-107.

[40]Kristensen, L., "Cup Anemometer Behavior in Turbulent Environments," *Journal of Atmospheric and Oceanic Technology*, Vol. 15, No. 1, Feb. 1998, pp. 5–17.

[41]Lockhart, T. J., "Anemometer Performance Determined by ASTM Methods," *Journal of Atmospheric and Oceanic Technology*, Vol. 4, No. 1, Mar. 1987, pp. 160-169.

[42]Krishnasamy, S. G., "Ice-Free Anemometer: Laboratory and Field Testing," Proceedings of the Third International Workshop on the Atmospheric Icing of Structures, Vancouver, Canada, May 1986.

[43]Hogstrom, U., and Smedman, A., "Accuracy of Sonic Anemometers: Laminar Wind-Tunnel Calibrations Compared to Atmospheric In Situ Calibrations against a Reference Instrument," *Boundary-Layer Meteorology*, Vol. 111, No. 1, 2004, pp. 33-54.

[44]Siebert, H., and Teichmann, U., "Behaviour of an Ultrasonic Anemometer under Cloudy Conditions," *Boundary-Layer Meteorology*, Vol. 94, No. 1, Jan. 2000, pp. 165-169.

[45]Wamser, C., Peters, G., and Lykossov, V. N., "The Frequency Response of Sonic Anemometers," *Boundary-Layer Meteorology*, Vol. 84, No. 2, Aug. 1997, pp. 231-246.

[46]White, F. M., "Laminar Boundary Layers," *Viscous Fluid Flow*, 2nd ed., McGraw-Hill, New York, 1991, pp. 298.

[47]Coleman, H. W., and Steele, W. G., "Statistical Considerations in Measurement Uncertainties," *Experimentation and Uncertainty Analysis for Engineers*, 2nd ed., Wiley-IEEE, New York, 1999, pp. 34.

[48]Saltelli, A., Tarantola, S., Campolongo, F., and Ratto, M., *Sensitivity Analysis in Practice: A Guide to Assessing Scientific Models*, John Wiley & Sons Ltd., West Sussex, England, 2004.

[49]Awbi, H. B., and Tan, S. H., "Effect of Wind-Tunnel Walls on the Drag of a Sphere," *Journal of Fluids Engineering*, Vol. 103, No. 3, Sept. 1981, pp. 461-465.

[50]Hensel, R. W., "Rectangular-Wind-Tunnel Blocking Corrections using the Velocity-Ratio Method," NACA TN-2372, June 1951.

[51]Peters, G., Fischer, B., and Kirtzel, H. J., "One-Year Operational Measurements with a Sonic Anemometer–Thermometer and a Doppler Sodar," *Journal of Atmospheric and Oceanic Technology*, Vol. 15, No. 1, Feb. 1998, pp. 18-28.

[52]Arya, S. P., *Introduction to Micrometeorology*, 2nd ed., Academic Press, San Diego, 1988.

[53]Karamcheti, K., *Principles of Ideal-Fluid Aerodynamics*, John Wiley & Sons Inc., New York, 1966.

[54]Constantinescu, G., and Squires, K., "Numerical Investigations of Flow over a Sphere in the Subcritical and Supercritical Regimes," *Physics of Fluids*, Vol. 16, No. 5, May 2004, pp. 1449-1466.

[55]Constantinescu, G. S., and Squires, K. D., "LES and DES Investigations of Turbulent Flow over a Sphere," AIAA-2000-0540, 38th Aerospace Sciences Meeting and Exhibit, Reno, NV, Jan. 2000.

APPENDIX A

Machine Drawings for the Weatherprobe

Holes at the port locations to fit 3/8” OD S.S tubes at an angle 30° to the horizontal (when the probe (or sting) axis is vertical).

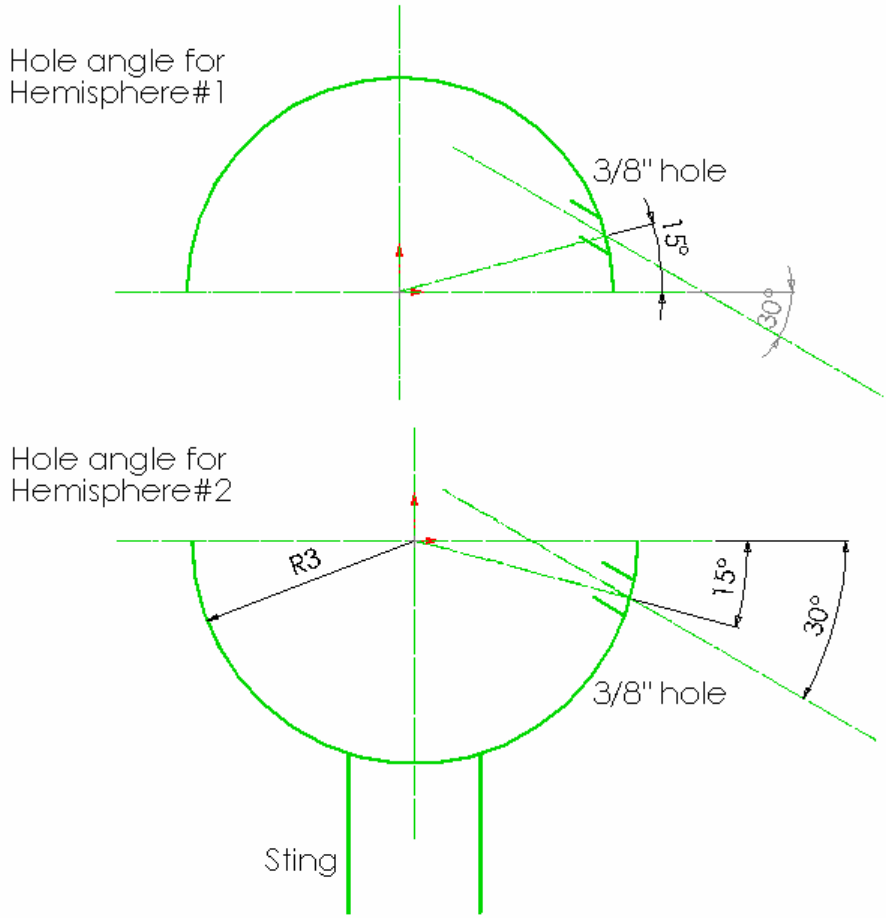

Fig. A-1 Location and orientation of holes.

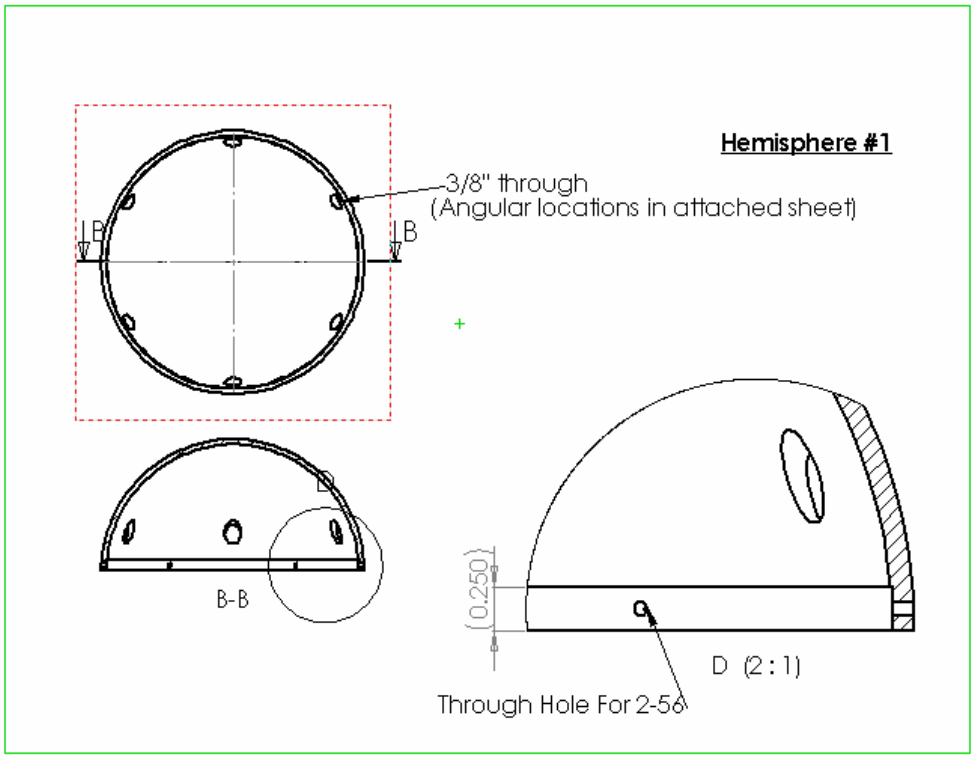

Fig. A-2 Upper hemisphere.

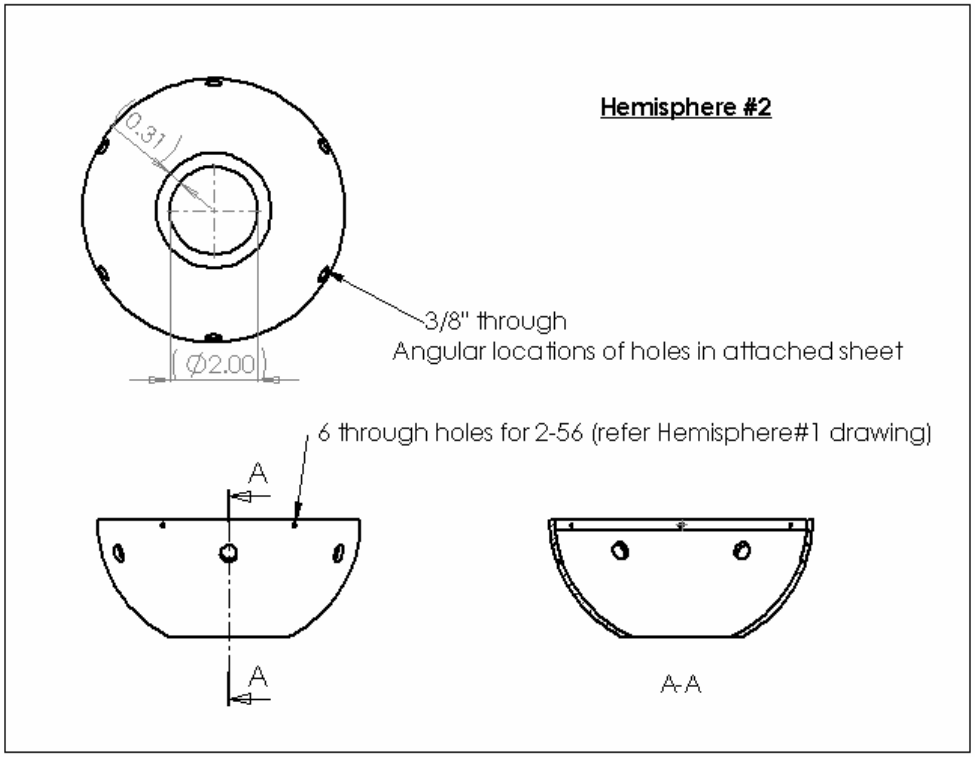

Fig. A-3 Lower hemisphere.

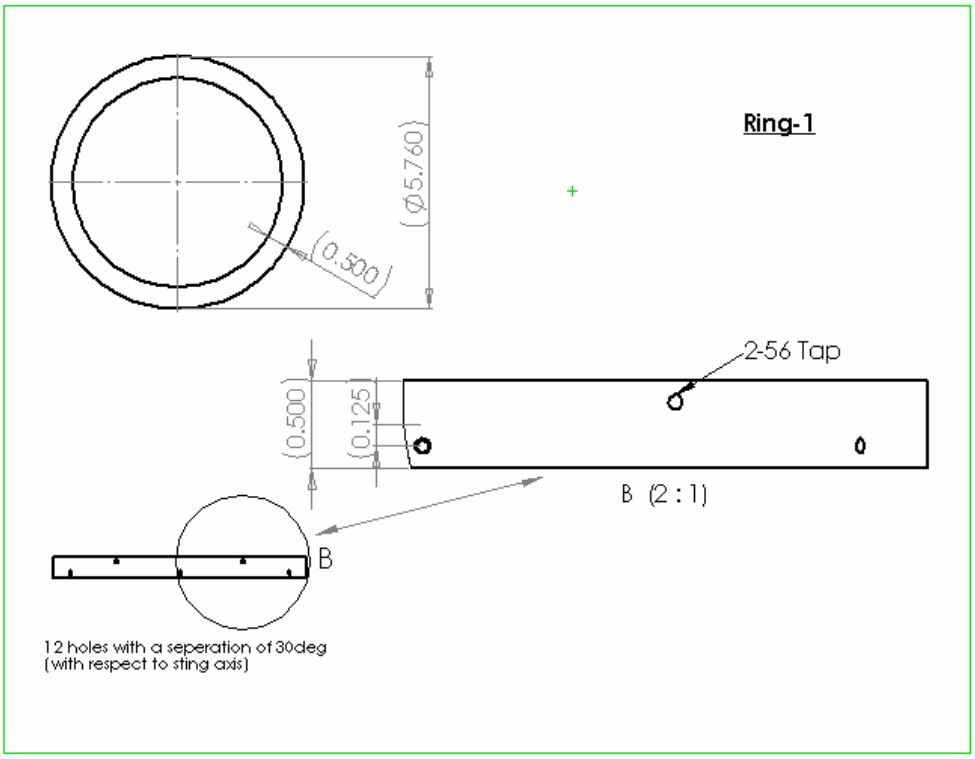

Fig. A-4 Ring-1.

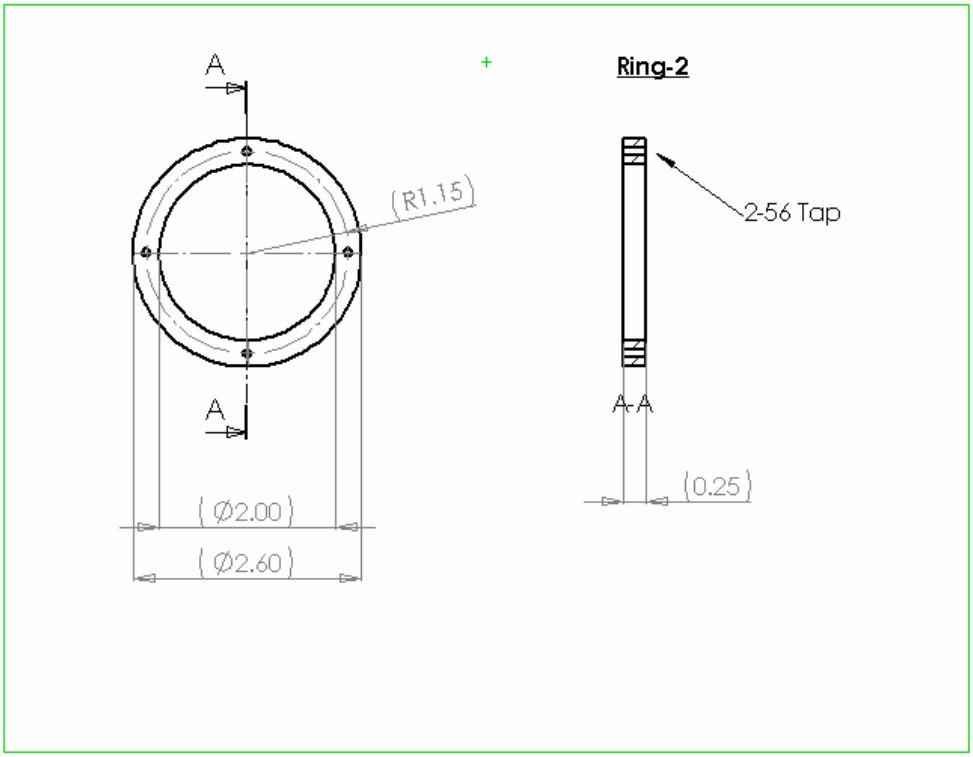

Fig. A-5 Ring-2.

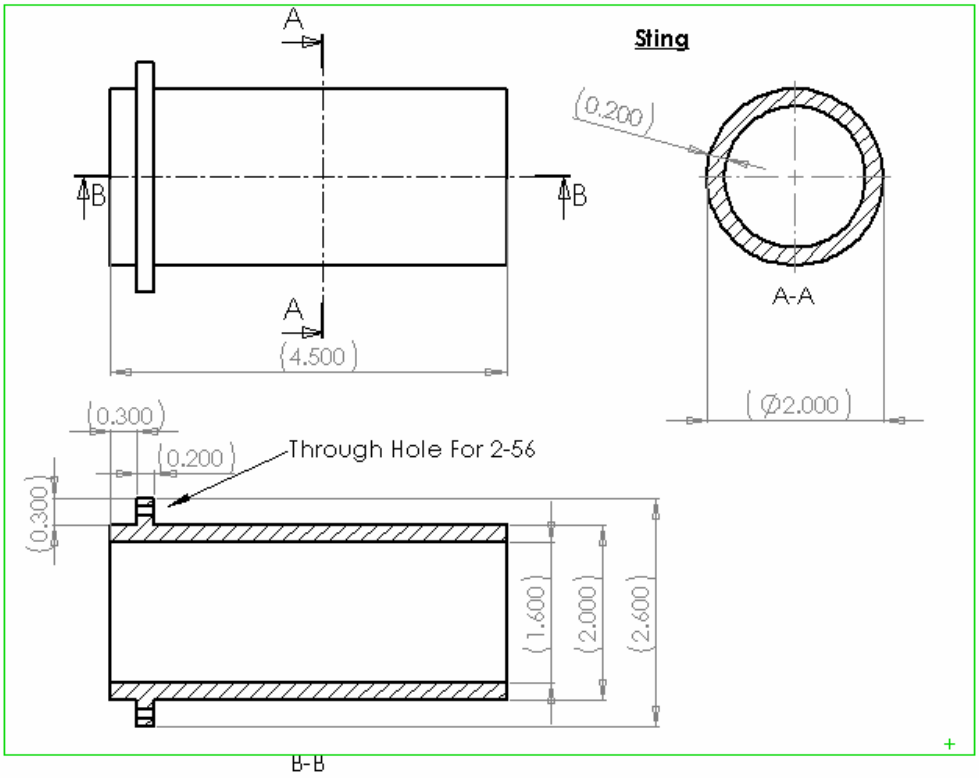

Fig. A-6 Sting.

Port coordinates with respect to the probe (sting) axis: standard spherical coordinate system

Port Number	Theta (deg)	Phi (deg)
1	75	0
2	75	60
3	75	120
4	75	180
5	75	240
6	75	300
7	105	30
8	105	90
9	105	150
10	105	210
11	105	270
12	105	330

APPENDIX B

Instrumentation and Testing Equipment for the Weatherprobe

Major equipment:

Name / Description	**Manufacturer**	**Model Name / #**
Data acquisition system rugged splash-proof stand-alone with 16-bit A/D board, 100kHz throughput, 1GHz processor and 20GB hard disk w/ power supply	RTD Embedded Technologies	IDAN system CMX37786HX1000HR-512HDD DM6430HR-8-62S VPWR104HRTX-50WS XKCM-30
Terminal board (w/ cable)	RTD Embedded Technologies	TB-50 (w/ IDAN-XKCM17)
Pressure sensors ±50 torr gauge piezoresistive with amplified output	Honeywell International Inc.	40PC series (40PC001B1A)
Pressure sensors ±5 in. H_20 differential piezoresistive with amplified output	Honeywell International Inc.	ASDXL series (X115715-PC)
Power supply 75W, 24V DC	Astrodyne Corp.	RS75-24
Temperature controller w/ temperature readout	Omega Engineering	CNi8-DH-54-EI
Solid-state relay a/c input, DC output w/ heat sink	Omega Engineering	SSRL240DC10 (w/ FHS-1)
Heating elements 120V A/C, rectangular, 10W/sq.in, 3” x 1”,	Omega Engineering	SRFG-103/10-P

silicone-rubber, flexible w/ PSA		
Thermocouple T-type	Omega Engineering	5TC-TT-T-30-36 or SA1-T-SC EXPP-T-20-TWSH-50 TMTSS-062E-12-SMP-M
Hemispheres 6 in. aluminum alloy 3003	The Wagner Companies	B4172
Enclosure fiberglass, sealed (NEMA type 4X), 18" x 16" x 8" w/ baseplate	AdProducts Co.	#23368 (N4X-FG-181608CHQR)
Delphi add-on software SDL-component suite	Lohninger / Epina Software Labs	BasePack, MathPack, GuiPack

Minor equipment / lab accessories:

Name / Description	**Manufacturer**	**Model Name/#**
Pneumatic manifold 12-port	Scanivalve Corp.	TC125-M12
3/8" SS tubes	MSC industrial supply	---
Machine screws 2-56, 3/8" SS phillips flat-head	MSC industrial supply	---
Ferrite beads 0.14" x 0.13"L x 0.05"ID	All Electronics Corp.	FB-65
15-pin D-sub cable 10ft M/F	L-com Inc.	CSMN15MF-10
Thermal grease/ Epoxy for heating elements	Omega Engineering	OB-200-2 OT-201-2
62-pin high-density D-connector	Allied Electronics	D3-62PTES

Spray nozzles	Spraying Systems Co.	1/8HH-1 1/4M-12 1/4HH-5
Enclosure vent louver and grille w/ filter	Hoffman (Distributor: Elliott Electric, Bryan)	AVK33 AFLT33
Hand-held temperature measurement 2-input, all T/C types	Omega Engineering	HH509
Surge protector 2-outlet	Mid-State Electronic Supply Co.	ISOBLOK-2-0

Minor (non-specific) electronics and machine parts have not been noted here.

APPENDIX C

Matlab Code Listing for Step Response of Pneumatic Tubing

```
function StepResponse1
%finds 1) a continuous-time transfer function that corresponds to a given complex frequency response
% and  2) the step response to a given complex frequency response
clear all; close all; clc;

%------------------ Read FR (mag and phase) data --------------------------
FileName = 'Test2.tff';
MagPhase = GetTFF(FileName);
[TotalPts,junk] = size(MagPhase);
TotalPts

f = MagPhase(:,1); % FREQUENCY
mag = MagPhase(:,2); % AMPLITUDE RATIO
phase = MagPhase(:,3).*pi/180; % PHASE SHIFT

%---------------------------------------------------------------------------

%------------------ Get Transfer Function (TF) ----------------------------
m = 4; % # of denominator coefficients
n = 2; % # of numerator coefficients

% w = f;
w = f*2*pi;
w = CorrectW(w); % Correct w = [0, pi]

%Get the Coefficents of the Transfer Fn -----> b = Numerator; a = Denominator
[b,a] = invfreqs(mag.*exp(j*phase),w,n,m,[],500);

PlotTFtoCheck(f,mag,phase,b,a,w); % IMP : This plot should match the TF's Mag and Phase plots

sys = tf(b,a); % complex-valued transfer function model
%---------------------------------------------------------------------------

%------------------ Step Input Response -----------------------------------
[y_step,t,ysd] = step(sys);
figure; step(sys);
xlabel('Time ','FontName','TimesNewRoman','FontSize',12)
ylabel('Normalized amplitude (-)','FontName','TimesNewRoman','FontSize',12)
set(gcf,'Color',[1 1 1])
title('Fig. 3: Step Response', 'FontName','TimesNewRoman','FontSize',14)
set(gca,'FontName','TimesNewRoman','FontSize',10)
grid on

%---------------------------------------------------------------------------
```

```
%------------------ Generic Input Signal ----------------------------------
% sine
Nmult = 15; % multiply this factor to length of "t" to analyze longer time periods
[SizeOf_t, junk] = size(t); %get num of points in matrix "t"
delT = max(t)/(SizeOf_t - 1); % use delta-t in "T" same as that of "t"
Div = 1;
delT = delT/Div; % To increase resolution

%u = 1*(sin(2*pi*T*600));

%non-zero mean (added: Sep 05 2006)
PrMean = 10; %Mean Pressure
PrAmpPcnt = [20,16,12,8,4]; %Amplitude Pcnt: (if set to zero, will work as step response to 0 -->
PrMean)
PrFreq = [40,70,110,155,190];

%u = PrMean + (PrAmpPcnt/100*PrMean) * (sin(2*pi*T*PrFreq));
A = PrAmpPcnt/100.*PrMean;
Nbw1 = 2; %Multiplier to sizeof_t for dividing the time interval. MUST be less than Nmult
Nbw2 = 4; %Multiplier to sizeof_t for dividing the time interval. MUST be less than Nmult
for ijk = 1:Nbw1*SizeOf_t*Div
   T(ijk) = (ijk-1)*delT;
   t1 = T(ijk);
   a1 = -(PrMean)/((Nbw1*SizeOf_t*delT*Div)^2);
   b1 = -2*a1*Nbw1*SizeOf_t*delT*Div;
   c1 = 0;
   %u(ijk) = (PrMean-0)/(Nbw1*max(t)-0)*T(ijk);
   u(ijk) = a1*t1^2 + b1*t1 + c1;

end
for ijk = Nbw1*SizeOf_t*Div+1:Nbw2*SizeOf_t*Div
   T(ijk) = (ijk-1)*delT;
   r1 = randn(1);
   u(ijk) = PrMean;% + (PrAmpPcnt/100*PrMean) * (sin(2*pi*(T(ijk)-T(Nbw1*SizeOf_t))*PrFreq));
   %u(ijk) = u(ijk)*(1+r1*10/100);
end
for ijk = Nbw2*SizeOf_t*Div+1:Nmult*SizeOf_t*Div
   T(ijk) = (ijk-1)*delT;

   u(ijk) = PrMean;
   for ii = 1:size(PrFreq')
      u(ijk) = u(ijk) + A(ii) * (sin(2*pi*T(ijk)*PrFreq(ii)));
   end

   %u(ijk) = u(ijk)*(1+r1*10/100);
end


% Random noise
% for ijk = 1:size(t)
%    r1 = randn(1);
%    u(ijk) = 10*(1+r1*20/100);
% end
```

```
%
% Linear + Noise
% for ijk = 1:size(t)
%     u(ijk) = (20-10)/(0.008-0)*t(ijk) + 10;
% end
% for ijk = 1:size(t)
%     r1 = randn(1);
%     u(ijk) = u(ijk)*(1+r1*20/100);
%     u(ijk) = u(ijk) + r1*20/100;
% end

% figure; plot(T,u);
% xlabel('Time (sec)','FontName','TimesNewRoman','FontSize',12)
% ylabel('Pressure amplitude (-)','FontName','TimesNewRoman','FontSize',12)
% set(gcf,'Color',[1 1 1])
% title('Input Signal', 'FontName','TimesNewRoman','FontSize',14)
% set(gca,'FontName','TimesNewRoman','FontSize',10)
% grid on
%--------------------------------------------------------------------------

%------------------ Output Signal ----------------------------------------

[y,T] = lsim(sys,u,T);
figure; plot(T,y,'r'); hold on; plot(T,u,'b')
xlabel('Time (sec)','FontName','TimesNewRoman','FontSize',12)
ylabel('Pressure amplitude (torr)','FontName','TimesNewRoman','FontSize',12)
set(gcf,'Color',[1 1 1])
%title('Fig. 4: Output response (y, red) to a synthetic signal (u, blue)',
'FontName','TimesNewRoman','FontSize',14)
legend('Output response','Synthetic input signal');
set(gca,'FontName','TimesNewRoman','FontSize',10)
grid on

clc;
AveStartN = round(0.9*Nmult);
y(AveStartN*SizeOf_t : Nmult*SizeOf_t);
umean = mean(u(Nbw2*SizeOf_t*Div+1:Nmult*SizeOf_t*Div))
ymean = mean(y(Nbw2*SizeOf_t*Div+1:Nmult*SizeOf_t*Div))
b
a
T(Nbw1*SizeOf_t*Div)
T(Nbw2*SizeOf_t*Div)
T(Nmult*SizeOf_t*Div)
% ymean/umean
% max(y_step)
% size(t)
% size(T)
%--------------------------------------------------------------------------

% END OF MAIN

%**************************************************************************
%**************************************************************************
```

```
function MagPhaseX = GetTFF(Fname)
fid1 = fopen(Fname, 'r');
tline = fgetl(fid1);
InputFile_Temp = fscanf(fid1, '%g', [3, Inf]);
MagPhaseX = InputFile_Temp'; %??
fclose(fid1);

function PlotTFtoCheck(f,mag,phase,b,a,w);
w_check = w;
h_check = freqs(b,a,w_check);
mag_check = abs(h_check);
phase_check = angle(h_check).*180/pi;

f_check = w_check/(2*pi);
figure; plot(f,mag,'b');
hold on;
plot(w_check/2/pi, mag_check, 'r');
xlabel('Frequency (Hz)','FontName','TimesNewRoman','FontSize',12)
ylabel('Pr/Ps (-)','FontName','TimesNewRoman','FontSize',12)
set(gcf,'Color',[1 1 1])
set(gca,'FontName','TimesNewRoman','FontSize',10)
title('Fig. 1: Amplitude Ratio - given (blue); Matlab sys (red)',
'FontName','TimesNewRoman','FontSize',14)
grid on

figure; plot(f,phase*180/pi,'b');
hold on;
plot(w_check/2/pi, phase_check, 'r');
xlabel('Frequency (Hz)','FontName','TimesNewRoman','FontSize',12)
ylabel('Phase (deg)','FontName','TimesNewRoman','FontSize',12)
set(gcf,'Color',[1 1 1])
set(gca,'FontName','TimesNewRoman','FontSize',10)
title('Fig. 2: Phase Lag - given (blue); Matlab sys (red)', 'FontName','TimesNewRoman','FontSize',14)
grid on

function w = CorrectW(w);
flag = 1;
[NumPts, junk] = size(w);
for i = 1:NumPts
   while(flag == 1)
      if (w(i) > pi)
         w(i) = w(i) - pi;
      else
         flag = 0;
      end
   end
end



% The use and application of all Matlab functions in the code can be found at:

% http://www.mathworks.com/access/helpdesk/help/helpdesk.html
```

VITA

Vijay Ramakrishnan
Department of Aerospace Engineering
3141 TAMU
College Station, TX 77843-3141
(979) 845-0729
vijayr@tamu.edu

Ph.D. Aerospace Engineering, Texas A&M University, December 2006.
M. S. Aerospace Engineering, Texas A&M University, May 2004.
B. Tech. Aerospace Engineering, Indian Institute of Technology-Madras, India, August 2001.